**Tracking of Photons and detection of thermal Neutrons with a GEM-Detector**

**Spurrekonstruktion von Photonen und Nachweis thermischer Neutronen mit einem GEM-Detektor**


Masterarbeit der Fakultät für Physik
der
Ludwig-Maximilians-Universität München

vorgelegt von

**Bernhard Flierl**

geboren in Bobingen

München, den 28.10.2014

Gutachter: Prof. Dr. Otmar Biebel

# Abstract

In this thesis the construction and the usage of gaseous-electron-multiplier-based detectors (GEM) is described with the aim of tracking photons in the energy range of 5-50 keV and detection of fast and thermal neutrons. The GEM-detector is a gaseous detector based on electron multiplication in thin copper-coated Kapton-foils. Three detectors with an active area of 100·100 $mm^2$ have been built with one-, and two-dimensional strip readout. Simulations with Garfield and Geant4 have been carried out to understand the detector response to a given particle signal. In order to reconstruct the tracks of charged particles in the detector a TPC-like analysis method was used. The inclination angle of these tracks was determined using the time of arrival information of secondary electrons on the respective strip. This method has been tested in the Cosmic Ray Facility in Garching (CRF) with cosmic muons, which were referenced by muon drift tubes with high accuracy. It was possible to reconstruct angles larger than 10° in a single GEM-detector with a resolution of up to 2°.

The intrinsic poor detection efficiency for photons could be increased by utilization of solid converter layers of high-Z material as cathodes. A improvement of 120% was observed in the energy range of 35-50 keV for a cathode, which was coated with a 466 nm gold layer, in comparison to a standard aluminized Kapton-cathode. The simulated and measured angular distribution of photoelectrons of 5.9 and 35 keV were compared and good agreement was found for the case of the higher energy. Simulations predict, that reconstruction in principle can work for energies larger than 20 keV, because of the straight electron tracks for this energies.

Simulations based on the reconstructed angular resolution also predict, that the position of point sources of photons can be reconstructed in space from these measurements. In order to achieve this, the angular dependence of the photoelectrons from the direction of the photon has been exploited.

Thermal neutrons could be detected by a $^{10}B$-based converter cathode, which has a high neutron capture cross-section of 3836 b $atom^{-1}$ and emits a $^4He$ and a $^7Li$ ion with a combined energy of 2.8 MeV in this process. Measurements have been carried out at the "Forschungs-Neutronenquelle Heinz Maier-Leibnitz" with undirected thermal neutrons from a moderated $^{252}Cf$ source and with a thermal neutron beam of small divergence. The best conversion efficiency could be achieved with a 2 µm layer of $^{10}B$ and by tracking of the ions, which are produced in the capture process, the resolution of the conversion point could be improved from (3.45±0.01) mm to (366±1) µm, for measurements with neutrons of 4.7 Å.

# Kurzzusammenfassung

Diese Arbeit beschreibt den Aufbau und die Verwendung von gaseous-electron-multiplier (GEM) basierten Detektoren mit dem Ziel Photonen im Energiebereich von 5-50 keV zu tracken und schnelle und thermische Neutronen nachzuweisen. Der GEM-Detektor ist ein Gasdetektor der auf der Verstärkung von Elektronen in einer Kupferbeschichteten-Kaptonfolie basiert. Es wurden dazu Detektoren mit ein- und zweidimensionaler Streifenauslese gebaut, die eine aktive Fläche von 100·100 $mm^2$ haben. Es wurde Simulationen mit Garfield und Geant4 durchgeführt, um die Detektorsignle besser zu verstehen. Zur Rekonstruktion der Spur geladener Teilchen wurde dazu eine zeifauflösende Auslese verwendet. Dazu wurde eine TPC-artige Methode verwendet um aus der unterschiedlichen Driftzeit von Elektronen die Spur der Teilchen zu rekonstruieren. Um diese Methode zu testen wurden Spuren von kosmischen Myonen in der Cosmic-Ray-Facility (CRF) in Garching referenziert und mit den Ergebnissen aus der Rekonstruktion im GEM-Detektor verglchen. Es wurde gezeigt, dass ab einem Einfallswinkel der Myonen von mehr als 10° die Winkelrekonstruktion mit einer Auflösung von bis zu 2° funktioniert. Um die intrinsische schlechte Effizienz bei der Detektion von Photonen zu erhöhen, wurden unterschiedliche Konversionsschichten getestet. Für Photonen im Energiebereich von 35-50 keV wurde eine Effizienzsteigerung von 120% beobachtet für eine Kathode, die mit einer 466 nm Goldschicht beschichtet wurde, im Vergleich zu einer Standardkathode. Für Photonen wurde die rekonstuierte Winkelverteilung von Photoelektronen mit simulierter Winkelverteilung verglichen und gute Übereinstimmung bei 35 keV Photonen erzielt. Simulation und Messung zeigten ausserdem, dass die Rekonstruktion erst ab einer Photonenergie von 20 keV funktonieren kann. Simulationen die auf den rekonstruierten Winkelverteilungen von 35 keV Photonen basieren zeigen ausserdem, dass die Rekonstruktion einer Punktquelle im Raum möglich ist. Dazu wurde die Winkelabhängigkeit der Photoelektronen zu den einfallenden Photonen ausgenutzt.

Um thermische Neutronen zu detektieren wurde eine Konversionsschicht aus boriertem Material in den Detektor eingebracht, die nach thermischem Neutroneneinfang $^4$He und $^7$Li Ionen mit einer Gesamtenergie von 2.8 MeV aussendet. Die Messungen fanden an einer moderierten $^{252}$Cf-Quelle und in einem gerichteten Neutronenstrahl an der Forschungs-Neutronenquelle Heinz Maier-Leibnitz statt. Die beste Effizienz für den Nachweis thermischer Neutronen wurde dabei mit einer 2 µm Konversionsschicht aus reinem $^{10}$B erreicht. Die Produkte aus der Neutroneneinfangreaktion des Bors konnten einzeln getrackt werden. Im Neutronenstrahl konnte die Ortsauflösung vermessen werden und durch Anwendung der aus der Winkelbestimung der Ionen resultierneden Winkelkorrektur von (3.45±0.01) mm auf (366±1) µm verringert werden für Neutronen.

# Contents

# 1 Introduction

The Large Hadron Collider (LHC) at CERN will get a luminosity upgrade in 2018 from the present $7{\cdot}10^{33}$ $cm^{-2}s^{-1}$ to $2{\cdot}10^{34}$ $cm^{-2}s^{-1}$ (see [1]). The muon chambers in some regions, which are used since the beginning of the experiment, were not designed to work under these high rates which are expected for both signal and background. Therefore they will be exchanged by high rate capable and background tolerating track resolving detectors.

All these requirements can be fulfilled by multiplets of large area micro pattern detectors which will be used as fast triggers but also for muon track reconstruction. The Micromegas gas detectors used for this system are designed to track muons also in one single layer and use this information to improve the spatial resolution in each layer. For tracks of particles with a range, which is orders of magnitudes larger than the active volume of the detector, the position of the track can be well approximated with the center of the track in the active volume. For non ionizing particles, which are absorbed in the process of detection and create only tracks which are comparable to the drift volume a systematic error in the spatial detection has always been done, since the point of creation is not the center of the track.

The reconstruction of the source of a track might vastly improve the spatial resolution. The idea is to use this method to reconstruct the origin of a charged particle, which was created by photons in the energy range of medical imaging (20-50 keV) or fast and thermal neutrons. Three questions arise from this issue:

Is it possible to detect the particles with sufficient efficiency?
Can the tracks of the secondary particles be reconstructed?
Is it possible to calculate the origin of the particle?

For this task a gaseous electron multiplier (GEM), which is also a high rate capable and background tolerating gaseous detector with high intrinsic resolution has been chosen. GEMs have already been used for detection of neutrons and photons, but the reconstruction of tracks has not yet been carefully investigated.

# 2 The GEM-Detector

Gaseous detectors have a long tradition in particle physics. In 1899 J.J. Thompson thoroughly investigated an effect, which was already discovered by W.C. Röntgen in 1895, the ability of X-rays to ionize air, which could be detected with an electroscope and an electric field to separate the charges [2]. The ionization chamber was invented. The charge created in a gaseous volume by ionizing radiation, like gamma and x-rays, or beta particles, is collected by two electrodes. Electrons and ions are separated by an electric field and if the electrons reach the anode they will lead to a small but measurable current. This signal can be increased by applying higher voltages to the electrodes. The electrons will be accelerated accordingly and can themselves ionize gas atoms. This leads to a higher amount of electrons, which can be detected at the anode. In a wide voltage range this multiplication process is proportional to the number of primary electrons and the detector is called a proportional counter. If the voltage is increased even more the signal at the anode is no longer proportional to the initial number of electrons. In this so called Geiger region every ionization in a detector of this type creates an electron avalanche, which will not stop until the electric field breaks down due to the current produced by these electrons.

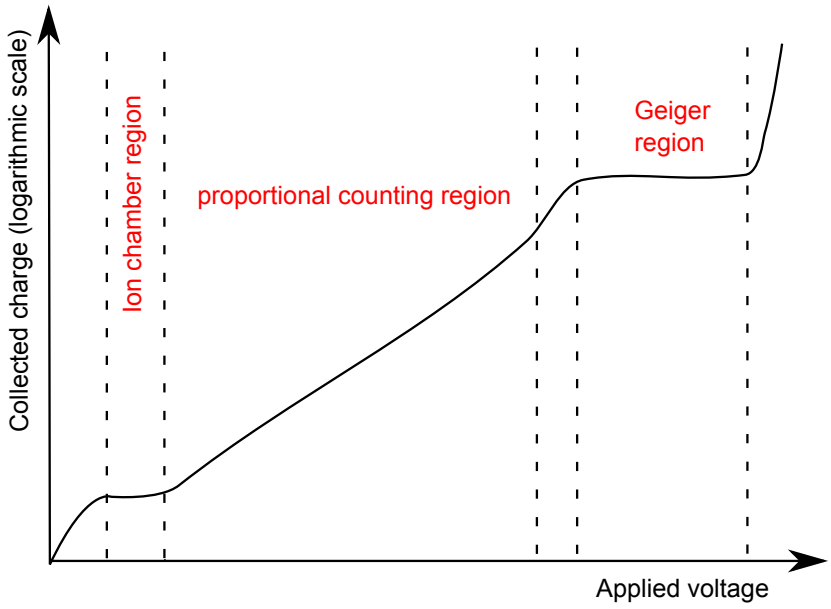


Figure 2.1: Scheme of charge collection against applied voltage for different gas detectors

Further increase of the voltage would lead to unwanted continuous discharges between the electrodes independently of the ionizing radiation .

## 2.1 Ionization processes in gaseous detectors

Primary ionization in a gaseous detector can happen in different ways, depending on the charge and energy of the incoming particle. In the case of charged particles the Bethe-formula applies. This formula describes the mean energy loss of a charged particle due to interaction with the electron shells of the matter it is traversing (taken from [3]).

$$-\left\langle \frac{dE}{dx} \right\rangle = Kz^2 \frac{Z}{A} \frac{1}{\beta^2} \left[ \frac{1}{2} \ln \frac{2m_e\gamma^2\beta^2c^2T_{max}}{I^2} - \beta^2 - \frac{\delta(\beta\gamma)}{2} \right] \tag{2.1}$$

Here $K$=$4\pi N_A r_e^2 m_e c^2$, with $N_a$ the Avogadro constant, $m_e$ and $r_e$ are the mass and the classical radius of the electron of $2.818 \cdot 10^{-15} m$. $Z$ and $A$ are the atomic number and mass of the medium, $\beta = \frac{v}{c}$ is the relativistic velocity of the incoming particle , $z$ is the charge of this particle, $\delta$ the Fermi density correction (see [4]), $T_{max}$ the maximum energy transfer and $I$ the mean ionization potential of the material.

The energy loss in the medium can lead to excitation, emission of photons and most importantly to ionization. Energy deposition in the detector leads to an amount of electron ion pairs, which is depending on the gas mixture. The mean number of pairs created depends on the mean energy for creation of an ion-electron pair, which is different from the ionization potential for a gas atom or molecule.

Table 2.1: Mean energy for ion-electron pair creation for different gases (taken from [5])

| Gas | Mean energy for ion-electron creation [eV] | Ionization potential [eV] |
|---|---|---|
| $H_2$ | 37 | 15.4 |
| He | 41 | 24.6 |
| Ar | 26 | 15.8 |
| Kr | 24 | 14 |
| $CO_2$ | 33 | 13.7 |
| $CH_4$ | 28 | 13.1 |

Photons can also ionize matter, which is typically done by transfer of energy to an electron of the atomic shell. There are mainly two processes, where this can happen: The so called Photoelectric effect, where a photon hits an electron of the medium and transfers its entire energy to this electron. The other process is the Compton scattering. Here the photon loses only a fraction of its energy and momentum to an electron. Both electron and photon will then have a share of the initial energy and can individually ionize further atoms. The third way, how a photon can lose energy in matter, is creation of electron-positron pairs. If the photon has more energy than 1.022 MeV, which is twice the rest mass of an electron, this can happen in the electric field of an atom. Which process is most dominant is depending on the energy of the photon. For low energies up to about 100 keV Photoelectric effect is the most dominant process. For higher energies Compton effect becomes more important and for energies above

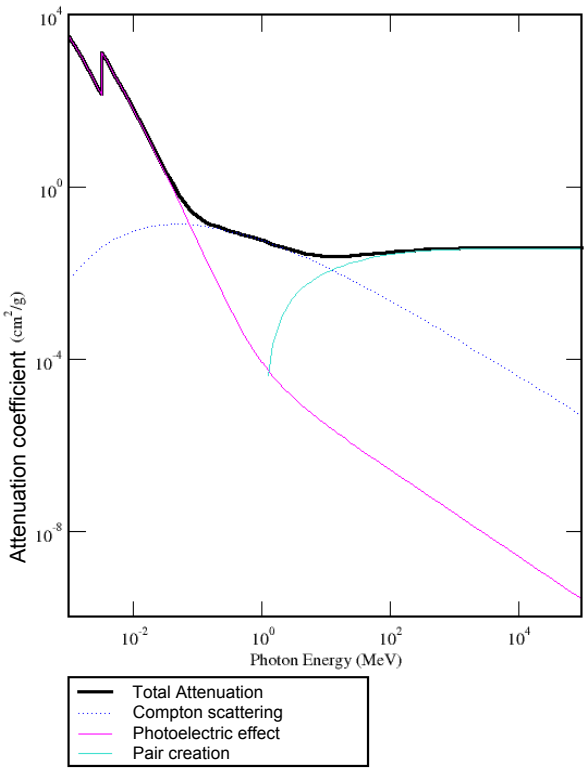


Figure 2.2: Photon attenuation coefficient in dependence of the photon energy for argon (taken from [6])

around 10 MeV pair creation is the most probable process. The exact boundaries are material dependent. For the example of argon the attenuation of photons due to these three processes is shown in figure 2.2.

## 2.2 Gas multiplication process

If 100 primary electrons in the detector are created[1] and all of them reach the anode within 10 ns the current produced by this electron cloud would just be in the order of pA, which is comparably difficult to measure. To increase this current, or the number of detectable electrons, a stage of multiplication can be embedded in the detector. In a gaseous detector this is achieved with a high electric field, that accelerates the primary electrons causing them to lose some of their kinetic energy by ionizing another gas molecule. This process is called Townsend-multiplication. The multiplication in a so called Townsend-avalanche along a path from $r_1$ to $r_2$ can be described by (see [7]):

$$G = e^{\left[\int_{r_1}^{r_2} \alpha(x)dx\right]} \tag{2.2}$$

1 This is roughly the equivalent of 3 keV of deposited energy for most gases

Where $\alpha$ is the Townsend-parameter which is a function of the electric field and the gas. A possible parametrization model is given by Rose and Korff [8], which can be used to describe the gain also in a GEM-detector depending on the electric field and the particle density n:

$$\frac{\alpha}{n} = A_0 e^{-\left(\frac{B_0 n}{E}\right)} \tag{2.3}$$

Here $A_0$ and $B_0$ are gas constants.

Another contribution to the ionization of gas atoms is the so called Penning effect. This is in fact more a group of processes, that can increase the gas gain in the detector. In this process an atom is excited into a metastable state, which can be deexcited by a collision with another atom and ionize it. This effect has to be taken into account if the gain is simulated especially in Ar-$CO_2$ mixtures, because of the coincidental concurrence of excitation and ionization energies for both gases [9].

Since the electrons in this process do suffer a great amount of collisions. They therefore cannot strictly follow the electric field lines and will also diffuse perpendicular to them. Since this process is arbitrary and there is a great number of collisions, electrons starting from an initial point $x_0$ will have a lateral Gaussian distribution to the electric field at the readout plane with mean value $x_0$ and standard deviation of:

$$\sigma(r) = \sqrt{6Dt} \tag{2.4}$$

Where D is the diffusion coefficient and t is the drift time (see [5]).

## 2.3 The Gaseous Electron Multiplier (GEM)

The GEM-detector concept was introduced by F. Sauli in 1997 [10]. The GEM-detector is a gaseous detector, which works as a proportional counter, meaning that the charge that reaches the readout anode of the detector is proportional to the energy deposition in the detector.

In a gaseous electron multiplier (GEM) the multiplication of the primary electrons is realized by 50 µm Kapton foils which are cladded at both surfaces with a thin copper layer of 5 µm. By means of photo-lithographic methods conical holes of 60 µm inner and 70 µm outer diameter are etched in these foils with a pitch of 140 µm (see figure 2.3(a) and 2.3(b)). This leads to a triangle shaped periodic hole structure in the foils. Application of a moderate voltage difference on both side of the foils leads to very high electric fields in the holes. For example 350 V potential difference will lead to an electric field of 70 $\frac{\text{kV}}{\text{cm}}$. This high field will lead to a multiplication of the incoming electrons by a factor of 15-30 (see also [11] and chapter 4). The electrons are guided through the holes along the electric field lines, which leads to a higher transparency for the electrons than the optical transparency of 46 % (see [12]). In order to get even higher amplification one can stack multiple layers of these foils and potentiate the outcome, but also minimize the probability of uncontrolled discharges [13], which can potentially destroy the foils.

## 2.4 Detector setup

The principle setup of all detectors used in this thesis is shown in figure 2.4. An aluminum housing contains three GEM-foils and a cathode laying all on negative high voltage. The active volume is defined by the size of the GEM-foils of 10·10 $\text{cm}^2$. The foils used are standard GEM-foils produced by CERN detector laboratory [15]. The distance between the anode and the first GEM-foil is 2 mm. The field applied between anode and GEM-foil is called induction field, because of the signal that is induced on the readout. The distance between two GEM-foils is always 2 mm, with the upper field being called $\text{E}_{Trans1}$ and the lower one called $\text{E}_{Trans2}$. The distance between the uppermost GEM-foil and the cathode can be varied for different applications, but usually a distance between 6 to 10 mm is a good value to work with muons or photons. The field in this region is called drift field. The readout anode lies on ground potential. For the detection of photons the housing has a window, which is sealed with a 10 µm Kapton-foil.

In principle it would be possible to run the detector with a single high voltage source over a resistor chain (see [16]). But for reasons of convenience and usability, here every voltage was applied separately in order to achieve better tuning possibilities, which otherwise would be limited by the resistors.

The detector is designed to work at slight overpressure of 20-30 mbar with constant gas flux to minimize gas pollution and ageing effects. A scheme of the whole gas system is shown in figure 2.5. The gas system used is capable of mixing up to four different gases and can control the gas pressure. Gas flux and pressure are tunable

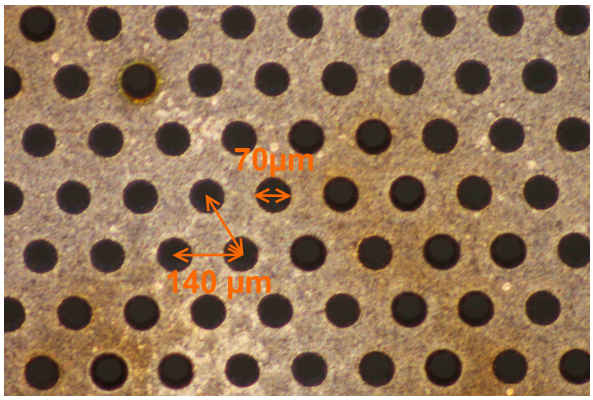


(a) Microscopic image of a GEM structure

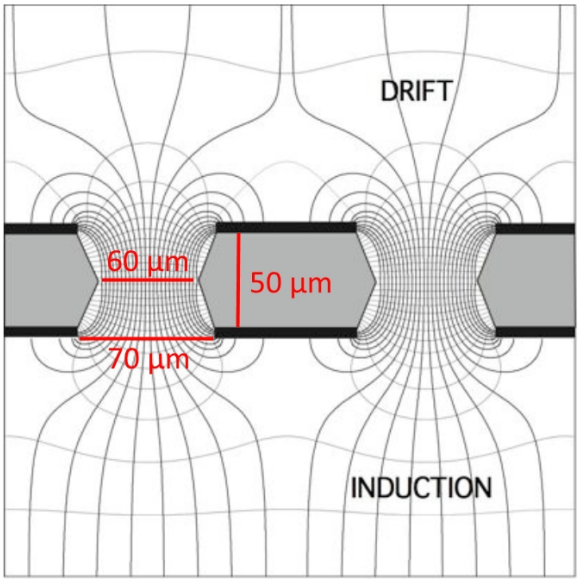


(b) Hole structure and electric fields inside a GEM-foil (taken from [14])

Figure 2.3: Geometry of GEM-foils

and can be held constant via Mass-Flow-Controllers and a Baratron controlled valve system. The measured pressure signal from the Baratron is conditioned and an outlet valve is controlled to adjust the pressure. The temperature is not actively controlled, but since the particle density inside the detector has influence on the pulse height of the signals, pressure and temperature are also logged (see equation 2.3).

If not mentioned especially all measurements and simulations in this thesis have been carried out with an Ar-$CO_2$ mixture of 93-7 Vol.% with a particle density of $(3.35 \pm 0.01)\,\mathrm{mbar\,K^{-1}}$. Argon is the main gas for the gas amplification and the creation of electrons. The $CO_2$ admixture works as a so called quencher. It catches photons, which are also produced in the amplification and hinders them to ionize again somewhere else in the detector.

The readout of the detector is based on copper strips, which collect the electrons. There were two types of strip designs used: Two identical detectors with one dimensional readout of 384 parallel strips with a pitch of 250 µm have been built (described

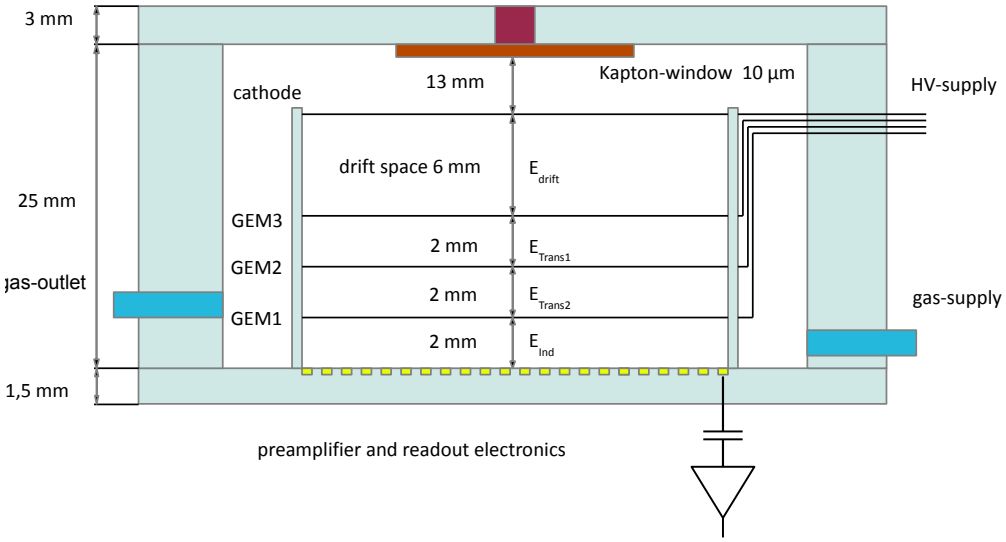


Figure 2.4: Illustration of the actual detector setup.

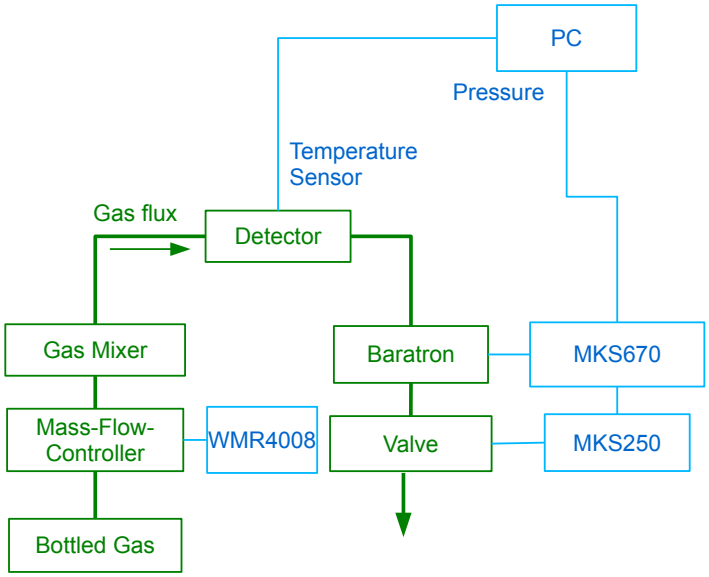


Figure 2.5: Scheme of the gas system: The flow through the detector is adjusted by Mass-Flow controllers , which are operated by a WMR4008 control unit. The gas flows through the detector and the pressure is measured by a Baratron which feeds a MKS670 Signal conditioner and a MKS250 pressure controller, which guides a magnetic valve. Pressure and temperature are logged

in [12]). The other type was based on a standard two dimensional readout board for GEMs from CERN. It consists of crossed strips with a pitch of 400 µm and 250 strips per direction (see also section 3.4).

The readout system is based on APV25 frontend boards (see [17]) which are programmable charge sensitive preamplifiers with ring memory. Although these chips were initially designed for silicon strip detectors they are now used for gaseous detectors like Micromegas (see [18]) and GEM, for example in the Compass experiment (see [19]). The APV25-chip has the capability of time resolved sampling of the signal, which allows to sample up to a depth of 30 steps with 40 MHz rate for 128 channels. Here the APV25 chips are mounted on Hybrid-cards developed by the RD51

collaboration, which also contain eight two-channel 12-bit analog-digital-converters (ADCs) and protective circuits to compensate for discharges to the readout. The signal from the Hybrid-cards are read out by a so called Front-End Concentrator card (FEC) which is basically a Xilinx Virtex-5 field-programmable gate array (FPGA). Every FEC-card is capable of controlling 8 pairs of Hybrid-cards[2]. The FEC-card is connected to a computer by a Gigabit ethernet interface . This system allows to read out every strip separately and time resolved.

Since the FEC-card needs an external trigger it is helpful to collect the signal also at the lowest GEM-foil. This is possible, because a signal is also induced by the drift of the electrons towards the anode on the lower surface of this GEM-foil (see figure 2.6). The signal is tapped by a 1 pF coupling capacitor and a charge sensitive preamplifier. It is then shaped by a Timing Filter Amplifier (TFA), with a typical shaping time of 60 ns. The trigger is then formed by a discriminator if the shaped signal exceeds a threshold, which starts the readout via the FEC-card. The whole readout is presented in figure 2.7.

Since the capacity of the GEM-foil is much larger than the capacity of the single readout strips the signal is much lower, as it can be seen in figure 2.6(b).

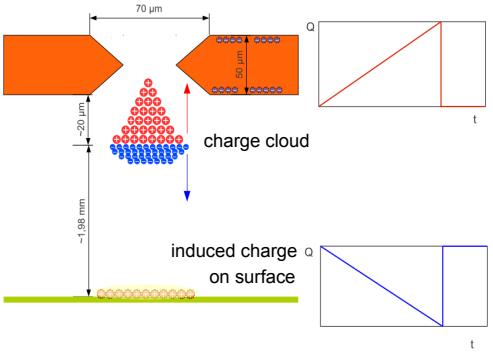


(a) Scheme of the signal formation on anode and GEM-foil.

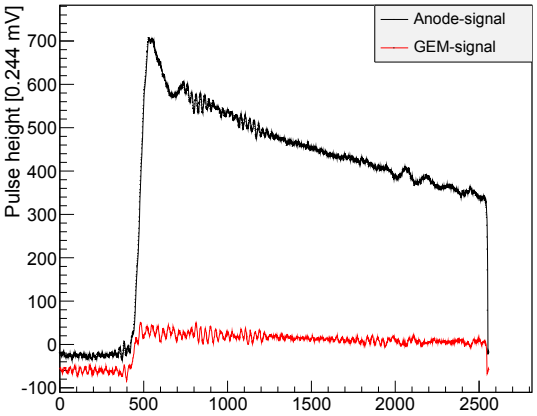


(b) Comparison of signal at anode and GEM-foil. Measurement with FlashADC and all strips shortened. The polarity of the GEM-signal is inverted for better comparision

Figure 2.6: Signal forming and signal shape at anode and lowest GEM-foil

2 For larger systems multiple FEC-cards can be combined in a Scalable Readout System (SRS)

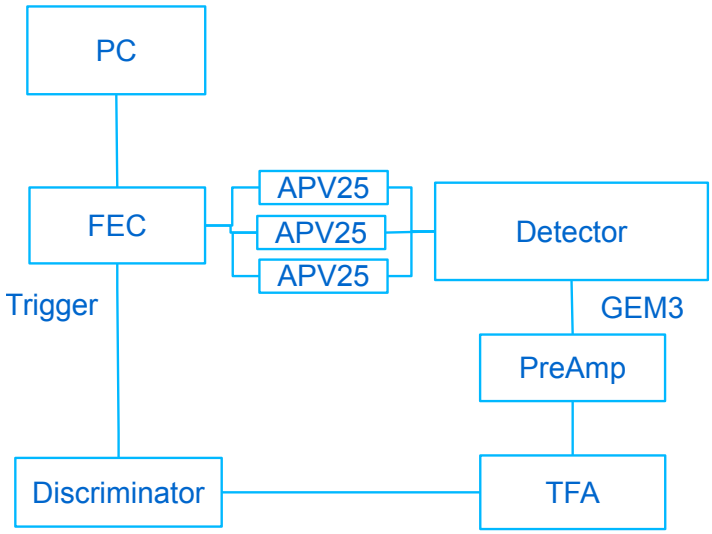


Figure 2.7: Scheme of the standard APV25 based-readout electronics. One APV per 128 strips is connected to the strips of the detector. The APV25-Hybrid card are connected to the FEC-card by HDMI-cables. A signal is tapped from the third GEM-foil , which triggers the redout electronics. The FEC-card communicates with a PC over an ethernet interface

## 2.5 µTPC-electron drift reconstruction

Utilization of the time resolving readout in principle allows to fully reconstruct the three-dimensional track of a particle along with the specific energy loss dE/dx in the gaseous volume. The drift velocity of the electrons in the detector is comparably small to the velocity of the detected particles. Therefore electrons from a track which are produced closer to the anode will also arrive at an earlier time. This method is widely used in so called time projection chambers (TPC). The Z-component of the track can be calculated from the arrival time of the electrons, if the drift velocity in the gas is known. The huge advantage of this method is, that a single readout plane is sufficient to track a particle. If long tracks have to be detected TPC can become very large, the ALICE-TPC at LHC for example has an overall length of 510 cm and is divided into two drift regions (see figure 2.9 and also [20]).

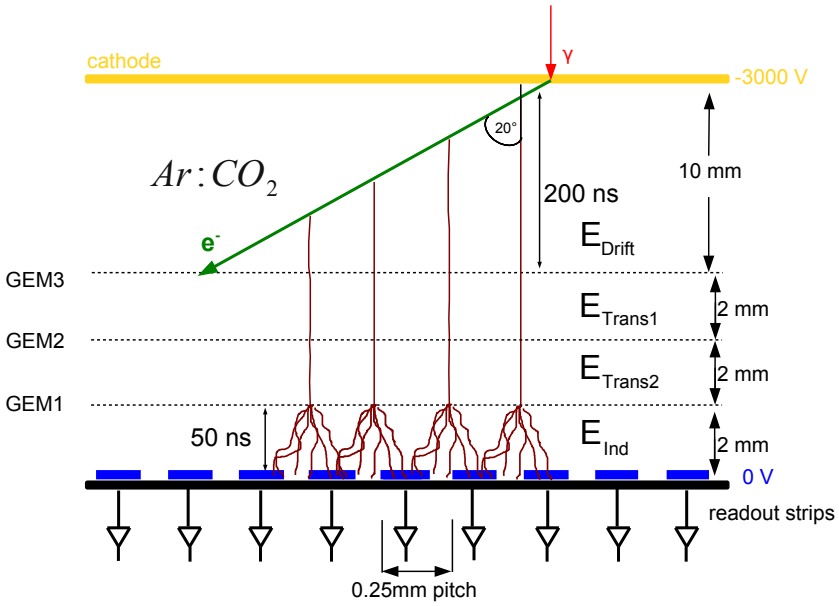


Figure 2.8: Concept of µTPC in a GEM-detector.

If the time resolution of the readout is high enough this method can also be applied for shorter tracks and thinner drift spaces, here for example $\mathcal{O}$(cm). In order to reconstruct the inclination angle of the track of an incident particle it is wishful to know position and arrival time of the electrons at the readout plane as good as possible. If gas distribution, pressure and the electric field are constant in the region of interest, the drift velocity will also be constant. This is the case in the GEM-detector, where the field is homogenous in every gap, with the exception of the direct vicinity of about 300 µm to the GEM-foils (see [22]), which is neglectable comparing to the other dimension of $\mathcal{O}$(cm). The electron drift velocity can be looked up, or being calculated for example by using tracks of particles with known inclination.

The inclination angle can be calculated as follows:

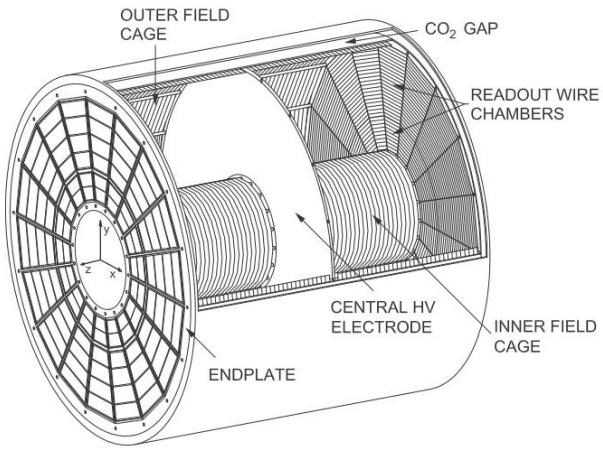


Figure 2.9: 3D-view of the ALICE-TPC field cage. The overall length is 510 cm and the diameter is 556 cm, (taken from [20]). The readout of the detector at the moment is done with wire chambers, but GEM-based readout for a future upgrade has also been discussed and tested (see [21])

$$\theta = \arctan \frac{\Delta x}{\Delta z}$$
$$\text{where}$$
$$\Delta z = v_{Drift} \cdot \Delta t \tag{2.5}$$

$v_{Drift}$ is the drift velocity of the electrons and $\Delta x$ and $\Delta t$ are the width and duration of the track.

## 2.6 Radioactive sources

As sources for photons nuclides of americium, barium, cesium and iron have been used. The most important lines in the energy spectra of the respective sources are shown in table 2.2. Other types of radiation, which in principle are also produced by these sources were shielded by the wrapping of the respective sources, for example 1 MeV electrons from the cesium decay.

Table 2.2: Most important photon energies of used sources (taken from [23] and [24])

| Nuclide | Energy [keV] (relative intensity per decay ) |
|---|---|
| $^{241}$Am | 60 (67%),26 (2.4%) |
| $^{133}$Ba | 356 (62%),81 (34%),35 (22%) |
| $^{137}$Cs | 661 (85%) |
| $^{55}$Fe | 5.89(60%),5.88(16%), 6.5(8.2%) |

Since the attenuation coefficients for photons strongly depend on the photon energy for $^{133}$Ba the energy of interest is the 35 keV line. The total attenuation length for

35 keV photons for example is in gold 17 $cm^2/g$ whereas the attenuation length for 356 keV photons is only 0.25 $cm^2/g$ (see [6]). Therefore the 35 keV line is effectively the most detected energy. The $^{55}$Fe-source is sometimes referred to their double line at 5.9 keV, which cannot be resolved by the GEM-detector (see also chapter 4).

# 3 Signal analysis

The recording of the data is done with the mmdaq-software (see [25]), which was developed by the RD51-collaboration for the use with Micromegas-detectors. The signal is sampled in 25 ns steps for every strip at 27 time bins per event. If the readout is triggered the signal on every strip is written into a root-tree, if the pulse height exceeds a chosen threshold on this strip. A raw signal typically looks like the one shown in figure 3.1(a). This software allows for data acquisition with a rate up to 300 Hz and some online event display to check for inconsistencies.

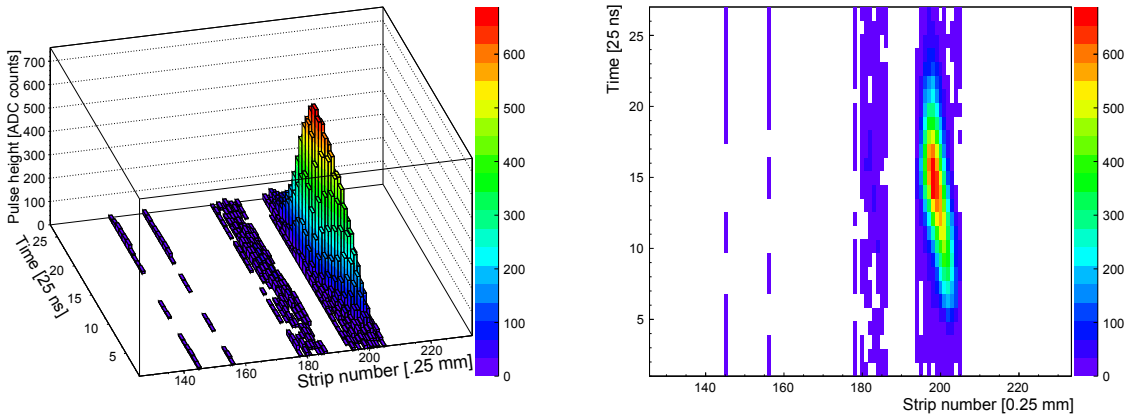


(a) Raw charge signal created by neutron capture process in a Boron cathode (see chapter 9)

(b) Projection of the same signal on the x-t plane

Figure 3.1: Raw data of charge distribution in readout plane for a track of a $^{7}$Li or $^{4}$He ion after neutron capture in $^{10}$B

The data analysis is done off-line and consists of multiple steps. For every recorded event the charge collection at every strip is fitted with two functions. The essential parameters for further analysis are the maximum height (i.e charge collected) for every strip, the starting time of the signal and the overall duration of the signal.

For short signals, i.e a signal rise time of less than 4 time bins an inverse Fermi function yields a good parametrization.

$$f_1(t) = \frac{p_0}{e^{-\frac{t-p_1}{p_2}} + 1} + p_3 \tag{3.1}$$

The maximum pulse height $p_0$ is adapted to the value of the highest bin and the range of the fit is confined to two bins after the highest bin in order to suppress the

decrease of the signal, which contains no further information. The starting time of the signal is extrapolated using $t_1$ and $t_2$, being the timing at 1 and 99% of the maximum pulse height (see figure 3.2):

$$t_0 = t_1 - \frac{0.01\,(t_2 - t_1)}{0.98} \tag{3.2}$$

$$t_1 = p_1 - \ln\frac{1}{0.01}p_2 \tag{3.3}$$

$$t_2 = p_1 - \ln\frac{1}{0.09}p_2 \tag{3.4}$$

The duration of the signal is calculated by the difference between the 99% time and the extrapolated start value:

$$\Delta t = t_2 - t_0 \tag{3.5}$$

For signals that exceed four time bins this method is not optimal and leads to some bias to the timing calculations. Therefore an Arctan-function is also fitted to the single strip signal, which is better suited for longer rise times.

$$f_2(t) = p_0 \arctan(p_1(x - p_2)) + p_3 \tag{3.6}$$

Quite similar to the first function the starting time and the duration are calculated by extrapolation of the 1 and 99% values.

$$t_0 = t_1 - \frac{0.01\,(t_2 - t_1)}{0.98} \tag{3.7}$$

$$t_1 = \frac{\tan(0.01\pi)}{p_1} + p_2 \tag{3.8}$$

$$t_2 = \frac{\tan(0.99\pi)}{p_1} + p_2 \tag{3.9}$$

$$\Delta t = t_2 - t_0 \tag{3.10}$$

## 3.1 Cluster building

All the information of a track in the detector is contained in clusters of neighbouring strips which are hit. In the process of the cluster building first all strips are marked as hit or not hit, depending on the maximum charge of the strip evaluated before. Strips that do not exceed a threshold of 45 ADC counts are considered to be not hit and neglected in further analysis, which is an empirical cut value for noise on single strips. The track of a charged particle will hardly lead to only a single strip being hit (see chapter 4). Therefore a cluster has to contain at least two hit strips. In order to account for badly connected strips and non uniform ionization along the track a gap between two hit strips of one strip is allowed.

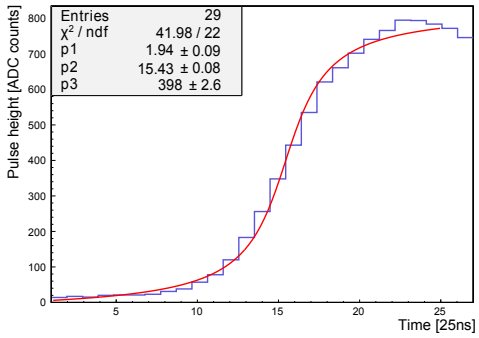


(a) Fit of an Arctan-function to the signal on a single strip

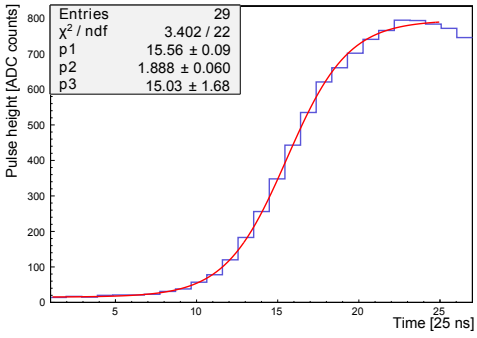


(b) Fit of a Fermi-function to the signal on a single strip

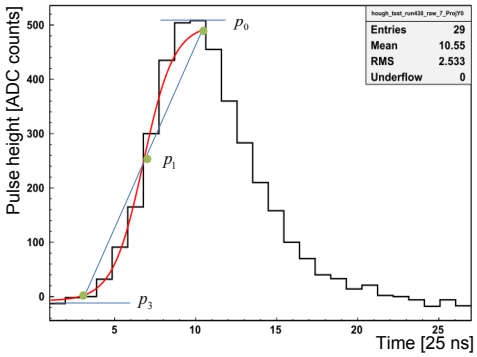


(c) Extrapolation of the start time for a single strip signal based on a fit with a Fermi-function

Figure 3.2: Survey of single strip signals with fit to charge distribution over time. The height ($p_0$) was not fitted, but fixed to the maximum charge for every strip.

How many clusters in an event have to be considered is depending on the expected track length in the detector and the ionization density of the track. For the purpose of photon detection it is sufficient to consider only the leading cluster i.e the cluster that contains most of the charge. This can be seen in figure 3.3 at the example of irradiation of the detector with a $^{55}$Fe-source. Here almost every event contains only a single cluster, because the tracks are very short and photoelectrons ionize quite dense. Therefore the cluster with less charge is neglected further on.

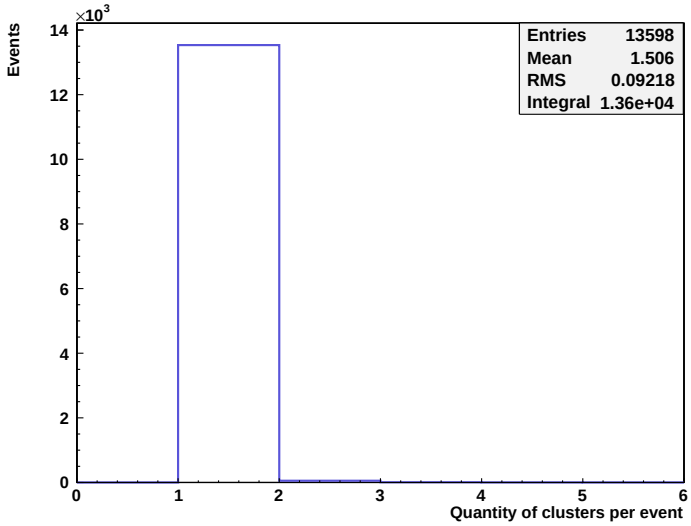


Figure 3.3: Amount of reconstructed charge clusters per event for irradiation with a $^{55}$Fe source

If the rate of incident particles is much higher, or a track of a single particle can lead to more than one cluster one has to be a bit more careful. Long tracks for example can split into two or more clusters, due to not perfectly homogenous ionization along the track. This can be seen in figure 3.4 at the example of a muon track. In the left case the clusters lay on a straight line and the rate of incident cosmic muons is very low, therefore they belong with very high probability to the same track. In this case it would be best to combine all clusters to get the most information for this event. In the left case this distinction is more complicated, since the clusters cannot be arranged on a straight line. This might be due to a delta electron, which was produced by the muon and can leave its own track.

Whether multiple clusters form a single track is determined by a Radon-transformation (see appendix A). This transformation can find straight lines in a hit distribution and is therefore suitable to find tracks. If only one track is found the clusters are combined, if more than one track is reconstructed the event is neglected for further analysis.

## 3.2 Cluster analysis

After the final cluster is built, the properties of this cluster are evaluated.

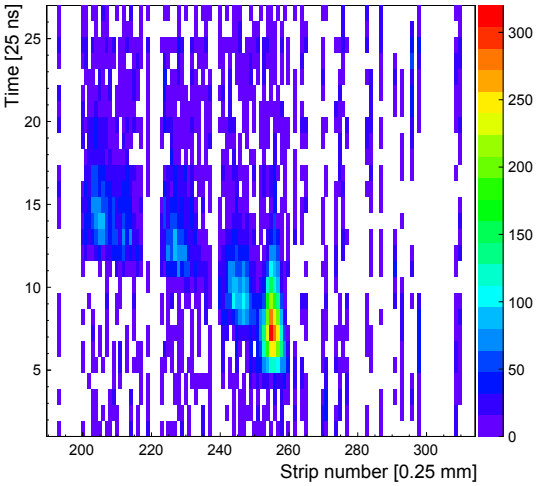


(a) Multiple clusters of presumably only one track in detector due to a cosmic muon. All clusters fit to a single line.

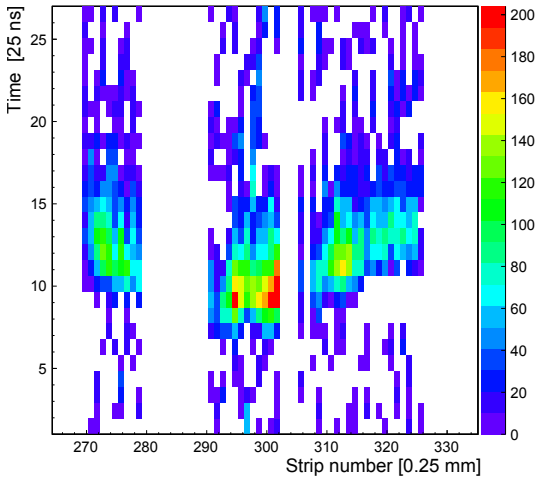


(b) Event in detector with more than one track in multiple clusters with no common direction. Possibly due to a delta electron.

Figure 3.4: Hit pattern in readout plane for tracks of muons

The charge of every cluster is assumed to be the sum of the maxima of charge for the strips in the cluster. The geometric mean of the track is calculated by the mean value over the hit strips. The center of charge $x_c$ for n strips in the cluster is then calculated by the position of the strips $x_i$ weighted with the charge of the respective strip $c_i$.

$$x_c = \left( \sum_0^n c_i \right)^{-1} \sum_0^n x_i \cdot c_i \tag{3.11}$$

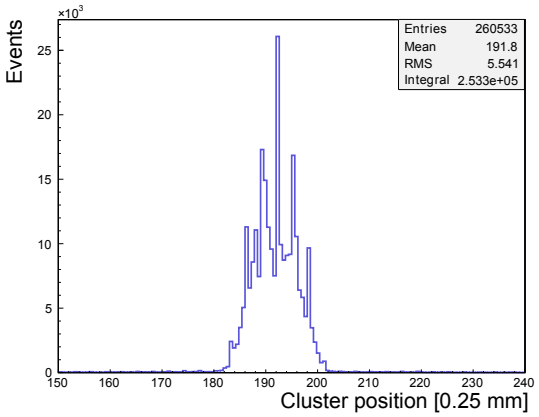


(a) Position of cluster evaluated with geometric mean value of cluster for irradiaton with a $^{55}$Fe source

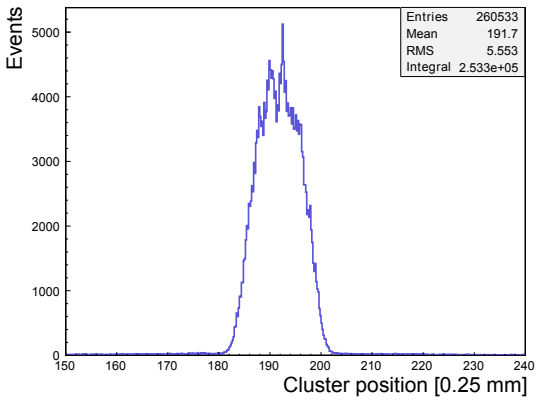


(b) Position of charge averaged mean value of cluster for irradiaton with a $^{55}$Fe source

Figure 3.5: Comparison between geometric mean of position and charge averaged position

The width of the cluster is determined by the number of hit strips. The overall time difference between the fastest and slowest strip in a cluster is calculated and every cluster is marked with a time stamp.

As a last step the inclination angle of every track is reconstructed. Using the strip number and the extrapolated starting time from either the Arctan or the Fermi-Fit to every strip the inclination is calculated from a fit of a straight line to the track as it can be seen in figure 3.6. For the fit only strips are considered that have at least a charge of 20% of the maximum charge in the cluster, which was empirically found to improve the accuracy of the fit. The angle is then computed by the slope m of the line and the drift velocity $v_D$ of the electrons in the gas as:

$$\theta = -\arctan\left(\frac{0.25\text{mm}}{m \cdot v_D \cdot 25\text{ns}}\right) \tag{3.12}$$

This leads to a somehow unconventional definition of the inclination angle, but the algebraic sign of the angle directly shows the direction of the particle. Another reason for the convention of the inclination angle is the fact, that with an one-dimensional readout the actual inclination angle $\theta_w$ cannot be reconstructed, but only its projection onto the precision direction (see figure 3.7). Both angles are correlated in the following way:

$$\tan(\theta_w) = \tan(\theta)\frac{1}{\cos\phi} \tag{3.13}$$

Where $\phi$ is the azimuthal angle, that cannot be reconstructed with just one coordinate in space.

Figure 3.8 shows the reconstructed angle of the two fitting methods. Here the angular distribution of charged tracks due to the irradiation of a $^{10}$B-cathode with thermal neutrons is shown (see chapter 9).

If not otherwise mentioned the reconstructed angles, which are used in this thesis, always represent the projected angles.

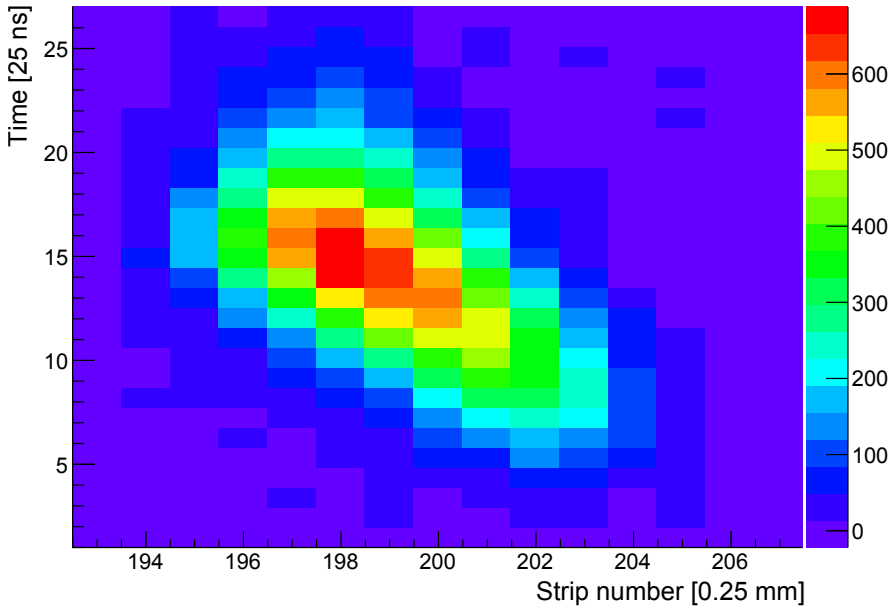


(a) Raw charge cluster

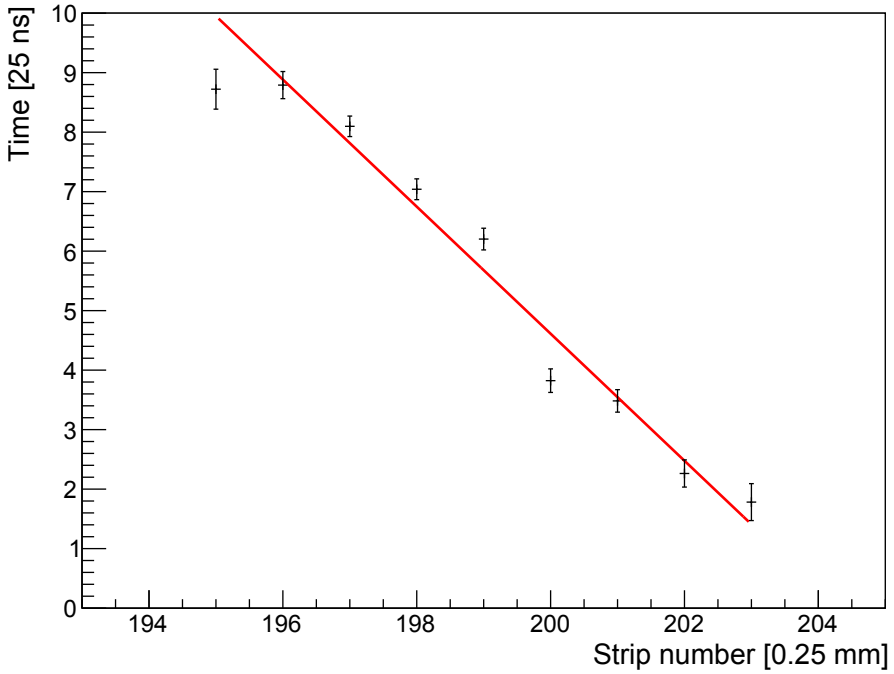


(b) Extrapolated starting time and reconstructred track

Figure 3.6: Position and timing of a track on the readout plane with one dimensional readout

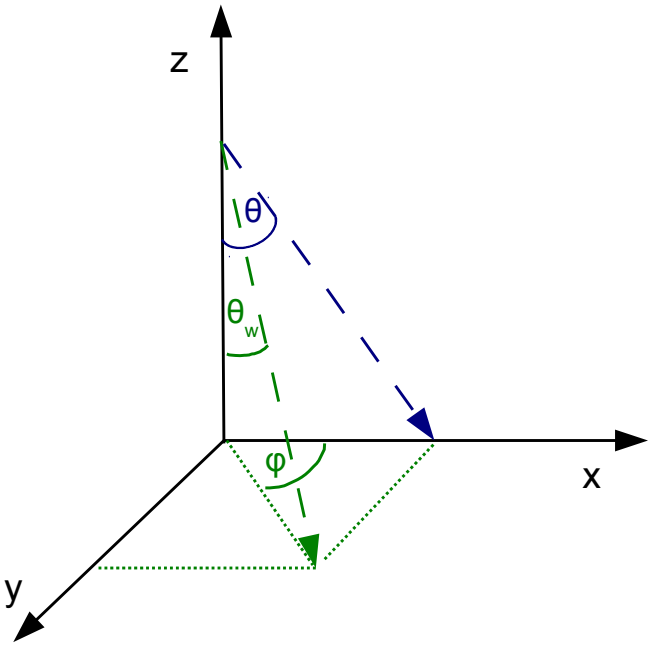


Figure 3.7: Scheme of the reconstructed inclination and the real inclination for a one dimensional readout

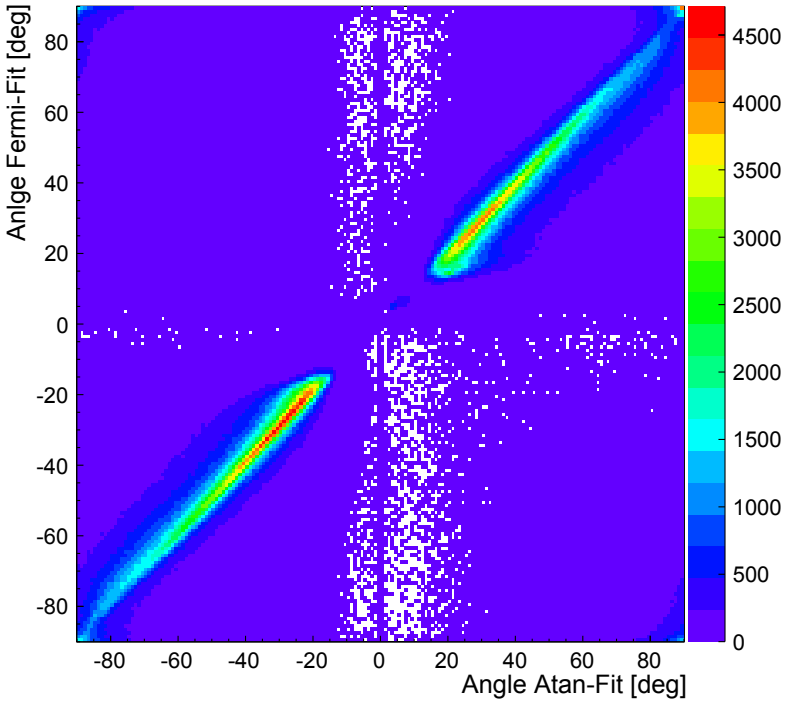


Figure 3.8: Reconstructed angle with two different methods of fitting the properties of every strip for products of the $^{10}$B+n reaction (see chapter 9)

## 3.3 Charge correction

Every two strips of length l, width w and distance d on a readout plane form a capacitor with a capacity of (taken from [26]):

$$C = \epsilon_R \cdot l \frac{\int \sqrt{1 - \left(\frac{d}{2w+d}\right)^2} d\left(\frac{d}{2w+d}\right)}{\int \sqrt{\left(\frac{d}{2w+d}\right)} d\left(\frac{d}{2w+d}\right)} \tag{3.14}$$

So the readout strips do couple capacitively with their respective neighbours directly and over the readout board. This leads to an induced signal on the neighbouring strips, if one strip collects charge (see also [18]). This cross-talk adds up to the signal for every strip and can impair the quality of the angular reconstruction, because this coupling is instantaneous.

In order to correct for this cross-talk the strips in a cluster are ordered by their respective starting time. Beginning with the earliest and going gradually to the last one the raw data of the direct neighbouring strips is time bin wise corrected. This correction works as follows: A fraction of the charge of the bin considered is subtracted from the charge of the right and left neighbours. This is done up to the bin with maximum charge. For all later bins the value of the maximum bin weighted with the charge of the current bin is subtracted. The correction factor, i.e the amount of charge that a neighbour strip sees due to a signal on the first strip, was determined by iteration and minimizing the error of the reconstructed angle (see chapter 7).

## 3.4 Detector with 2D-strip-readout

Most of the measurements in this thesis have been carried out with a one-dimensional strip readout. There was also a detector built with a crossed-strip readout based on a readout board from CERN[3]. This board has 250 strips for both X and Y direction which are placed atop of each other. The strips are placed on the two surfaces of an etched Kapton-foil, which is laminated onto the board. The etching of the foil allows both layers to collect electrons directly. The pitch is in both cases 400 µm. The upper strips are 80 µm wide and the lower strips are 250 µm wide, in order to compensate for the shadowing through the upper strips. If both layers would have the same strip width, the lower plane would see much less charge. Due to this different width the charge collection in both planes is very much the same and well correlated, as can be seen in figure 3.11. The number of strips per cluster is also the same, meaning that the noise level in both directions is also the same and as low as at a single strip readout. With this readout is possible to reconstruct the true inclination of a track and therefore the true track length. This is not possible with a one dimensional readout, as can be seen in equation 3.15, where the mean value of a

3 See [27]

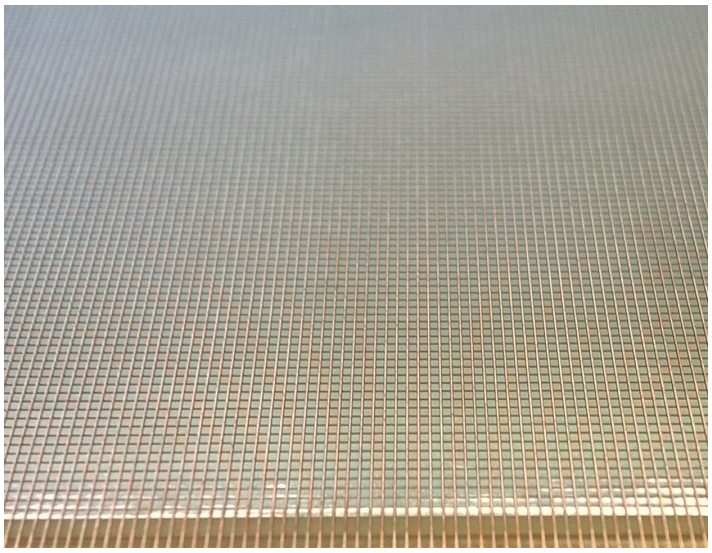

Figure 3.9: Close-up of crossed strip readout board

projected range in the x-direction $N_x$ is calculated from the real track length $N_0$ (see also figure 3.10(a)).

$$\overline{N}_x = N_0 \sqrt{\int_0^{\frac{\pi}{2}} \int_0^{\frac{\pi}{2}} \left(\sin^2(\theta_w)\cos(\phi)\right)^2 d\theta_w d\phi} = \frac{\sqrt{3}\pi}{8} N_0 \simeq 0.68 N_0 \tag{3.15}$$

Whereas the projected length in the XY-plane $N_{XY}$ can be calculated as:

$$\overline{N}_{xy} = N_0 \sqrt{\int_0^{\frac{\pi}{2}} \int_0^{\frac{\pi}{2}} \left(\sin^2(\theta_w)\right)^2 d\theta_w d\phi} = \frac{\pi}{4} N_0 \simeq 0.79 N_0 \tag{3.16}$$

The mean projected value can be calculated from the measured track lengths in both directions:

$$N_{xy} = \sqrt{N_x^2 + N_y^2} \tag{3.17}$$

A comparison between measured values can be seen in figure 3.10(b). The most probable value for the projection in the XY-plane is 11 strips whereas the mean value in X-direction is 9 strips, which matches the expected value. Therefore the calculation of the real track length is possible if the angles $\theta_w$ and $\phi$ are known.

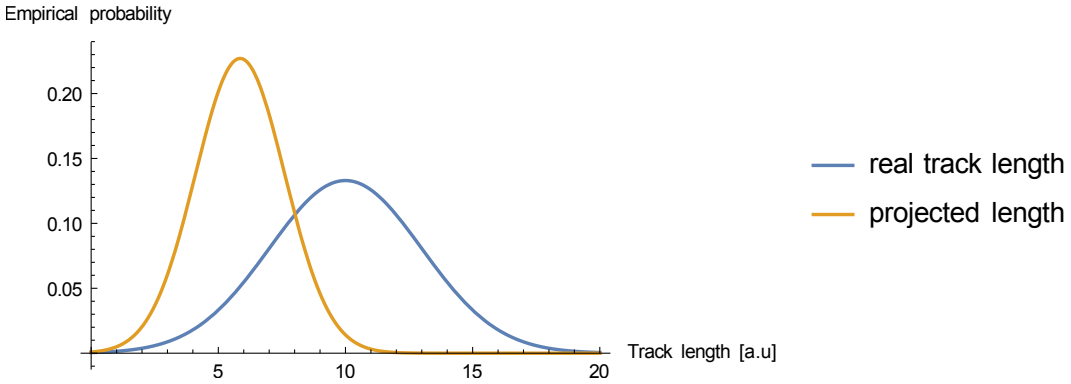


(a) Example for a gaussian distributed tracklength. The real tracklength equally distributed in 3-dimensions and the projection in one readout direction are shown

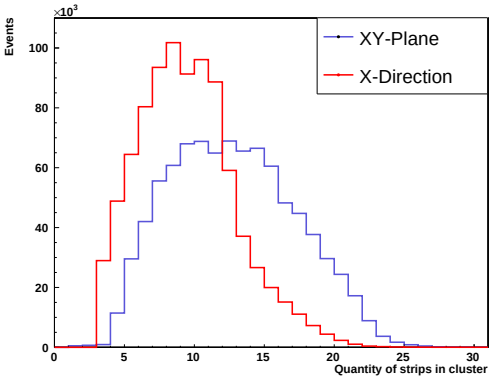


(b) Comparison of 2-dimensionally measured projected tracklengths on the readout plane and in the readout direction for products of a $^{10}$B + n reaction (see chapter 9)

Figure 3.10: Difference between real track length and projection into the readout plane or readout direction

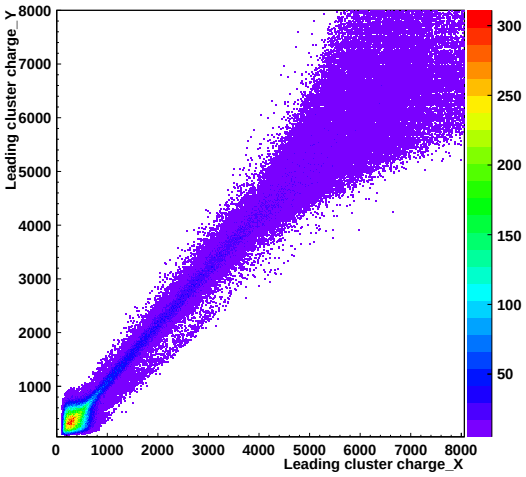


(a) Measured charge in both readout directions for irradiation with neutrons

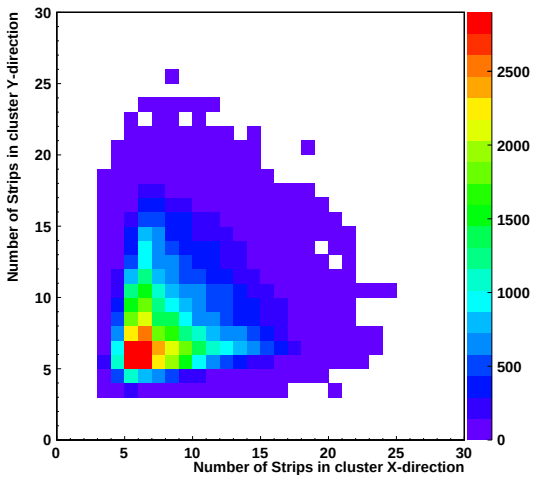


(b) Distribution of hit strips in both readout directions. A direct correlation of the length in both direction is not expected.

Figure 3.11: Charge and hit strips recorded with a two-dimensional readout

# 4 Simulations

In order to fully understand the behavior of the detector and to simplify the optimization for different applications it is suggestive to model the detector virtually and simulate it. This has been done for the GEM-detector with two different tool kits, which can simulate the production of electrons in the medium and the drift and multiplication processes. In this chapter the simulations and programs used are described. Simulation and measurement are compared in the following chapters.

## 4.1 Garfield electron drift and avalanche simulations

"Garfield" - and in this particular case "Garfield++"- is a tool kit for the simulation of gaseous detectors (see [28]). It has been developed by R. Veenhof at CERN. The transport properties in the gas are taken from the "Magboltz" database [29] and the electron drift and multiplication is calculated. The electronic signals induced by avalanches can also be calculated on sensitive areas inside the detector. Garfield is perfectly suitable to optimize the behavior of the detector with different gas mixtures and electric fields. Additionally the package "Heed++" (see [30]) can be used to simulate the response to charged incident particles like muons or also photons.

Garfield needs a finite element model of the detector as input and tables of the electric and magnetic fields inside this geometry. The raw geometry of the detector was built with gmsh, an open source mesher that reproduces the geometry and splits it into pieces in order to apply finite element methods to obtain the electrostatics. The calculation of the electric fields is done by Elmer, which calculates the electric fields and potentials in the detector and delivers the input to Garfield (described in [31] and [32]).

It is not necessary to rebuild the whole detector in gmsh since Garfield and Elmer are capable of using symmetry conditions. The unit cell of the detector as described in [33] is shown in figure 4.1. The geometry of the detector was simplified and contained the gaseous volume, the GEM-foils and bounding planes for cathode and anode. Neither readout or the housing, nor structural elements in the detector were simulated.

A single gas or a gas mixture is loaded and initialized from the Magboltz tables and the temperature and pressure are set. Additionally the Penning-effect can be enabled and the parameters for it can be forwarded to Magboltz (see [9], also all parameters for the simulation of this effect are taken from there).

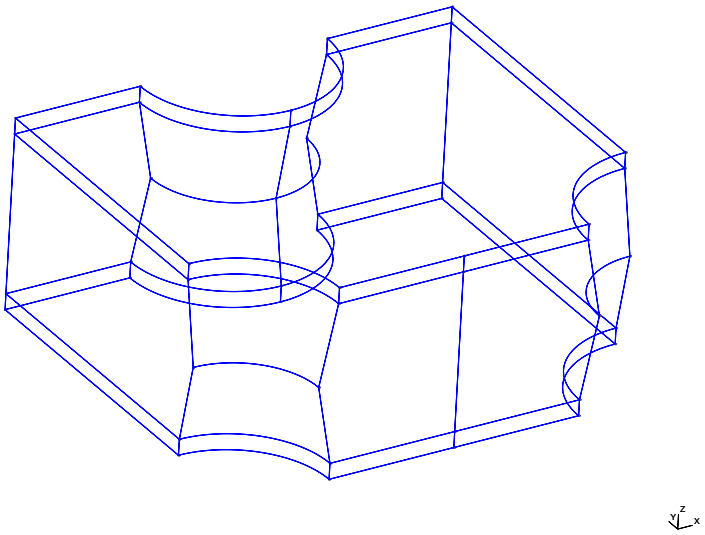

Figure 4.1: Unit cell of a single GEM-foil. The whole GEM-foil was modelled by utilization of the periodicity of this cell.

The last step before the simulation would be the placement of an initial electron inside the detector. This can be done either by placing it at an arbitrary position or by using Heed, which will simulate an ionizing particle and create electrons along its track or a photoelectron.

The simulation of the electron avalanche and drift is then iterated in multiple steps:

1. Electron position, direction, initial energy and time are used to determine its mean free path
2. Step length and diffusion coefficients are calculated
3. Diffusion is generated with Gaussian distribution
4. Multiplication of the electron is calculated by means of the Townsend coefficient
5. The position of the electron is updated and newly generated electrons from the step before get their initial parameters
6. The iteration then breaks if:
    a) The position is not inside the boundaries of the gaseous volume
    b) The electron recombines with an ion or is attached to a surface, which can happen with a certain probability defined in Magboltz
7. If the electron is still alive the iteration begins again

For every electron initial and final energy, initial and final position, initial and final direction and a parameter which describes the reason for aborting the iteration (i.e boundary is hit, attachment, recombination or left the detector volume) is stored.

### 4.1.1 Charge spread

There are limiting factors for the single electron resolution in the production of an electron avalanche, besides the limitation in resolution caused by the readout structure itself. Due to lateral diffusion of the electrons in the electric field and the granularity of the GEM-foils a charge cloud will be spread significantly after being proliferated in the GEM stages. To some extent this behavior is helpful in order to increase the multiplicity of hit strips, leading to a better charge averaging. This however works only if the spread is homogeneous and laterally symmetric to the electron drift.

## Single Electron Simulations

To evaluate the resolution limits the first step was to simulate the drift of a single electron and to reproduce its signal at the readout stage. Avalanches for single electrons and different setups of GEM-foils are shown in figure 4.2. The difference in gain and spread for the different amount of GEM-foils is apparent in those examples.

Minimizing the lateral diffusion in the detector should be possible in two ways. By reducing the drift distances in the detector and leaving all the fields at a consistent level the spread out would be reduced by reducing the drift time. This however is only a partially reasonable solution since too small gaps between the foils and especially the readout structure could lead to discharges and sparks. The second possibility is to improve the lateral diffusion by varying the electric fields in the detector. In order to do so single electrons are placed inside the detector and tracked down to the electrode. An accumulated hit pattern of 500 initial electrons with all secondary electrons can be seen in figure 4.1.1. All primary electrons were released at the same starting position at zero X and Y position and 1 mm above the uppermost GEM-foil. Since the diffusion in every step is simulated to be Gaussian the hit distribution naturally looks also Gaussian. A valid parameter for determining the resolution of the detector should then be the full-width-half-maximum (FWHM) of a Gaussian fit to the hit pattern (as also in [34] used).

The first step was to start with a simple single GEM-detector, Since a triple GEM configuration already has seven different electric fields to optimize. The three different fields in this case were varied independently of each other and the resolution determined for every field configuration. Figure 4.4(a) shows the theoretical resolution at the anode if the induction field is varied between 500 and 4000 $\mathrm{V\,cm^{-1}}$. The GEM potential difference was 300 V and the Drift field 1000 $\mathrm{V\,cm^{-1}}$. In figure 4.4(b) the simulated spread is plotted against the gain, due to the same variation of the induction field. The gain for lower values of electric field is limited, since the electrons are not well extracted from the GEM-holes.

Both plots show that the effect of this field is rather small. There is only a variation in the spread of about 10% to the mean value of 0.51 mm. Still a higher electric field seems favourable, since the gain drops quite significantly at lower electric fields

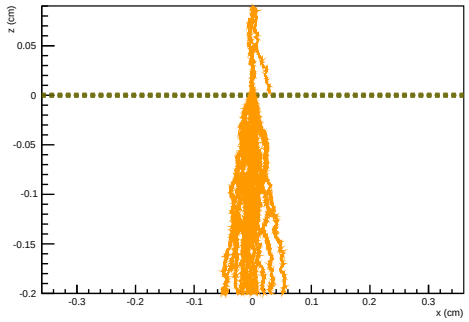


(a) Single electron avalanche through single GEM-Foil. A single electron track ending on the GEM-foil is also visible

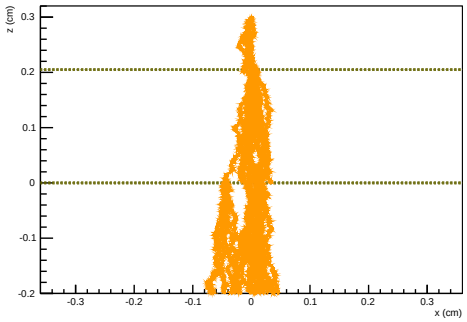


(b) Single electron avalanche through 2 GEM-foils.Voltage difference at each stage 300 V

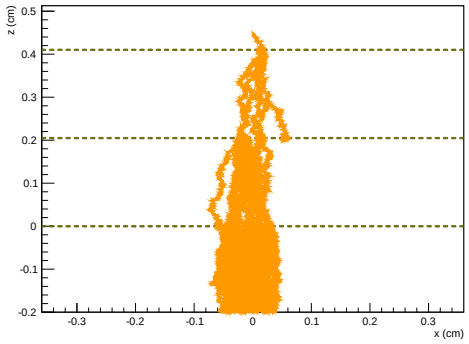


(c) Single electron avalanche trough 3 GEM-foils. Voltage difference at each stage 300 V. Tracks ending on a GEM-foil are also visible

Figure 4.2: Avalanche caused by a single electron for different GEM configurations Readout plane at -0.2 cm. The width of the electron hit distribution in the readout plane cannot directly be compared in these plots, since the number and density of electrons are very different (see figure 4.1.1)

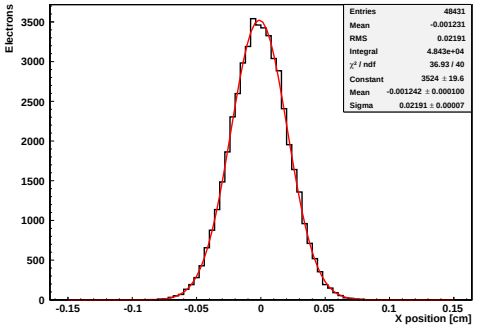


(a) Simulated accumulated deviation of electrons in the readout plane from position of the initial electron. Single GEM at 300 V potential difference and $E_{ind}$=3000 V/cm

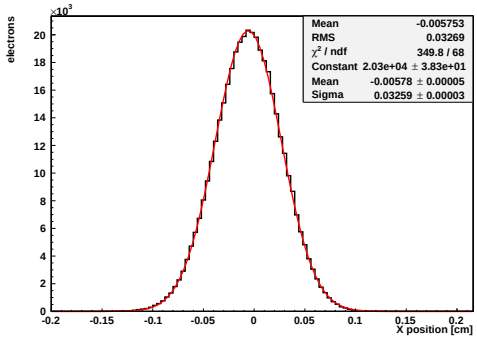


(b) Simulated accumulated electron position deviation for a triple GEM. $E_{Ind}$=$E_{Trans1}$=$E_{Trans2}$=2000 V/cm, $E_{Drift}$=700 V/cm, $\Delta GEM_1$=300 V, $\Delta GEM_2$=270 V and $\Delta GEM_3$=280 V

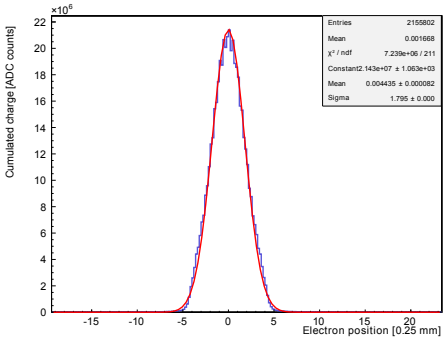


(c) Measured accumulated deviation of charge clusters for a triple GEM. The detector was irradiated with a $^{55}$Fe source, $E_{Ind}$=$E_{Trans1}$=$E_{Trans2}$=2000V/cm, $E_{Drift}$=700V/cm, $\Delta GEM_1$=300 V, $\Delta GEM_2$=270 V and $\Delta GEM_3$=280 V

Figure 4.3: Accumulated hit distributions of single events for 500 simulated electrons and 100000 measured photons. The agreement of measurement and simulation is shown in figure 4.6

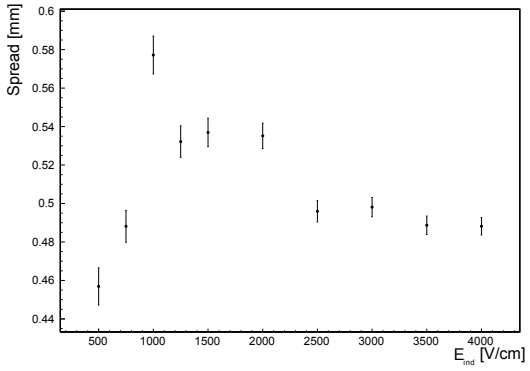


(a) Spread against $E_{ind}$.

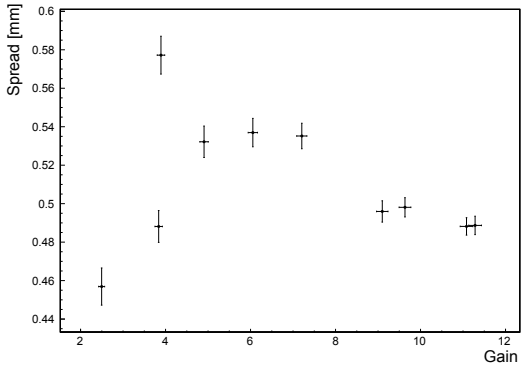


(b) Spread against gain due to variation of $E_{ind}$ given in (a)

Figure 4.4: Spread of the electron cloud at the readout plane, due to variation of $E_{ind}$. GEM potential 300 V and $E_{drift}$=1000 V/cm for a single GEM-foil

which limits the detection efficiency. A value between 3000 and 4000 $V\,cm^{-1}$ seems to be optimal in this case.

Keeping the induction and drift fields constant at 3000 $V\,cm^{-1}$ and 1000 $V\,cm^{-1}$ respectively, the GEM voltage difference has been changed in the range between 200 and 400 V. The lower limit of 200 V has been chosen according to the expected gain. As it can be seen in figure 4.5(b) the gain at 200 V is about 1. This is equivalent to no amplification and merely transport of the electron through the GEM. The upper limit however is an empirical value that reflects the usability of the GEM foils in an Ar-$CO_2$ gas mixture. At higher voltage differences the detector is not stably operable and micro discharges are likely. In figure 4.5(a) the spread is plotted against the different amplification voltages. Again there are only slightly differences due to the variation of the voltage. Still voltages between 300 and 350 V seem most favourable in terms of spread. Also the gain in this voltage range between 20 and 48 is quite instructive for use in a triple GEM-detector.

Verification of these simulations over the whole range is quite difficult, since the trigger electronics is not capable of handling a single electron signal, neither is the amplification strong enough to be recorded by the APV25-chips.

To mimic a strongly localized start point of an electron a $^{55}Fe$ source was used, since

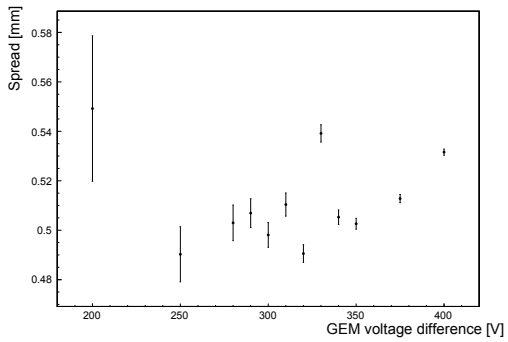


(a) Simulated spread against amplification voltage in single GEM-foil. $E_{Ind}$ = 3 kV/cm and $E_{Drift}$ = 1 kV/cm

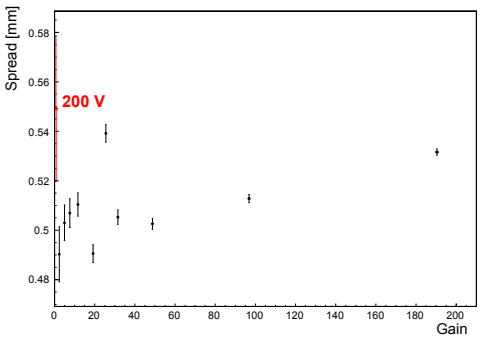


(b) Simulated spread against simulated gain for variation of the amplification field in a single GEM as are shown in (a)

Figure 4.5: Spread due to variation of the Amplification field

the range of a 5.9 keV photoelectron is limited to just about 70 µm in the gas (see chapter 5). In comparison to the strip pitch, the predicted spread and the predicted resolution this however is a neglectable range and therefore the initial electron cluster can be treated as perfectly localized. Still the amplification for the trigger is only high enough if a triple GEM-detector is used. Experimental spread of the cluster at the readout plane was then determined by the cluster size, i.e the number of strips per cluster. In the measurement the average number of strips per cluster was calculated by counting the strips in a cluster with a maximum charge of more than 45 ADC counts. To get a similar threshold for the simulated data, measurement and simulation were normalized to the peaks of the iron-spectrum. This sets the threshold for the simulation to 5800 electrons per mm to be the threshold for the left and right limit of the cluster. Experimentally the voltage of the uppermost GEM-surface ($U_{G3O}$) was alternated and therefore the amplification voltage of the uppermost GEM. All other electric fields were kept constant at $E_{Ind}$=$E_{Trans1}$=$E_{Trans2}$=2000 V cm$^{-1}$, $E_{Drift}$=700 V cm$^{-1}$, $\Delta GEM_1$=300 V and $\Delta GEM_2$=270 V. The voltage of the lower side of the uppermost GEM was 1765 V.

Measured and simulated width of the clusters are shown in figure 4.6. In the respective error limits the values of simulation and measurement match. Which is a strong argument for the validity of the simulations.

Despite the simulated small dependency of the spread of the amplification voltage of a single GEM measurement and simulation for a triple GEM show a quite significant alteration. The reason for this are the different measuring methods of both calculated quantities. As it can be seen in figure 4.7, where the FWHM values of a Gaussian fit to the simulated data is shown. The difference in the measurement is just a threshold effect.

## Track of a charged particles

For the more realistic case of a track of charged electrons in the detector the problem of spread prevails. By just counting the number of strips, which see charge, one

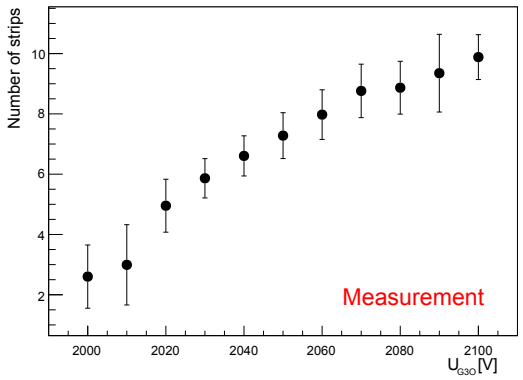


(a) Measured spread for different amplification voltages. All fields except the uppermost GEM field are kept constant. Here $U_G3O$ denotes the voltage applied to the top of the uppermost GEM-foil

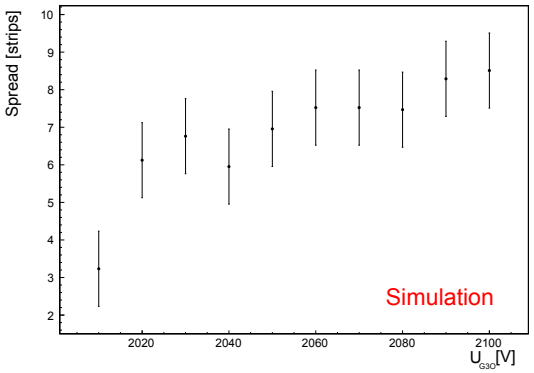


(b) Simulated spread for a triple GEM-detector against variation of the amplification voltage of the uppermost GEM-foil

Figure 4.6: Comparison between measurement and simulation of the lateral spread of an electron avalanche caused by a $^{55}$Fe source

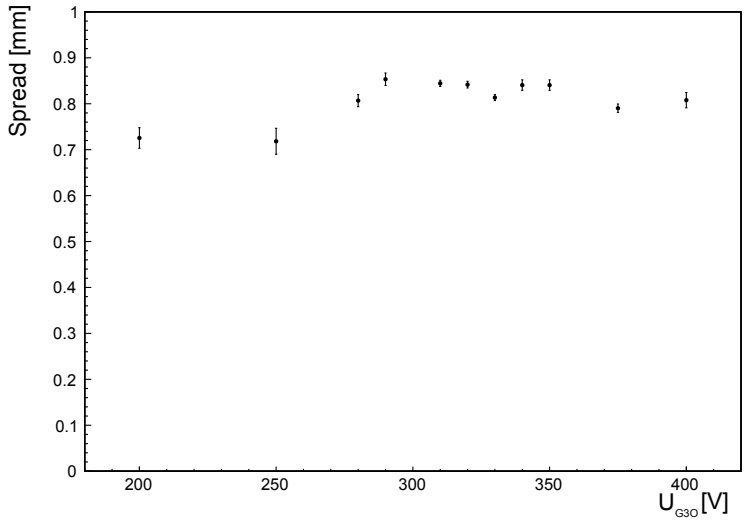


Figure 4.7: Simulated spread (FWHM) of single electron clouds in triple GEM.

would reconstruct the track projection too long. In order to mimic the track of a charged particle, with sufficiently high energy to get a straight track, single electrons were placed equidistantly in the detector. The track length was set to 6 mm consisting of 200 equally distributed electrons. The signal in the readout plane is integrated over time to obtain the charge collection. The track is then reconstructed by the μTPC-algorithm and the charge cluster profiled along this track. The width of the track is then calculated by the positions where the distribution exceeds a threshold of 5800 electrons per mm (equivalent to 45 ADC counts). The charge averaged cluster position ($\mathrm{pos}_{cluster}$) was then determined. Since the initial position ($\mathrm{pos}_{init}$) of the track was known, the distance of this position to the borders of the distribution on the readout plane could be calculated in units of the width of the track.

$$\epsilon = \frac{\mathrm{pos}_{init} - \mathrm{pos}_{cluster}}{\text{width of track}} \tag{4.1}$$

In figure 4.9 the ratio $\epsilon$ of the distance of the starting point of the track to the charge averaged cluster position to the width of the track is plotted for different track inclinations. The value of this ratio shows, that neither the position of the first strip in a charge cluster nor the charge averaged cluster position determine the start point of a track for all inclination angles. With these correction factors however the reconstruction of the start point of a track in the detector should be possible and therefore increase the effective resolution.

### 4.1.2 Angular resolution limits

The reconstruction of the inclination angle has obvious limits, as it is for example not possible to distinguish the case of perpendicular and parallel incident to the readout plane. Both cases are characterized by no difference in the arrival times of the electrons on all strips. To find the region for which this reconstruction delivers viable results, tracks with different inclination were simulated. In order to find the actual

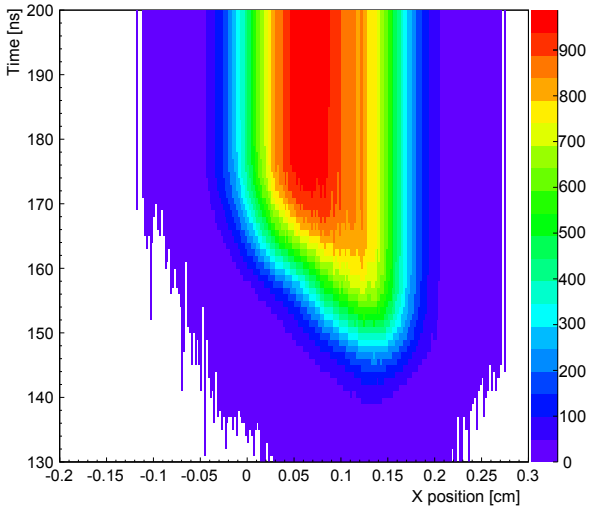


(a) Simulated charge signal of a track consisting of 200 primary elctrons in a triple GEM

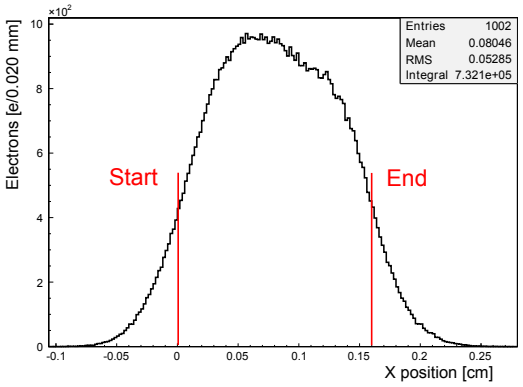


(b) Profile of charge distribution along the track . Position of first and last electrons are marked

Figure 4.8: Simulation of a track of a charged particle with homogeneous energy loss along its path

limitations due to spread of the charge cloud and the detector geometry, the strength of the drift field for this simulation was chosen to be as low as reasonably achievable with an actual detector. The idea behind this was to overcome the limitations of timing resolution of the readout electronics. This led to a rather low drift velocity of $12\,\mu m\,ns^{-1}$. Tracks of 1 mm and 6 mm length were simulated containing 75 equally spaced electrons for angles between 5° and 80°. The electron distribution at the readout plane was integrated over time and then bin wise treated the same way as the measured data in the spatial direction. The charge distribution for every bin of the space direction was fitted with an Arctan-function. The start time for every bin was extrapolated and a straight line was fitted to all starting times. The only difference to the data coming from real measurements was the binning of both, the time and the space coordinate. The binning in time direction was 1 ns and for the space coordinate a binning of 20 µm was used. In figure 4.10 the results for both track lengths are shown. The reconstruction of longer tracks works much better,

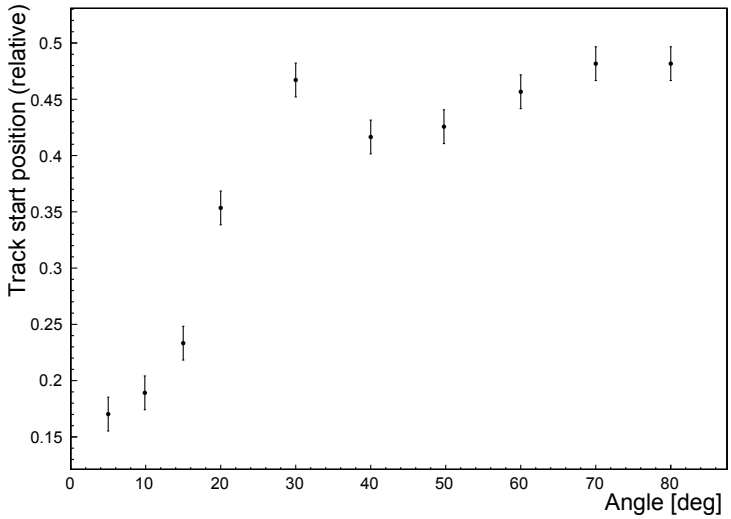


Figure 4.9: Simulated ratio of track width associated to the starting point of a track in x-direction

beginning at angles from 10°. The reconstruction is correct within the errors of the reconstruction up to 80°. On the other hand angles of short tracks in the range from 30 to 70 degrees still can be reconstructed with reasonable accuracy. In both cases the reconstruction fails completely at very low angles. Since this simulation is very time consuming only five tracks could be simulated per angle. The values represent the mean values of the reconstructed angles and their respective standard deviations.

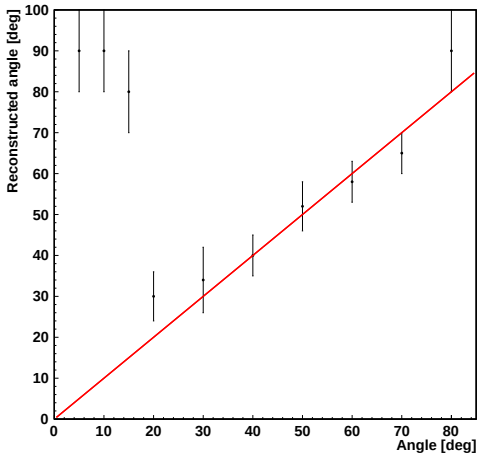


(a) Simulated reconstruction of track angle for a homogenous track of 75 electrons with a length of 1 mm

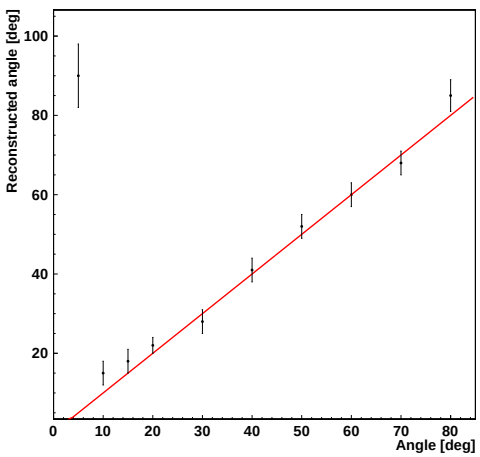


(b) Simulated reconstruction of track angle for a homogenous track of 75 electrons with a length of 6 mm

Figure 4.10: Simulated angle reconstruction for tracks of 1 and 6 mm length

### 4.1.3 Gas studies

The signal shape and timing is dependent mostly on two factors: The electric fields in the detector and the drift velocity of the electrons. The drift velocity is a function of the applied electric fields but also strongly depending on the gas mixture. This can be seen in figure 4.11. The simulated drift velocities are a main input parameter for the reconstruction of the inclination angle of tracks inside the detector.

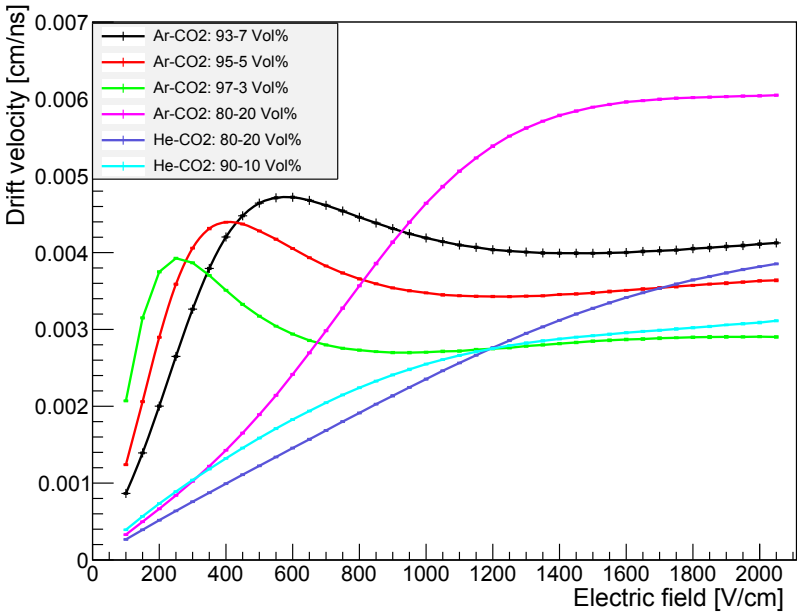


Figure 4.11: Simulated drift velocities of the electrons as function of the electric field in the drift region for different gas mixtures. All simulations at 1013 mbar and 293 K, which is a good working point for the detector

In order to optimize the angular resolution of the detector it might be useful to decrease the drift velocity of the electrons (see chapter 9). Therefore other gases and gas mixtures than the standard ATLAS Ar-$CO_2$ mixture might be favourable, as it can be seen in figure 4.11 helium mixtures would allow for drift velocities, which are a factor of four lower than those in argon based mixtures. Helium might be a future candidate also because of the lower stopping power causing tracks, which are a factor of three longer than those in argon for charged particles. This might be especially useful at the reconstruction of low angles for highly ionizing particles for example in the detection of neutrons with a converter foil (see chapter 9).

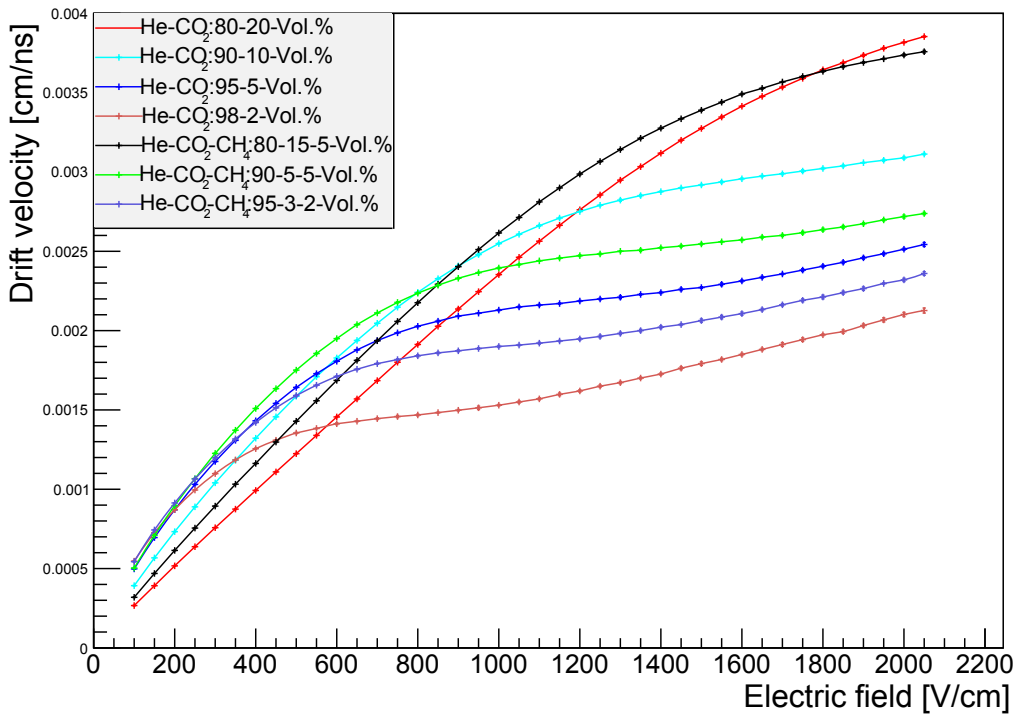


Figure 4.12: Electron drift velocities for different helium based gas mixtures. All simulations at 1013 mbar and 293 K.

## 4.2 Monte Carlo simulations based on Geant4

Geant4 [4] is also a Monte-Carlo based simulations tool kit but with far more applications than Garfield. Geant can handle any kind of physical process and radiation (see [35] and [36]). For the simulation the detector was modelled directly in Geant by predefined shapes. In contrast to the modelling for the Garfield simulations the housing, the cathode and the readout panel were modelled and also all elements inside the detector, like the plastic bolts, that hold the GEM-foils in place, and the frames of the GEM-foils [5]. For the drift region a constant electric field was applied. All other fields were neglected since the drift of electrons through the whole detector should not be simulated by Geant. The tracking of particles in Geant is very similar to the tracking in Garfield. In contrast to Garfield all kinds of particles are tracked. The particles are tracked to a minimal energy corresponding to a definable range, here 10 nm. For secondary particles the creation process, the mother particle and the point of creation are also logged (see [38]).

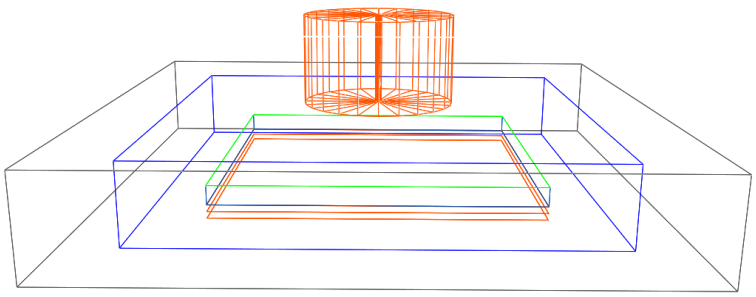

Figure 4.13: Simplified wire frame scheme of the detector geometry used for the simulations. The frames of GEM-foils and collimator are orange, the cathodes are green, the gas volumes are blue and the ones of the housing are grey

### 4.2.1 Energy loss

The signal that is produced in the detector is in general proportional to the energy deposit inside the drift volume. The detector however does not directly measure the energy deposited in the active volume, but the charge that is produced by this deposition. Since this is a stochastic process the number of electrons produced for a particle of fixed energy and energy loss is blurred out by the ionization process. This can be seen in the simulations in figure 4.14 at the example of the energy deposition

4 All simulations in this thesis have been carried out with version 4.10.0p2

5 The simulations in this thesis are based on the example simulation "EM8" from the standard Geant installation (see [37]), which was strongly modified

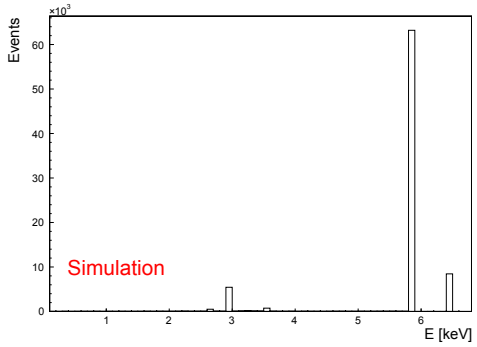


(a) Simulated energy deposition in the drift volime for a $^{55}$Fe source. At 6 mm drift space and with a 466 nm gold coated cathode

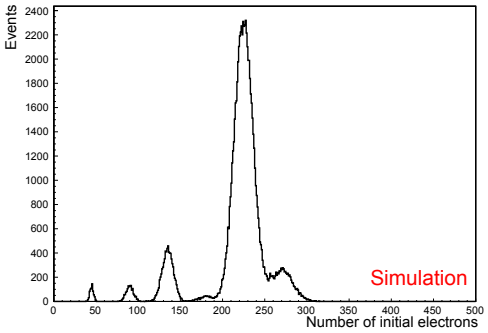


(b) Simulated amount of electrons produced by photoelectrons for $^{55}$Fe source. At 6 mm drift space and with a 466 nm gold coated cathode, the width of the distributions for every energy is limited by poisson statistics and proportional to the square root of the number of produced electrons

Figure 4.14: Simulated energy and charge deposition inside the detector

due to photons of a $^{55}$Fe source. The deposited energy is sharply defined, but the number of electrons produced by these photons is already blurred as it can be seen in figure 4.14(b). This spread is a gas characteristic and limited by the mean ionization potential. The width of the number of electrons produced by a photon in the gas can be described by Poisson statistics and would be $\sqrt{N \cdot F}$ where N is the mean number of electrons produced and F the so called Fano-factor, which is material dependent (see [5, p.118]).

The charge distribution in the active volume additionally is blurred out by the process of gas amplification which will lead to the final charge spectrum recorded in the readout plane. This spread is less drastic if the energy deposition is not sharply defined. This can be seen in figure 4.15 at the example of cosmic muons. The energy spectrum of the incoming muons was sampled from [39, p.218] with a most probable value of 4 GeV and a $\cos^2\theta$ distribution. The simulated distribution of electrons produced in the active volume and the measured amount of charge at the readout plane is shown for a measurement at the Cosmic-Ray-Facility (see also chapter 7). The shape and width of both distributions match, as expected, quite well to a Landau-distribution.

If the spectrum of the energy deposition is better defined and less broad the amplification process has to be considered in order to get competitive simulation results. This process can hardly be calculated by Geant directly, since the amplification process is very much dependent on the correct implementation of the electric fields in the detector. This however is very difficult to achieve in Geant. Nevertheless as Heed++ is only partly capable of reproducing the ionization processes that occur in the detector it was useful to let Geant simulate the first ionization process. Charged particles were tracked inside the active volume down to an energy below the mean ionization potential of the gas and the position of all secondary electrons was written to a file. For photons the Compton- or photoelectron was tracked and for neutron capture the respective products. The secondary electrons were

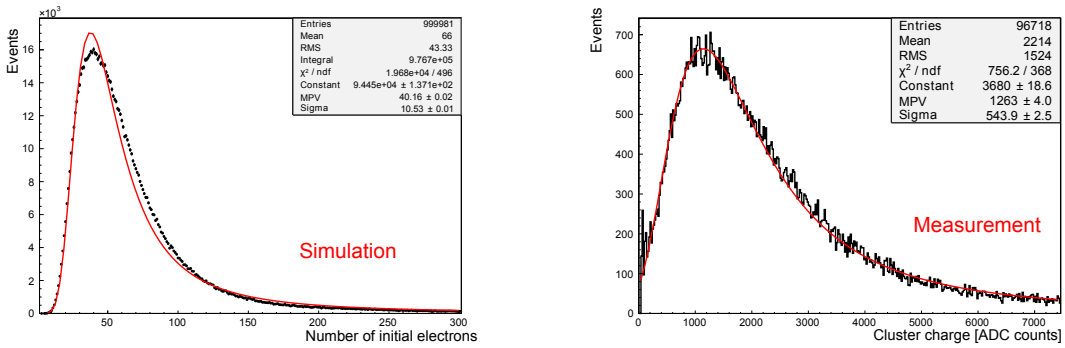


(a) Simulated distribution of amount of electrons produced in driftspace by cosmic muons for a driftspace of 10 mm of Ar-$CO_2$:93-7 Vol. % at normal conditions with 100 nm aluminized Kapton-cathode

(b) Meadured distribution of amount of electrons produced in driftspace by cosmic muons for a driftspace of 10 mm of Ar-$CO_2$:93-7 Vol. % at normal conditions with 0.1 µm aluminized Kapton-cathode at CRF (see chapter 7)

Figure 4.15: Simulated and measured charge deposition in the detector for cosmic muons

not tracked by Geant but immediately killed after their initial position had been recorded. The initial electron positions were then fed into a Garfield simulation to reproduce the amplification and drift process in the detector. The results of this simulation process can be seen in figure 4.16 for the case of a $^{55}$Fe and $^{55}$Ba source. The simulation was done for an aluminum-Kapton-cathode and the electric fields were $E_{Ind}$=$E_{Trans1}$=$E_{Trans2}$=2000 V cm$^{-1}$, $E_{Drift}$=700 V cm$^{-1}$, $\Delta GEM_1$=300 V, $\Delta GEM_2$=270 V and $\Delta GEM_3$=275 V and the drift space was 6 mm thick.

Muons and neutrons were simulated by placing them randomly in a plane of origin. The initial energy for neutrons was fixed to a constant value and for muons set randomly according to an energy distribution taken from [39][6]. The initial direction followed for neutrons was then randomly chosen from a isotropic distribution and for the muons from a $\cos^2\theta$-distribution. For the photon sources the geometry of the actual sources was modelled and the decay of the radioactive isotopes was simulated.

6 The energy distribution for perpendicular incident was chosen, but as the muons are minimal ionizing particles this should only have small effect on the energy deposition

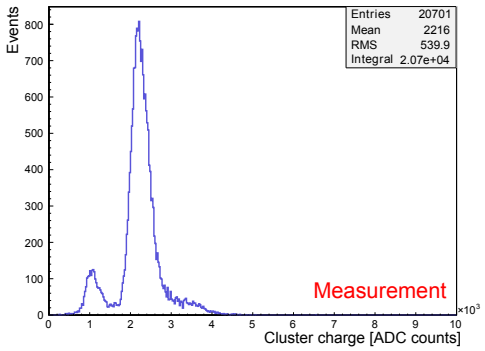


(a) Measured charge at readout plane for $^{55}$Fe source. Measured with a 466 nm gold coated cathode and 6 mm drift space

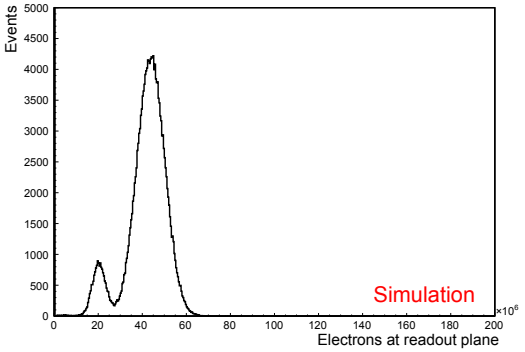


(b) Simulated charge at readout plane for $^{55}$Fe source. The wider distributions compared to figure 4.14(b) is due to the energy smearing caused by amplification in the GEM-foils

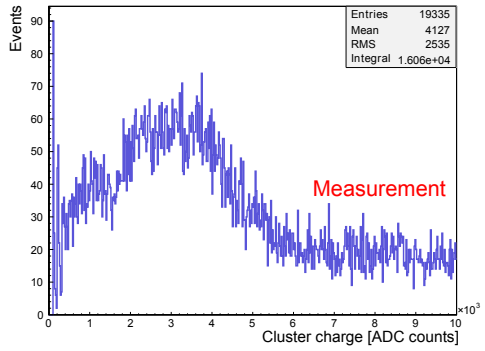


(c) Measured charge at readout plane for $^{133}$Ba source. Measured with a 466 nm gold coated cathode and 6 mm drift space

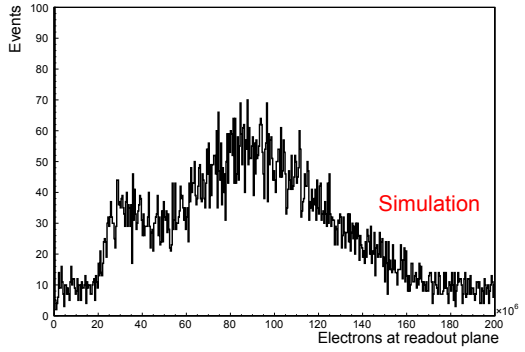


(d) Simulated charge at readout plane for $^{133}$Ba source

Figure 4.16: Simulated and measured charge for different photon energies

# 5 Photoelectron Tracking

Tracking of ionizing particles, which do not stop inside of the detector, or at least not inside the active volume, is comparably easy. Cosmic muons for example traverse the whole detector producing an average of 70 electron ion-pairs[7] per cm in Ar-$CO_2$:93-7 Vol.% at standard conditions without significant straggling[8]. Determining position and inclination of its track determines without further computation the direction the muon came from. In the case, if not the particle itself is detected, but a product of an reaction this is not quite as simple. The direction of the photoelectron and the direction of the incident photon are not the same. However the direction of the photoelectron is not totally arbitrary but confined at least to a spread cone relatively to the direction of the photon. Quantum mechanical calculations predict a distribution as is described in equation 5.1 (taken from [40, eq.52 p.91]).

$$J(\theta,\beta) = A \cdot \beta^2 \sin^2\theta \left( \frac{\sqrt{1-\beta^2}}{(1-\beta\cos\theta)^4} - \frac{1-\sqrt{1-\beta^2}}{2\sqrt{1-\beta^2}\,(1-\beta\cos\theta)^2} + \right. \\ \left. + \frac{2\left(1-\sqrt{1-\beta^2}\right)}{4\,(1-\beta\cos\theta)\,(1-\beta\cos\theta)^3} \right) \tag{5.1}$$

A is a normalization factor, $\beta$ the relativistic velocity and $\theta$ the angle of the photoelectron in comparison to the incident photon. Examples of distributions for different photon energies neglecting the electron binding energies is given in figure 5.1.

All values are normalized to the most probable value. This also shows the first difficulty in tracking photons by their photoelectrons, because of the distributions being very wide in the energy regime where the Photoelectric effect is dominant which is for most materials up to 50 keV, as it can be seen for some sample materials in table 5.1. An additional difficulty emerges from the fact, that the direction of the photon is only known up to the angle $\phi$, meaning that also by perfect reconstruction of the inclination angle the azimuthal angle is unknown and the direction of the incident photon only known up to a circle. This can be overcome by tracking more than one photon coming from the same source at different angles. This method is actually used in so called Compton-cameras, wich is as the name suggests the pendant with Compton scattered photons (see for example [41]).

7 See figure 4.15

8 0.2 mrad according to equation 7.2 in one cm of Argon

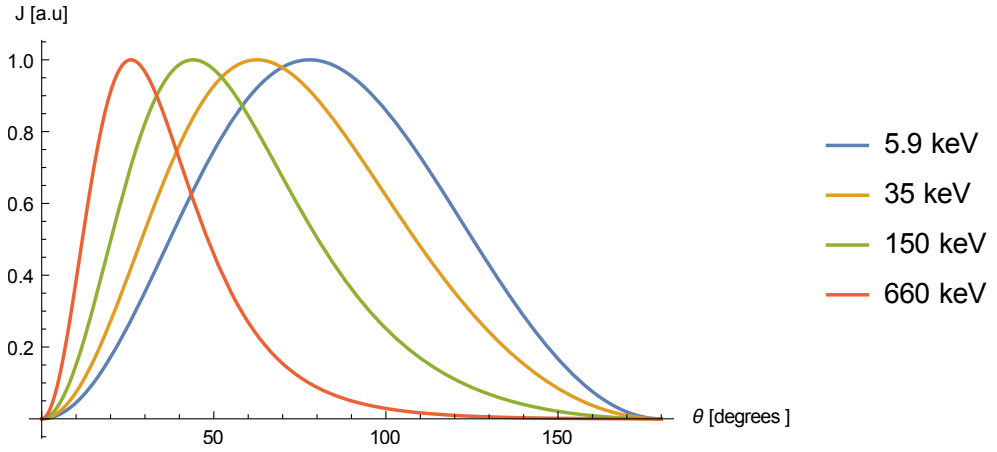


Figure 5.1: Angular distribution of photoelectrons direction relative to the photon direction (normalized to maximum) for different energies

Table 5.1: Photon energies for different materials where the cross sections for Compton-effect and Photoelectric-effect are equal (taken from [6]).

| Material | Energy |
|---|---|
| Aluminum | 53 keV |
| Copper | 130 keV |
| Gold | 55 keV |
| Iron | 120 keV |

To test whether this reconstruction with photons is in general possible the photons from radioactive sources were collimated to a divergence of 2° the same way as in chapter 6. Using a gold-coated cathode[9] the inclination angles of tracks in the detector were examined by the μTPC-methode. The reconstructed angle for a $^{133}$Ba source and a $^{55}$Fe source are shown in figure 5.2. Additionally the tracks were simulated in Geant and the projection in the X-direction of the angle of the photoelectron was calculated and is also shown for both photon energies. The cross section for Compton scattering in gold at 35 keV is only 29 b atom$^{-1}$ whereas the cross section for Photoelectric effect is 5633 b atom$^{-1}$ (see [6]), therefore its influence can be neglected.

Prediction and measurement for the case of the photons of higher energies fit comparably well, especially if considered that the reconstruction of angles works hardly for small angles. The behaviour for larger angles and the position of the local maximum is very similar in simulation and measurement. In the case of the photons with less than 10 keV energy for the $^{55}$Fe source however the reconstruction fails completely and there are hardly any similarities. The reason for the different quality of the outcome most likely lies in the ionization process itself. Photoelectrons of lower energy are far more straggled by traversing matter, therefore they do not ionize in a straight track. Photoelectrons of higher energy are also straggled, but far less and therefore keeping their initial direction long enough to produce a reconstructible track. In figure 5.3 sample tracks for both cases are shown. It is clearly visible that the initial direction of the photoelectron of lower energy cannot possibly be reconstructed

9 See chapter 8

by its track in the detector, quite in contrast to the track of a 35 keV photoelectron which nearly represents a straight line.

Both, measurement and simulations show, that the angle of a photoelectron in general can be reconstructed and therefore detection of the source of a photon might be possible.

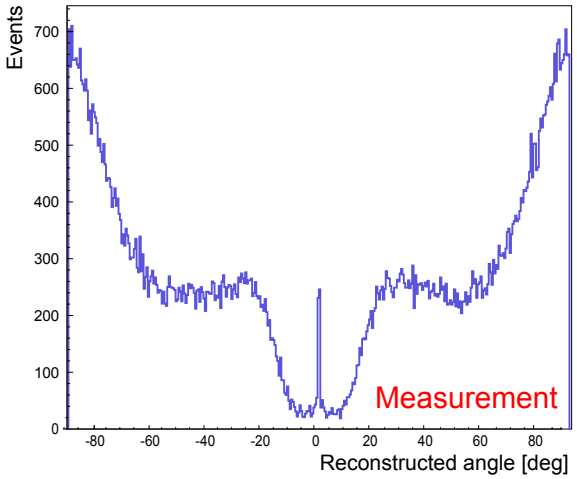


(a) Reconstructed angle for irradiation with collimated $^{133}$Ba-source. The peak at 0° is caused by the ambiguity in the reconstruction of perpendicular and parallel tracks with respect to the readout

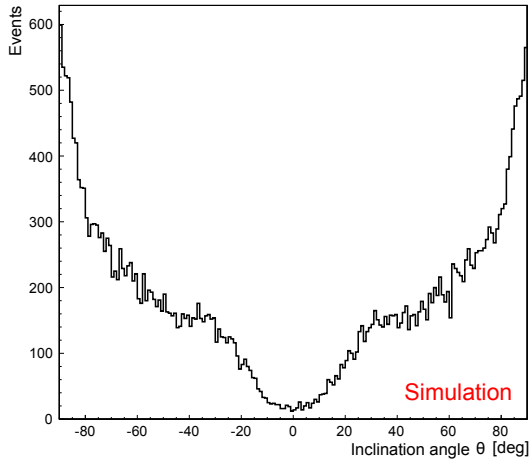


(b) Simulated angle of photoelectrons for perpendicular incident photons of 35 keV

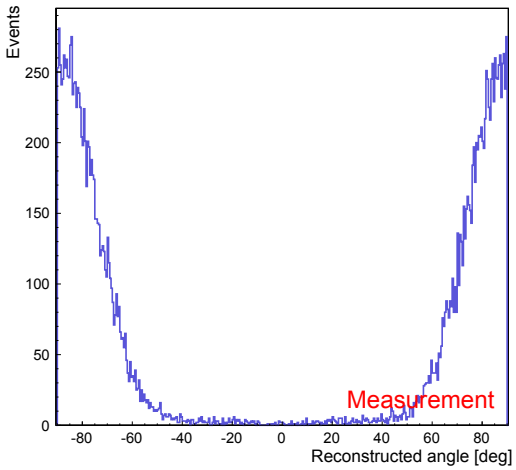


(c) Reconstructed angle for irradiation with collimated $^{55}$Fe-source

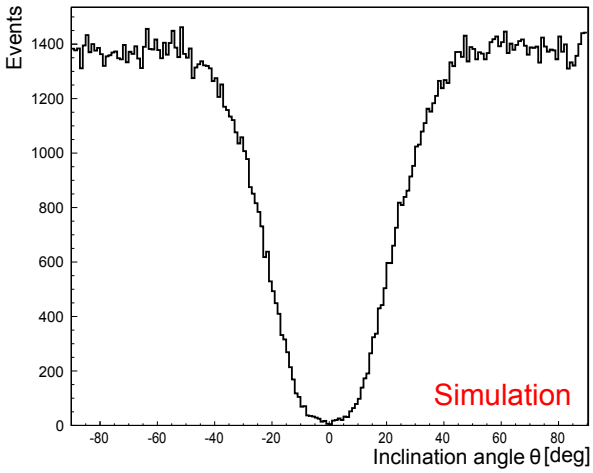


(d) Simulated angle of photoelectrons for perpendicular incident photons of 5.9 keV

Figure 5.2: Comparison of reconstructed and simulated angle of photoelectrons

Since these measurements could only be carried out with a one dimensional readout, tracking and reconstruction of sources was not possible with the reconstructed angles. The measurement however could be used as an input for a simulation.

Two point like sources of 35 keV were simulated, which were separated by 5 mm and a distance of 10 mm to the plane of interaction (cathode). The direction of photons for both sources was isotropic. If they reached the interaction plane an photoelectron

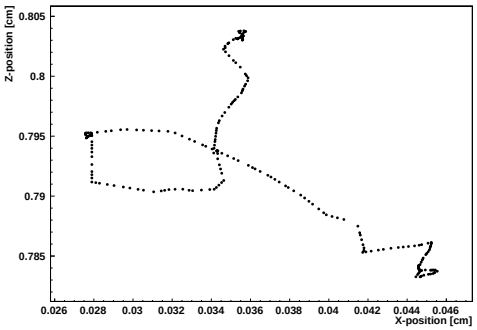


(a) Simulated track of a photoelectron of 5.9 keV in an Ar-$CO_2$:93-7 Vol.% gas mixture. In this plot the position of electrons, which were produced along the track of the primary electron, is shown. The drift due to the applied electric field is not considered

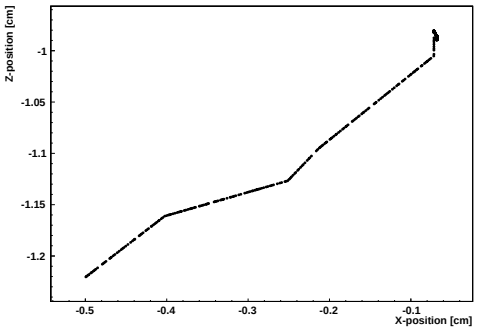


(b) Simulated track of a photoelectron of 35 keV in an Ar-$CO_2$:93-7 Vol.% gas mixture. In this plot the position of electrons, which were produced along the track of the primary electron, is shown. The drift due to the applied electric field is not considered

Figure 5.3: Tracks for 35 keV and 5.9 keV photoelectrons

was produced, which had a Gaussian distributed track length[10] of (12±2) mm and an inclination angle with respect to the incoming photon described by the distribution in equation 5.1. The azimuthal angle was randomized for every electron. In figure 5.4(a) the simulated charge averaged mean cluster position for all electron tracks is shown for 20000 photons being converted from every source. The hit distribution shows no features of two independent sources, but a broad peak at the center. To take also into account the reconstruction of the angles, the position of the conversion of the photons was randomized with a width of 0.5 mm to account for the error in reconstruction of the interaction point[11]. The last step was to use the difference between the simulated inclination of the electrons perpendicular to the readout and the mean inclination of 65° due to the photoelectric effect for this energy and draw cones with an opening angle of twice this angle. In figures 5.4(b) to 5.4(d) slices through these cones in different distance to the conversion plane parallel to it are shown. If the angular distribution were perfectly sharp, all cones would intersect for the first time at the position of the sources. This can help to reconstruct the distance of the source to the detector. Figure 5.4(b) shows the slice in 1 mm distance 5.4(c) in 10 mm distance and 5.4(d) in 20 mm distance. In the case of 1 and 20 mm there is only one peak apparent whereas for the slice in 10 mm distance two peaks at 0 and 5 mm in X-direction are clearly distinguishable. This however has not yet been validated with real data. It seems to be a very promising application since not only the resolution in two dimensions would be increased, but also the position in the third direction could be reconstructed.

10 Corresponding to the average track length of a photo electron in Ar-$CO_2$ simulated with Geant4

11 This corresponds to 5° error at an angle of 65° the mean inclination angle for perpendicular photons

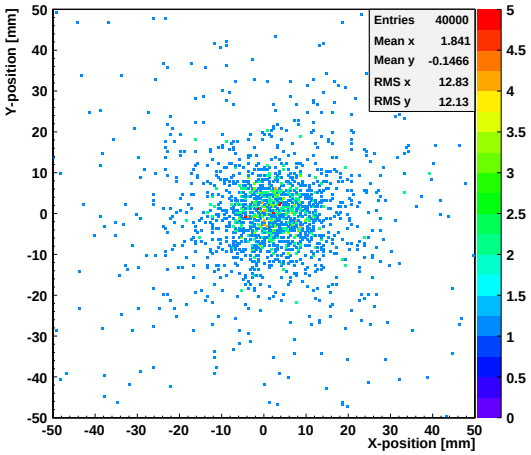


(a) Simulated cluster distibution in the detector for two isotropic photon sources

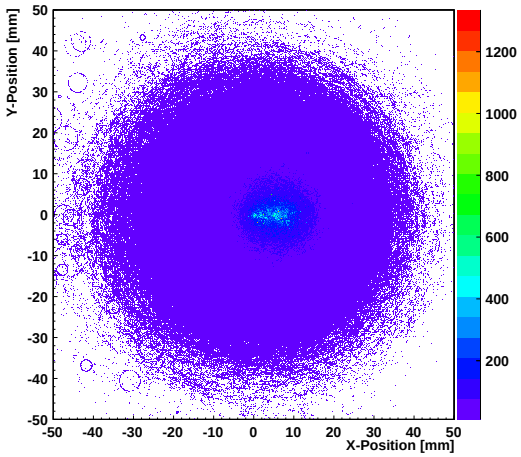


(b) Simulated reconstructed source position in 1 mm distance to the conversion layer

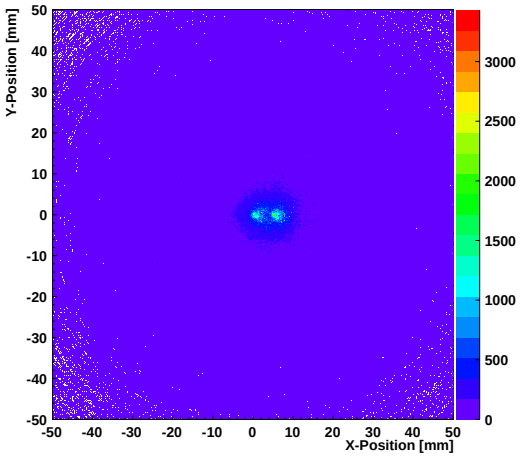


(c) Simulated reconstructed source position in 10 mm distance to the conversion layer

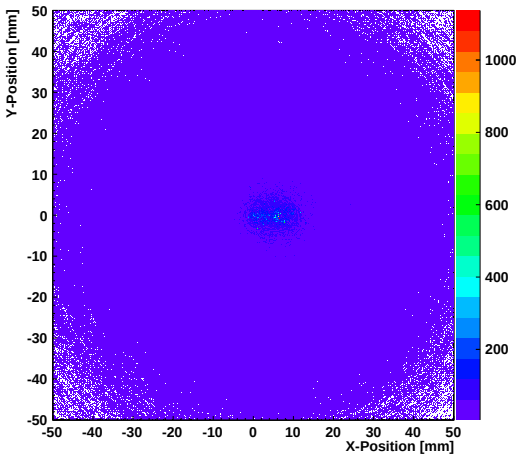


(d) Simulated reconstructed source position in 20 mm distance to the conversion layer

Figure 5.4: Simulated reconstruction possibilities of two point like photon sources

# 6 Spatial Resolution for a Single Object

Tracking of particles requires besides sufficient angular resolution a high spatial resolution to reconstruct the point of interaction. Since photons are scattered or converted in the process of detection the spatial resolution has to be determined in a single detector. In order to do so the minimal size of an object was measured, for which the detector is capable of detection of the shadow.

The setup consists of a 30 mm thick copper collimator with 2 mm diameter, which leads to an acceptance interval of -2°$< \theta <$ 2°. A single copper wire is placed parallel to the readout strips underneath the collimator but still outside of the detector. By varying the diameter of the wire and comparing the resulting shadow it is possible to extract the detector resolution. The tracks of photoelectrons of 5.9 keV energy are

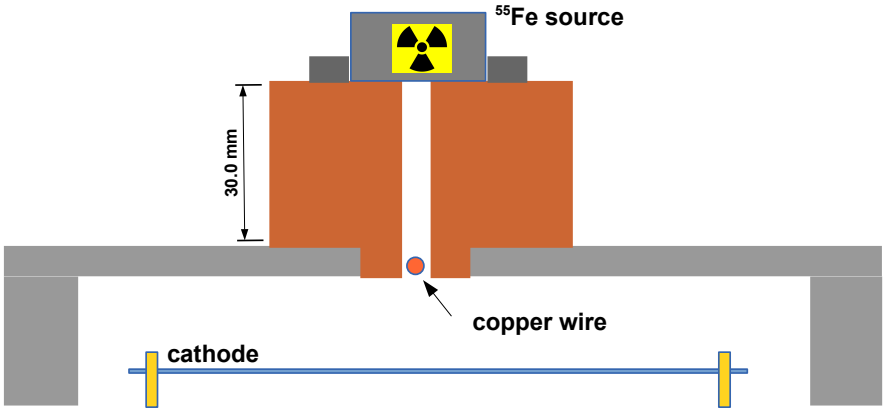


Figure 6.1: Illustration of the experimental setup

very short and can be considered point like in comparison with the lateral spread of the cluster, due to the amplification process. The range is about 70 µm (see chapter 4) and the spread of the charge cluster at the readout is about 800 µm. Therefore the strip multiplicity, i.e the strips that are hit per event, is always high enough to determine the mean of the cluster with high accuracy.

The resulting pattern should be a convolution of the flux from the source, described by the angle $\theta$ which describes the direction of the photons perpendicular to the flat source and a prefactor $I_0$:

$$\Phi(\theta) = I_0 \cdot \cos\theta \tag{6.1}$$

convoluted with the acceptance angle of the collimator in dependence of the inclination angle $\theta$ the distance from the center of the collimator $r - r_0$ and the thickness of the collimator $z_0$ (see also figure 6.2). $\mathcal{H}$ denotes the Heaviside step function:

$$A(\theta, r)|_{z_0} = (1 - \mathcal{H}(-r - r_0))\mathcal{H}(r_0 - r)\left(1 - \mathcal{H}\left(\theta - \tan^{-1}\left(\frac{r_0 - r}{z_0}\right)\right)\right. \\ \left. \cdot\mathcal{H}\left(\theta + \tan^{-1}\left(\frac{r + r_0}{z_0}\right)\right)\right) \tag{6.2}$$

And also convoluted with the conversion probability in the gas in the active volume[12] between $z_1$ and $z_2$:

$$I(z) = N_0\left[1 - e^{-\frac{z}{\mu}}\mathcal{H}(z_2 - z)\,\mathcal{H}(z_1 - z)\right] \tag{6.3}$$

Together with an assumed gaussian spread of the charge cloud, due to lateral diffusion the hit distribution cannot be calculated analytically, but can be approximated with a Fourier-expansion. This leads basically to a $\cos^2\rho$ distribution, where $\rho = r + \tan(\theta)z$, which is the distance of the conversion point to the axis of the collimator at the conversion point z.

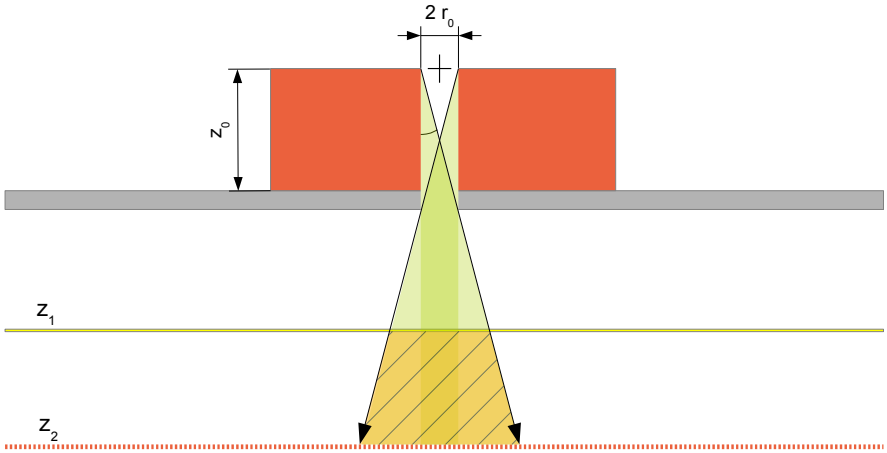


Figure 6.2: Description of the geometric features of the setup

The experimental hit distribution in the case of a collimated $^{55}$Fe source beam with a drift space of 10 mm is shown in figure 6.6(a) for $E_{Ind}$=$E_{Trans1}$=$E_{Trans2}$=2000 V cm$^{-1}$, $E_{Drift}$=700 V cm$^{-1}$, $\Delta GEM_1$=300 V, $\Delta GEM_2$=270 V and $\Delta GEM_3$=280 V. It is notable, that in the hit distribution periodic cuts are visible e.g at positions 109 and 113, as shown in figure 6.3, which kept the same absolute position in the detector even if the source was moved. Therefore it is most likely that they are due to geometric effects

12 This is a simplification, which treats all photons as if they were perpendicular to the readout plane. This is valid, since the collimation is quite well.

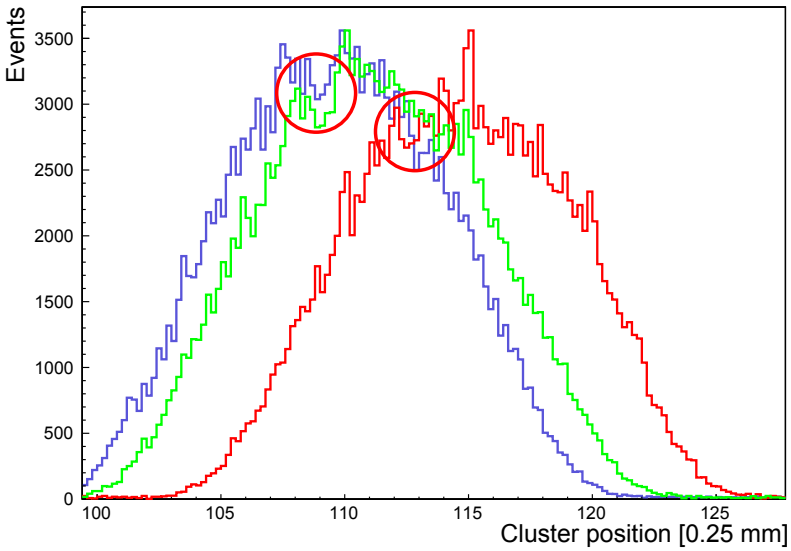


Figure 6.3: Hit distributions for three different positions of the collimator, the cuts in the distribution keep the same absolute position for example at strip position 109 and 113 (with slight statistic excess in the green pattern)

in the hit distribution caused by the structure of the GEMs itself. One would then see some pattern due to the hole structure of the GEMs[13].

This effect has to be considered when the hit distributions with wires are compared to that without a wire. If one would just subtract the hit distribution with wire from the distribution without wire these cuts would not be compensated. The depth of the cuts is proportional to the number of hits in the region of the cut therefore one would overestimate the number of hits in regions where there are few hits caused by the wire.

In order to compensate for this problem the analysis procedure was as follows:

- Fit of a $cos^2 x$ function to the distribution without wire
- Integrate over difference between fit and hit distribution with wire
- Iterate step 2 with a shifted hit distribution to compensate for slight displacement[14]
- Consider only the case where the integral is minimal.
- Fit a Gaussian to the resulting pattern.
- The amplitude of the Gaussian is the important item

Figure 6.7 shows the result for the different wire diameters and a fit with the function g that takes into account the amount of the beam, which is hidden by the wire (see also figure 6.4).

13 Although this patterns couldn't be reconstructed by simulations

14 Actually the perfect displacement was always zero. So the displacement between the measurements was always better than a strip pitch

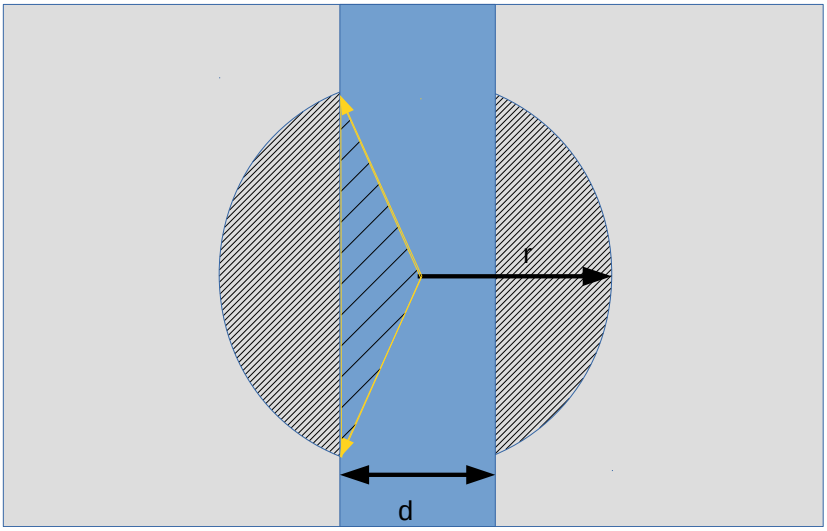


Figure 6.4: Scheme of the wire placed on the hole. The narrow hatched areas represent the not shadowed areas and can be calculated by integrating between the two yellow arrows and subtracting the wide hatched triangle.

$$g(d) = \frac{1}{\pi}\left(\pi - 4\sin d + 2d\sqrt{1-d^2}\right) \tag{6.4}$$

Where d is the relative wire diameter in comparison to the diameter of the hole. A criterion for the determination of the resolution could be a modified Rayleigh criterion. In optics this criterion describes the resolving of two Airy disks in the limit of the diffraction of the light. The main maxima of two Airy disks have to be separated by at least the distance of the first minimum to the center.

This leads in superposition of both disks to a combined local minimum at half of that distance with 73.5 % intensity compared to the maxima. This criterion represents the shape of the actual $\cos^2 x$ hit distribution quite well.

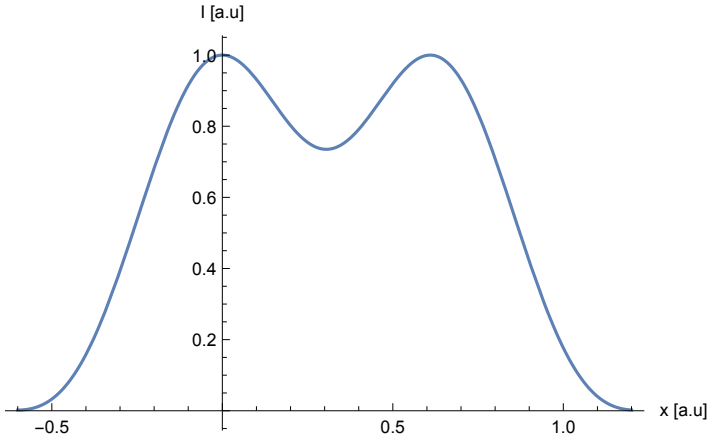


Figure 6.5: Two Bessel functions representing the Rayleigh criterion

The limit predicted by the Rayleigh criterion would corresponds to a wire diameter of 70 µm, meaning that in this configuration the detector would be capable of detecting single objects down to that size. Since the fit to data points seems to overestimate the deviation for small objects and the structure of the hit distribution has a periodic

structure of about the same size, it is more reasonable to use a resolution criterion of a deviation of 40 % in the same sense. This would lead to a minimum object size of 150 µm.

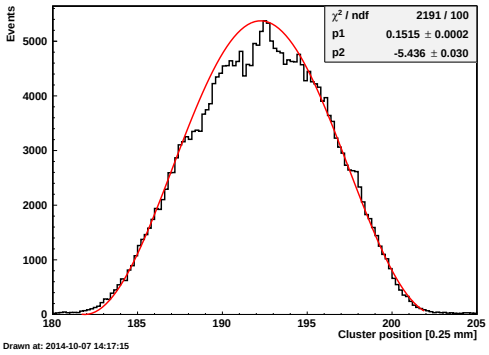


(a) Hit pattern of collimated beam without wire and $\cos^2 x$-fit to the distribution

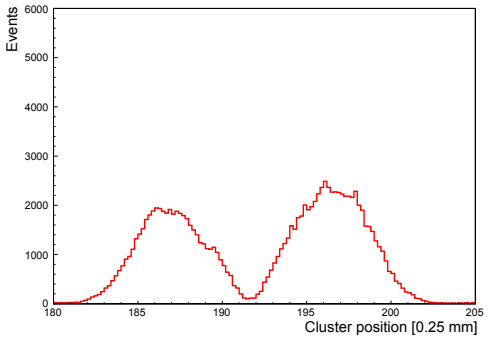


(b) Hit pattern of collimated beam with 1 mm copper wire placed on the detector cover

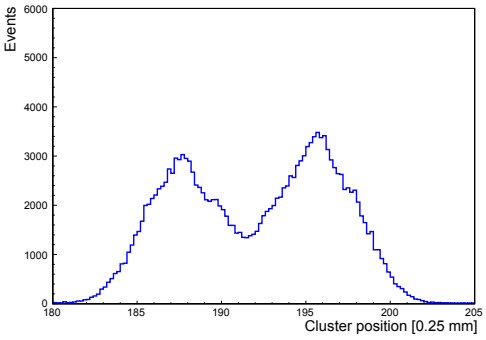


(c) Hit pattern of collimated beam with 0.6 mm wire

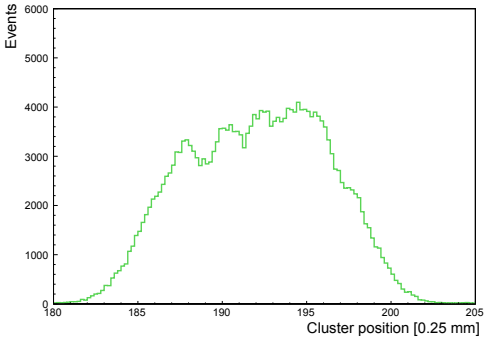


(d) Hit pattern of collimated beam with 0.2 mm copper wire

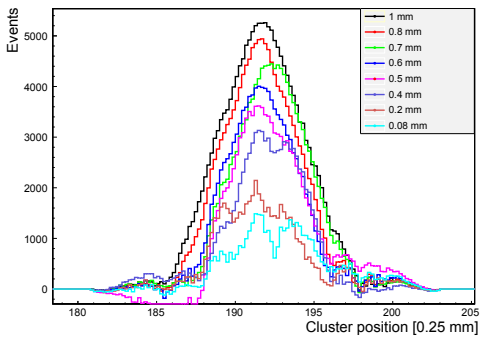


(e) Difference in hit pattern between irradiation with and without wire for different wire diameters

Figure 6.6: Comparison of hit patterns with and without wire

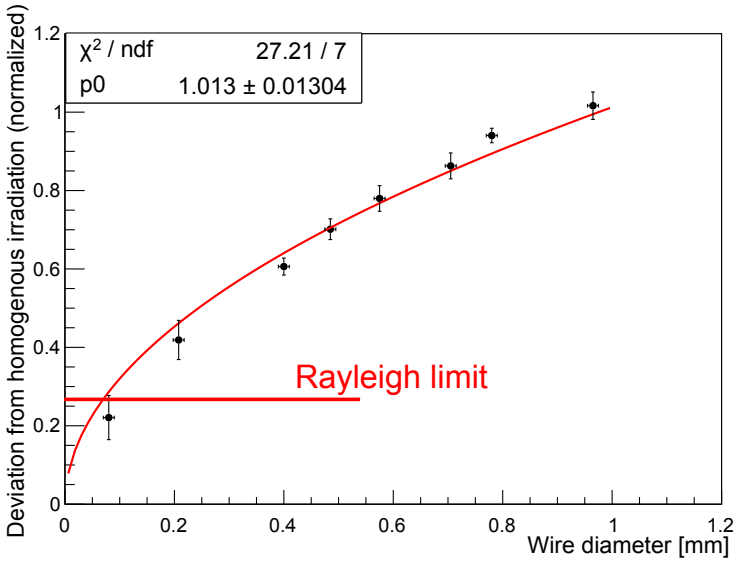


Figure 6.7: Relative deviation of the hit pattern in correlation to the wire diameter with fit function 6.4 under Rayleigh limit at (1-0.735)=0.265

# 7 Muon tracking

Cosmic muons are minimal ionizing particles (MIPs) with a mean energy of 4 GeV (see [39]). At an energy loss of about 2 $\frac{MeV \cdot cm^2}{g}$ they can traverse a whole system of detectors without being stopped and still being tracked. Additionally muons straggle hardly in matter and can therefore quite easily be tracked. Scattering for muons can be described by multiple scattering in the Gaussian limit:

$$\frac{dN}{d\theta} = \frac{1}{2\pi\theta_0^2} e^{\frac{\theta^2}{2\theta_0^2}} \tag{7.1}$$

using the Fermi approximation

$$\theta_0 = \frac{13.6MeV}{\beta cp}\sqrt{\frac{l}{X_0}}\left[1 + 0.038\ln\left(\frac{l}{X_0}\right)\right] \tag{7.2}$$

Here $\beta$ and p are the relativistic velocity and momentum of the muon and $l/X_0$ is the thickness of the medium in units of radiation lengths (see [3]).

## 7.1 Tracking with a GEM-doublet

In order to validate the results of the μTPC angle reconstruction two detectors were used to determine the inclination angle of incoming muons. The detectors were placed back-to-front atop of each other and sandwiched by two trigger scintillators, as it is illustrated in figure 7.1. Both detectors had one-dimensional strip readout and the same electric fields were applied. The only difference between them was the distance between the last GEM and the anode, being 3 mm for the upper detector and 2 mm for the lower detector. The idea was to determine differences in the angular resolution with respect to the different rise time of the signals, due to longer drift time[15].

The reference angle was calculated from the measured position of the tracks.

$$\theta = \arctan\frac{x_1 - x_2}{\Delta z} \tag{7.3}$$

15 This has not been done in subsequent measurements, due to arising from the long signal rise times. The signals jitter that much in time, that up to 20 % are not entirely recorded

$x_1$ and $x_2$ are the center of mass positions in the respective detectors and $\Delta z$ the distance between both drift spaces, using the assumption that the center of mass of the track in fact corresponds to the center of the drift space in z-direction.

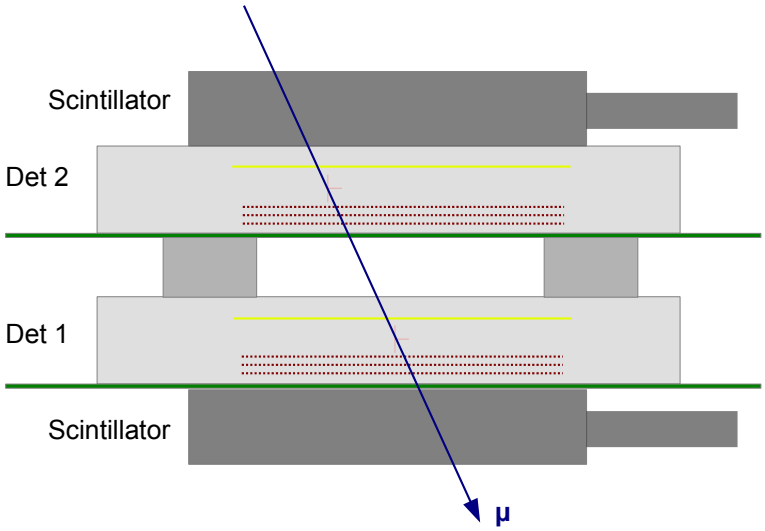


Figure 7.1: Illustration of the experimental setup with two triple GEM-detectors and tigger scintillators. The red crosses indicate the reconstructed position of the track in the middle of the drift space.

The reconstructed angles are shown in figure 7.2. Here only events are shown, which produced a signal in both detectors. Also the signal had to start and end between the 5th and 20th time bin. This led to a quite poor angular reconstruction for the lower detector, where the signals start typically earlier, due to the narrower induction gap. This time window was chosen, because of the upper detector and its wider induction gap, where the reconstruction works much better.

The main purpose of this measurement was to determine the correction factor, that has to be applied to correct for charge coupling of two neighbouring strips, which was described in section 3.3. In order to do so the residual between the reconstructed angle and the reference angle was calculated for different correction factors. The root mean square of the distributions was calculated and normalized to the value without correction. The results for the upper detector are shown in figure 7.3. The correction seems to improve the reconstruction up to a value of about 0.2. Higher correction factors impair the reconstruction quality again. This shows, that this correction can improve the reconstruction of the angles by about 10 %. Whenever the charge was corrected in further analysis this factor of 0.2 has been used.

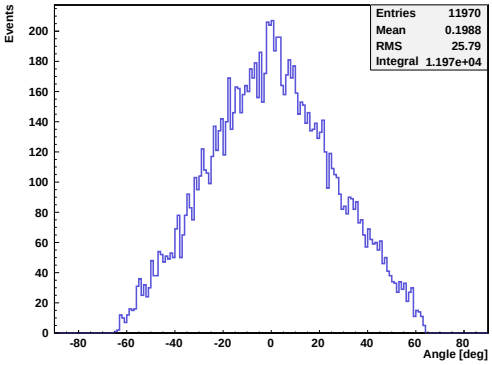


(a) Reference angle calculated from cluster position in both detectors, the distribution is the combination of the angular distibution of the incomming muons combined with the angular limit of this setup of about 60°

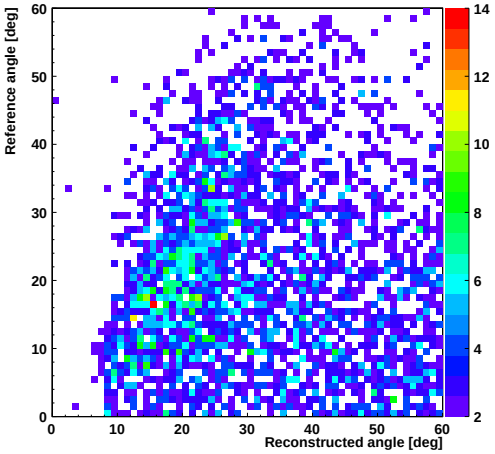


(b) Reference angle against the reconstructed angle in the upper detector without correction

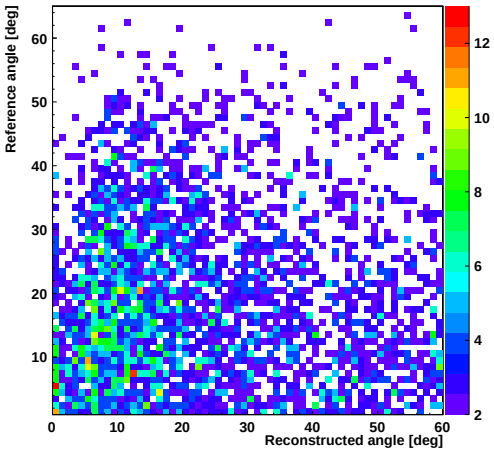


(c) Reference angle against the reconstructed angle in the lower detector without correction. Unfortunate trigger timing due to a different induction gap led to the poor angular reconstruction

Figure 7.2: Reconstructed muon angles in both detectors

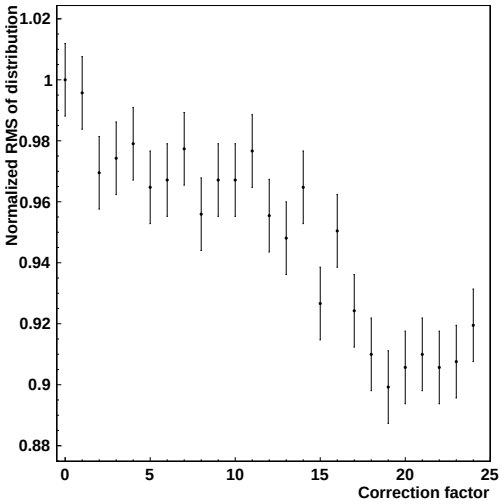


Figure 7.3: Normalized RMS between residuals of reconstructed and reference angle for the upper detector for different charge correction factors

## 7.2 Muon tracking at the Cosmic Ray Facility

The cosmic ray facility (CRF) in Garching is a test stand originally designed to calibrate ATLAS muon drift tubes [42]. The facility consists of two monitored drift tube chambers (MDTs), which are capable of tracking muons with a precision up to 70 µm in the precision direction perpendicular to the drift wires. Along the drift wires the resolution is given by two scintillator hodoscopes in the order of 5 cm. This setup can be used to get a spatial and angular reference for a GEM-detector between these chambers. The GEM-Detector was placed in the middle between the two MDT chambers with the readout strips orientated parallel to the drift tubes (see figure 7.4(a)).

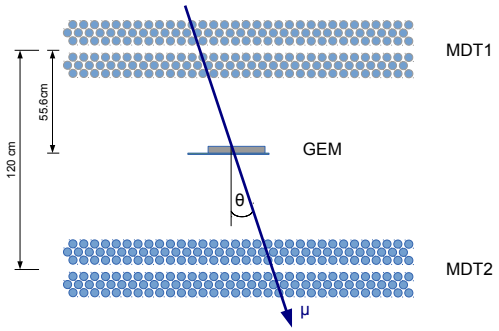


(a) Scheme of the experimental setup. A muon traverses both MDT-chambers and the GEM-detector. The inclination angle is calculated by a fit to the tubes hit in every chamber and compared with the reconstructed angle in the GEM-detector


(b) MDT chambers with GEM and trigger scintillators between the MDT chambers and the upper and lower scintillator hodoscopes

Figure 7.4: Illustration of the experimental setup in the CRF.

In both MDT-chambers the track of a muon is individually fitted to the single tube data, which yields position and inclination angle of the track. As reference for the GEM-detector measurement the average values of both chambers have been used.

### 7.2.1 Alignment of detector-systems

In order to combine the output of both detector systems the GEM-detector has to be aligned with the coordinate system of the MDT chambers. The course alignment is defined by the placement between the chambers, but the fine adjustment is realized in the analysis software [16]. The GEM-detector is virtually repositioned in the center between the chambers and parallel to them. Especially the tilting between the MDTs and the GEM-detector has to be considered, since the measured angles should be compared. How much the tilting impairs the spatial reconstruction can be seen in figure 7.5, where the residual between the cluster position in the GEM-detector and the prediction of the MDT-chambers is shown for perpendicular muons, with

16 The software was written by P. Lösel for a large-scale micromegas detector (see [43])

an inclination angle of less than 0.5°. A double Gaussian function is fitted to both distributions and although the effect of the tilting is more drastic for larger angles it can be seen, that the alignment significantly improves the reconstruction. A double Gaussian was chosen since also straggling in the MDTs has to be considered. The width of the narrow Gaussian, which describes the uncertainty of straight tracks, improves from (406±1) µm to (291±4) µm in the aligned case. This value is not the resolution of the GEM-detector, since the width of the distribution is mostly defined by the extrapolation error of the tracks in both MDT chambers[17].

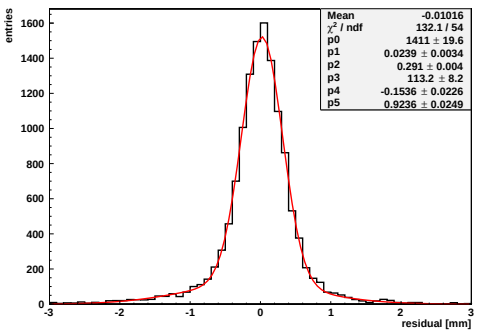


(a) Residuum between measured position in GEM-detector and by MDT-chambers predicted position for perpendicular incident of muons after position and angular alignment

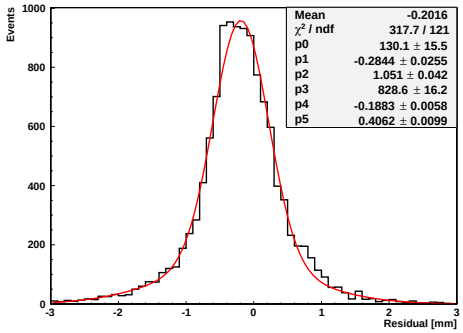


(b) Residuum between measured position in GEM-detector and by MDT-chambers predicted position for perpendicular incident of muons after position alignment, but before angular alignment

Figure 7.5: Comparison of cluster position deviation between MDT-prediction and position in the GEM-detector for perpendicular muons before and after alignment

### 7.2.2 Validation of the µTPC-angle reconstruction

The thickness of the drift space was set to 10 mm and the particle density[18] inside the detector was (3.33±0.02)mbar $K^{-1}$. The electric fields applied were: $E_{Ind}$=$E_{Trans1}$=$E_{Trans2}$=2000 V $cm^{-1}$, $E_{Drift}$=700 V $cm^{-1}$, $\Delta GEM_1$=300 V, $\Delta GEM_2$=270 V and $\Delta GEM_3$=360 V and a aluminum coated Kapton-cathode was used.

In figure 7.6(a) and 7.6(c) the reconstructed angles for both fitting methods are plotted against the MDT reference angle. The quality of the reconstruction has been determined by Gaussian fits to the distribution of the reconstructed angle in steps of a degree of the reference angle (see figure 7.7). Mean value and standard deviation were calculated and also the share of the angles reconstructed in a one $\sigma$-band around the mean value in comparison to all reconstructed angles, for the specified angular

17 For measurements with a large scale Micromegas detector, with a better resolution than 100 µm, in the same experimental setup similar values for the width of this distribution have been measured (see [43])

18 The gas system of the CRF has been used and active pressure regulation was not possible

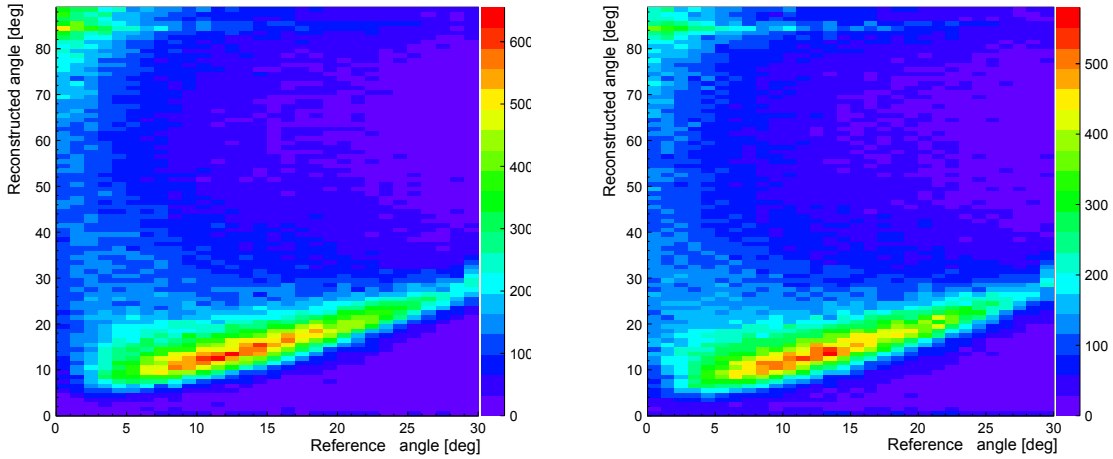


(a) Angle reconstructed with Arctan-fit

(b) Charge corrected reconstructed angle with Arctan-fit

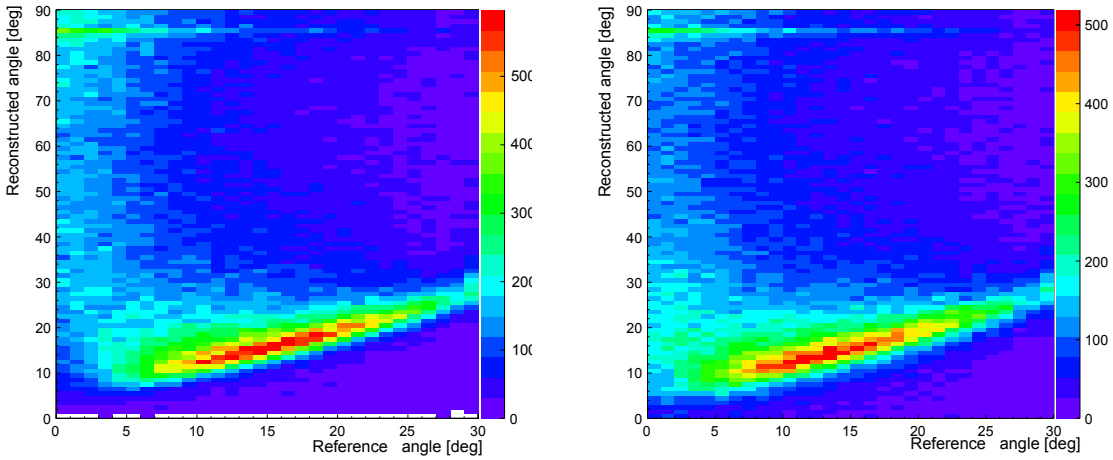


(c) Angle reconstructed with Fermi-fit

(d) Charge corrected reconstructed angle with Fermi-fit

Figure 7.6: Comparison of different fitting methods and charge correction factors

range. Since the reconstruction obviously does not work for angles smaller than 5°, this value was the lower boundary for the analysis.

The mean of the reconstructed angles is shown for both fitting methods in figure 7.7(a). Both methods show best results at angles larger than 20°. Smaller angles are reconstructed systematically too large, although the Arctan method works slightly better here. The deviation from the expected value is shown in figure 7.8(a) for the Arctan-fit. The deviation shows a nearly linear behavior, which allows to correct the reconstructed angle.

The width of the distribution of the reconstructed angle is almost constant at 5° in the range between 5° and 30°, as it is shown in 7.9(a).

In order to optimize the reconstruction also for angles in the range from 5° to 20° some corrections were necessary.

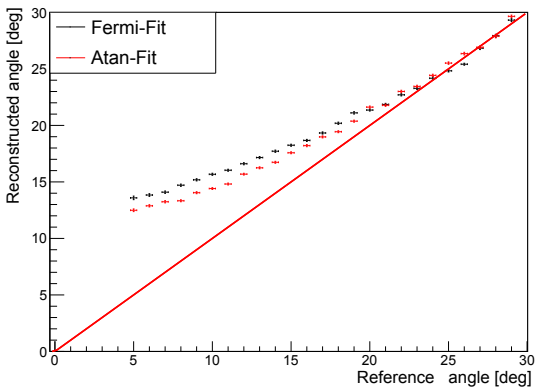


(a) Uncorrected mean reconstructed angle against angle referencd by MDT-chambers

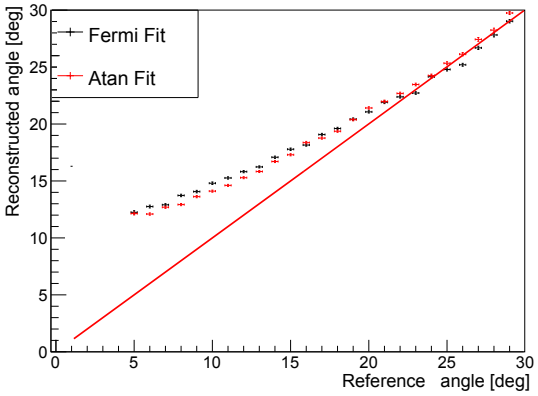


(b) Charge corrected mean reconstructed angle for both fitting methods against reference angle

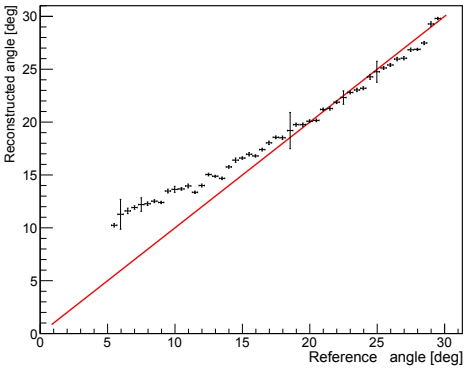


(c) Mean reconstructed angle with cut to difference between both fitting methods, variable binning and charge correction

Figure 7.7: Mean reconstructed angle against reference angle

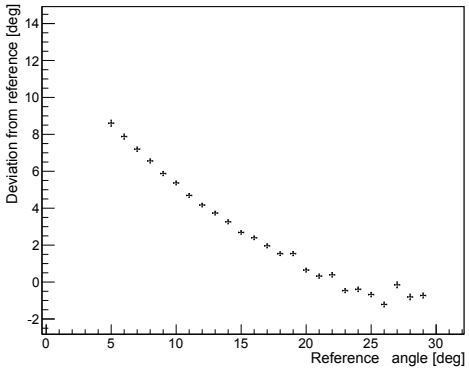


(a) Average deviation of reconstructed angle by the Arctan-method to the reference angle by the MDT-chambers

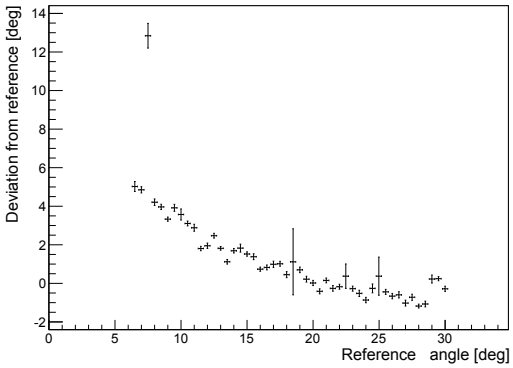


(b) Average deviation of reconstructed angle by Arctan-methode and reference angle. Data was corrected for charge coupling on neighbouring strips and a cut on the difference of the reconstructed angles has been applied

Figure 7.8: Deviation of mean reconstructed angle from reference angle against reference angle

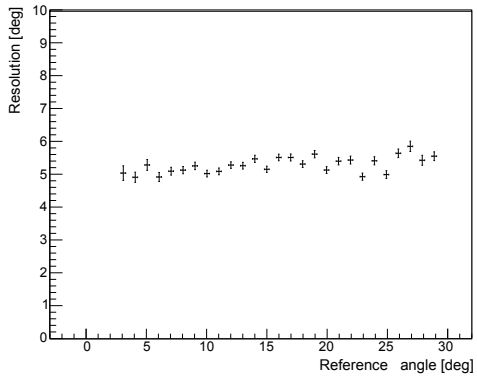


(a) Width of the distribution or the reconstructed angle for the Arctan-method

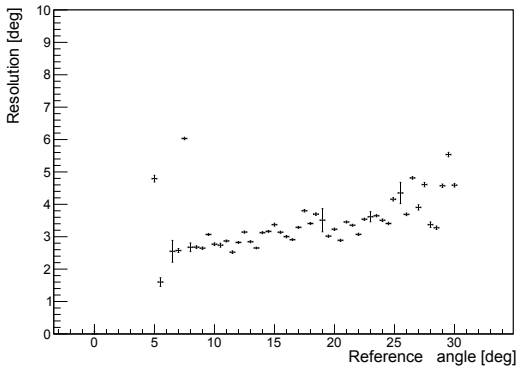


(b) Width of the charge coupling corrected angle distibution for the Arctan-method against the reference angle

Figure 7.9: Mean reconstructed angle against reference angle

As a first step the raw data was corrected for charge coupling of neighbouring strips with a correction factor of 0.2. This led to angular distributions, which are shown in figure 7.6(b) and 7.6(d) for both fitting methods. For the Arctan method there is hardly any visible improvement, but for the Fermi-method there are some slight improvements for smaller angles. This can be seen also in figure 7.7(b) where it is apparent that the Fermi-method now predicts the same mean values for the reconstructed angle as the Arctan-method.

The next step in the analysis was to set a cut on the difference of the reconstructed angle with both fitting methods. Only events where the difference between both reconstructed angles did not exceed 5° were allowed. Also a cut to the maximum reconstructed angle has been applied, since the μTPC method in principle fails at very large angles (see chapter 4). Therefore all events with a reconstructed angle of more than 75° have been neglected in the further analysis. And finally the bin size was adjusted to the reconstruction method.

This can be understood from the following deliberations.

If the fit of the slope can be conducted with an symmetric error $\sigma$, the distribution of the reconstructed slope $\mu$ for a fixed true slope can be written as:

$$s(x) = N_0 e^{-\frac{1}{2}\left(\frac{x-\mu}{\sigma}\right)^2} \tag{7.4}$$

If now the angle is reconstructed the distribution of the angle looks as follows:

$$f(\theta) = N_0 e^{\frac{1}{2}\left(-\frac{\frac{1}{\tan\theta}-\mu}{\sigma}\right)^2} \tag{7.5}$$

Leading to a most probable value for $\theta$ of :

$$\bar{\theta} = \frac{1}{\tan\mu} \tag{7.6}$$

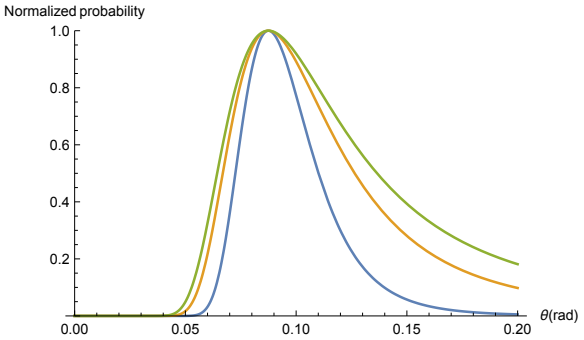


(a) Example of functional of distibution of reconstructed angle for 5° and different errors for the reconstructed slope

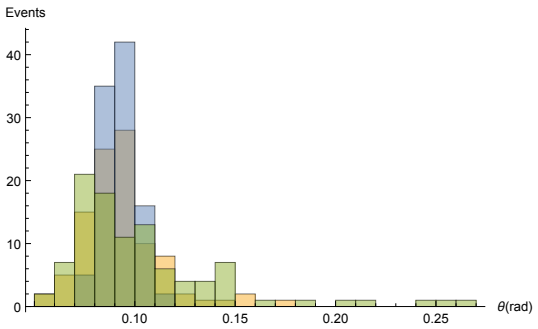


(b) Sampled and binned distribution of reconstructed angle for the functions above

Figure 7.10: Effect of binning on mean value of reconstructed angle

As it can be seen in figure 7.10 this distribution is not symmetric any more. If the distribution of the slope is now sampled and the angle is calculated and filled in a histogram this can lead to a misinterpretation of the most probable value. This can be seen in figure 7.10(b), where the reconstructed angle for distributions of the slope with the same mean value, but different standard deviations are plotted.

Therefore the bin width has to be adapted to constant steps in the slope $\Delta x$, leading to steps in the reconstructed angle of:

$$\Delta\theta_i = \arctan\left(\frac{a}{x + i \cdot \Delta x}\right) - \arctan\left(\frac{a}{x + (i-1) \cdot \Delta x}\right) \tag{7.7}$$

The result of this operations is shown in figure 7.11. Although the contrast of the colour plot is not as good as in the equally binned histograms the effect on the mean value is apparent, which is plotted in figure 7.7(c). The deviation of the mean reconstructed and reference angle is now in the range from 11° to 30° below 2° (see figure 7.8(b)). This is a major improvement compared to the uncorrected results, where this could only be achieved for angles larger than 17° (see figure 7.8(a)). Also the width of the resolution drastically decreases to values from 2° to 4° as it is shown in figure 7.9(b).

Another criterion for the quality of the reconstruction would be the fraction of events with a reconstructed angle within a one-$\sigma$-band of the mean value, compared to all reconstructed angles. For the totally uncorrected case this ratio did not exceed (45±2)% for any angle, as it can be seen in figure 7.12. This means, that even in the best case 55% of the reconstructed angles were wrong. In the corrected case this ratio constantly increases with the reference angle having a maximum value of (80±3)% at 30° and exceeding the maximum for the uncorrected case already at 12°.

Altogether this shows, that a reconstruction of the tracks for muons is possible with reasonable accuracy and efficiency. The results are also in agreement with the simulations in section 4.1.2, where it has been shown, that the reconstruction of

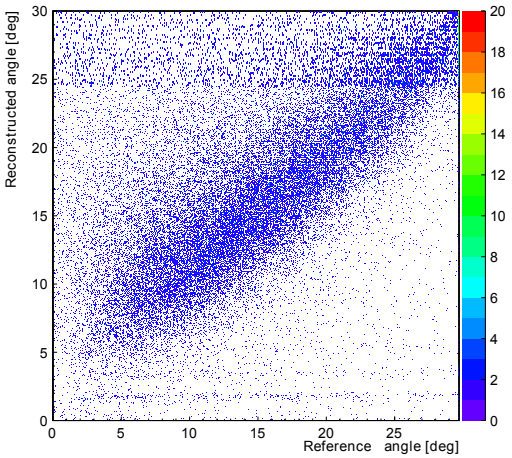


Figure 7.11: Reconstructed angle against reference angle by MDT chambers with charge correction and variable binning

angles smaller than 10° is hardly possible. Although the timing and space resolution for this measurement are far worse than in the simulation assumed. Most likely due to the long tracks of the muons in the detector this disadvantage of the readout is compensated.

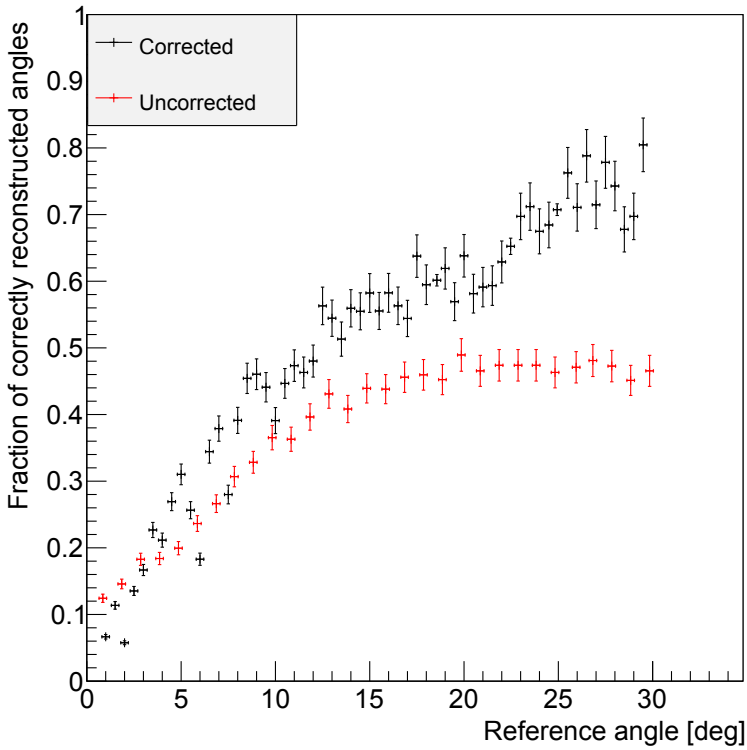


Figure 7.12: Comparisons of the ratio of correctly reconstructed angles, evaluating figure 7.11, to all reconstructed angles in the corrected and uncorrected case

# 8 Photon detection efficiency

Gas detectors have due to the low particle density in their active volume a comparably low efficiency for photon detection. The photon attenuation of Photoelectric effect and Compton effect are both dependent on the atomic number Z of the medium, where conversion would appear. The gas mixtures used in typical micro structured detectors do not contain any heavy elements, therefore the absorption coefficients are rather low, or in other words the absorption lengths are rather long. For the Photoelectric effect the cross section can be described in Born-Approximation with equation 8.1 (taken from [5]):

$$\sigma_{Ph} = 4\alpha^2\sqrt{2}Z^5\sigma_0\left(\frac{1}{\gamma}\right)^{\frac{7}{2}} \tag{8.1}$$

$$\text{with} \qquad \sigma_0 = \frac{8\pi r_e^2}{3} \tag{8.2}$$

Where $\alpha = 1/137$ is the fine structure constant, $r_e$ is the classical electron radius and $\gamma = h\nu/m_e c^2$,where h is the Planck constant, $\nu$ is the frequency of the incident photon, $m_e$ the rest mass of an electron and c the speed of light. The angular dependent cross-section for Compton-scattering for a single electron is given by the well known Klein-Nishina cross-section, which can be integrated to the total cross-section (see [44]):

$$\sigma_{Compton} = 2\pi r_e^2\left[\frac{1+\gamma}{\gamma^2}\left(\frac{2\,(1+\gamma)}{1+2\gamma} - \frac{1}{\gamma}\ln\left(1+2\gamma\right) + \frac{1}{2\gamma}\ln\left(1+2\gamma\right) - \frac{1+3\gamma}{(1+2\gamma)^2}\right)\right] \tag{8.3}$$

The cross-section per atom is then dependent on the amount of electrons for this atom and therefore proportional to Z.

The absorption itself is then depending on the attenuation coefficient μ, which depends on the absorption cross section and the particle density n.

$$\mu = n\sigma \tag{8.4}$$

The upper limit for the detection efficiency can then be described by the attenuation in a medium of thickness $r_{max}$:

$$\epsilon = \int_0^{r_{max}} \left(1 - e^{-\mu r}\right) \cdot t\,(r)\,dr \tag{8.5}$$

The estimated efficiency depends on two parameters. First the absorption of photons in mater, which leads to photoelectrons that are detected. Secondly those photoelectrons must traverse a specific path length in the active volume to deposit enough energy to be detected. In this calculation this threshold is considered by the function t(r). If the drift length in the detector is significantly larger than the drift space, this factor is everywhere 1, except at the fringes of the drift space. Its exact behavior depends on the energy loss of the electrons, which is dependent on the photon energy.

## 8.1 Increasing the drift space

Altering the geometry of the detector by increasing the thickness of the drift space can improve the detection efficiency in two ways. The thicker the drift space, the more photoelectrons can be produced there, which increases the efficiency nearly linearly. The other effect is that not only more photoelectrons are produced, but they can also create more charge inside the active volume. A photoelectron of 35 keV for example has a CSDA-range[19] of 17 mm in the detector gas at standard conditions (see [45]). Therefore photoelectrons, which were produced at the borders of the drift volume, will not deposit enough energy to trigger the readout electronics and cannot be detected.

The relative detection efficiency was examined with photon sources, which were placed atop the detector with a 25 mm spacer and the width of the drift gap was varied from 2 to 10 mm. The relative efficiency was determined by counting triggers from the lowest GEM-foil with an NIM-counter over a fixed time of 10000 s. This has been done, because much higher count rates could be measured than by using the standard readout. Amplification and trigger threshold were equal for all measurements. The electric fields were $E_{Ind}$ = $E_{Trans1}$ = $E_{Trans2}$= 2000 V cm$^{-1}$ , $\Delta U_{GEM1}$=300 V , $\Delta U_{GEM1}$=270 V and $\Delta U_{GEM1}$=270 V.

In figure 8.1 the increase of detected photons with increasing drift space is shown for an aluminum cathode and different photon energies. The behavior in all cases is as expected nearly linear, since the attenuation coefficients are quite low and the attenuation therefore can be approximated with:

$$I_r = 1 - (1 - \mu \cdot x) \tag{8.6}$$

Where x is the thickness of the drift space. Figure 8.1(b) shows a simulation for the same experimental set-up with an aluminum cathode. In the simulation a detection threshold of 1.5 keV inside the drift volume was chosen. The simulation also predicts absolute values for the conversion efficiency of 8±1% for the best value at 10 mm drift space.

The inclination of a line fit to measurement and simulation match within their error limits being 0.105±0.002 mm$^{-1}$ for the measurement and 0.098±0.005mm$^{-1}$ for the simulations. The intercept in both cases should account for the electrons produced

19 Continous-Slowing-Down-Approximation

in the cathode. In the measurement for the $^{55}$Fe-source this value is negative, which presumably indicates a underestimation for low energy deposition, since this is not apparent for the other two sources this feature is most likely due to a too low threshold chosen in the measurements.

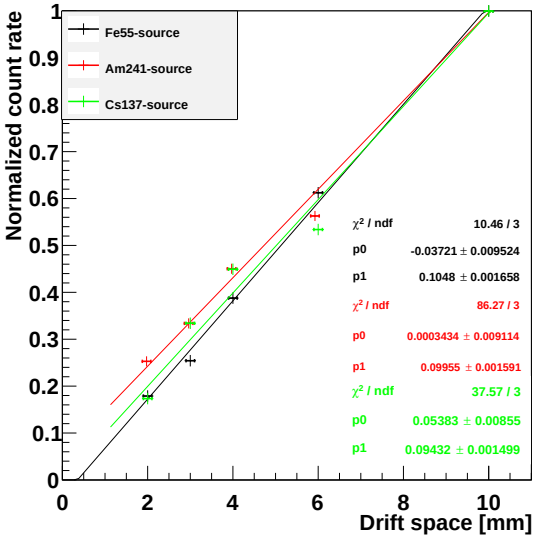


(a) Measured normalized efficiencies for different photon energies with respect to variation of the thickness of the driftspace

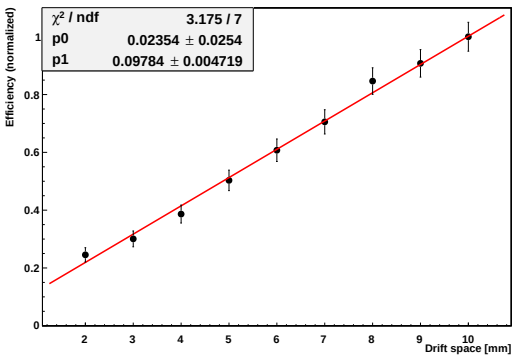


(b) Simulated normalized efficiency for a $^{55}$Fe source and a 100 nm aluminum coated Kapton-cathode for a minimal energy deposit of 1.5 keV inside the drift volume

Figure 8.1: Efficiency increase due to variation of drift space

## 8.2 Conversion in photo cathodes

As shown in equation 8.1 the cross section for the Photoelectric effect is strongly dependent on the atomic number of the conversion material. Besides using a different gas with higher atomic number like Xenon, there is still the possibility of using a solid converter layer inside the detector. Not only the cross section will be improved by a solid converter, but also the density and therefore the attenuation factor will increase. Additionally the solid converter defines a position in Z-direction where the conversion took place, which is helpful for tracking purposes.

In principle it is possible to use the GEM foils itself as a converter, as it is done for example for neutrons (coated with Boron, see [46] ) or soft X-ray (coated with Gold, see [47]). The idea behind this method is to stack a couple of coated GEMs and apply a voltage to them, that will only transport the created electrons through these foils. Only in the last stage is a high enough electric field to multiply the electrons. In theory very high efficiencies could be achieved by this method. On the other hand the spatial resolution suffers from the stacking and tracking will be quite complicated, since it would be necessary to know in which GEM foil a conversion has taken place.

The method used here was to utilize different single converter cathodes to improve the detection efficiency.

Figure 8.2 shows simulated detection efficiencies for the example of a $^{133}$Ba source and cathodes made of silver, gold, iron and lead. As expected from equation 8.1 the detection efficiency becomes higher for elements with higher atomic number. Also the thickness of the conversion layer is quite important. At 100 nm all tested cathodes have, within their respective error bars, equal conversion efficiency. The separation becomes more distinctive for thicker layers. The gold and lead cathodes perform very similar with an optimal value of $(0.35\pm0.3)\%$ at 3 µm thickness. For tracking purposes and in order to get the most information from the tracks of the photoelectrons it is on the other hand favourable to have a conversion layer as thin as possible. Photoelectrons have only a very limited range in the solid medium, which can be seen in the efficiency simulation. The efficiency starts to saturate at a thickness of about 1.5 µm, therefore electrons produced at the top of the layer are stopped inside and cannot be extracted.

To test the predicted increase in efficiency cathodes of heavier elements have been tested in comparison to the standard 100 nm aluminized Kapton-foil. In order to determine their conversion qualities a $^{55}$Fe-source and a $^{133}$Ba-source have been placed atop of the detector on the collimator described in chapter 6. Here the signals could be recorded, since the count rate in this set-up was lower than 100 Hz. Otherwise the same electric fields as in section 8.1 were used and the width of the drift space was set to 6 mm.

The first cathode to be tested was a stainless-steel mesh with 23 µm wires, as it is used in Micromegas detectors. Additionally a standard GEM-foil was used as cathode. The same voltage was applied to both sides, therefore no amplification could happen inside the foil, leaving it as an effective 5 $\mu$m copper coated Kapton-cathode. As a fourth cathode a standard aluminized Kapton-cathode has been coated with 466 nm

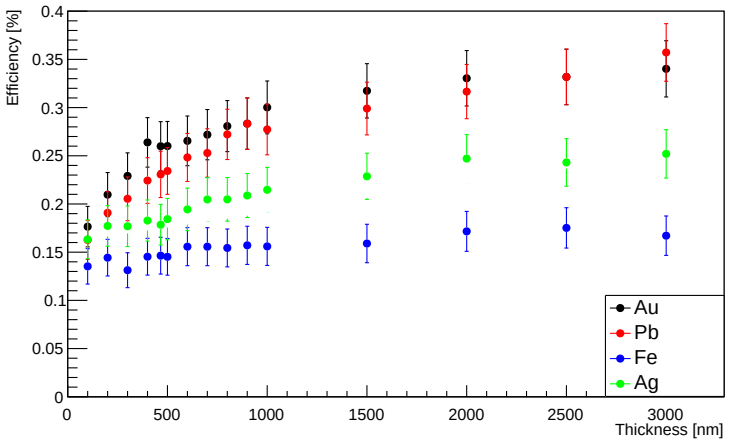


Figure 8.2: Simulated detection efficiencies for photons from a $^{133}$Ba source and different thicknesses of conversion coating. Drift space of 6 mm and detection threshold of 1.5 keV.

of gold by the target laboratory of LMU. The thickness of the gold layer was estimated to be a proper trade-off in efficiency and electron range.

Table 8.1: Relative efficiencies for different cathodes and various photon energies, normalized to the overall worst performing cathode, for 6 mm drift space and a cut to minimal energy deposition of 1.5 keV (overall simulated efficiency)

| | Measurement | | Simulation | |
|---|---|---|---|---|
| | $^{55}$Fe | $^{133}$Ba | $^{55}$Fe | $^{133}$Ba |
| Aluminum-Kapton | 1 | 1 | 1 (4.4%) | 1 (0.42%) |
| Copper-Kapton | 0.9±0.2 | 1.4±0.2 | 0.88 | 1.41 |
| Steel-Mesh | 2.4±0.2 | 1.2±0.2 | 1.8 | 1.25 |
| Gold-Kapton | 0.9±0.2 | 2.2±0.2 | 0.6 | 2.19 |

For most combinations of cathodes and photon energies simulation and measurement match in their respective error range. This shows that the most photon transparent cathode has the best efficiency for photons of 6 keV. Most conversion for this photon energy is happening in the gaseous volume. For 35 keV photons the most effective conversion layer was, as expected, the gold-coated cathode with a relative efficiency of a factor (2.2±0.2) compared to the standard aluminum-cathode. The simulated efficiency increases from (0.42±0.01)% to (0.93±0.01)%[20]. The use of a suitable converter cathode can improve the detection efficiency by at least a factor of two for photons at energies of 35 keV.

20 Only the photons with 35 keV from the $^{133}$Ba source are considered

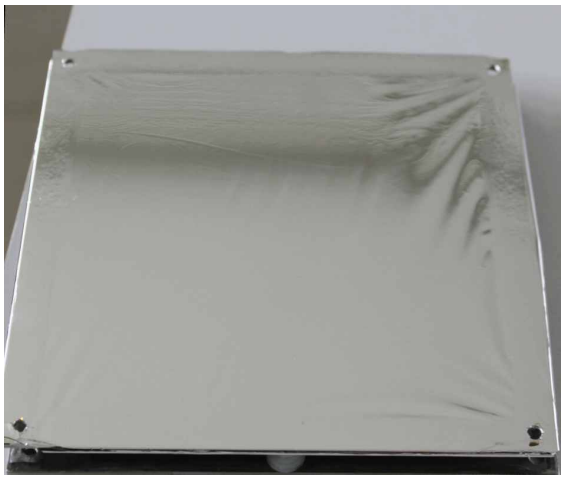

(a) Cathode of 10 $\mu$m Kapton coated with 100 nm aluminum

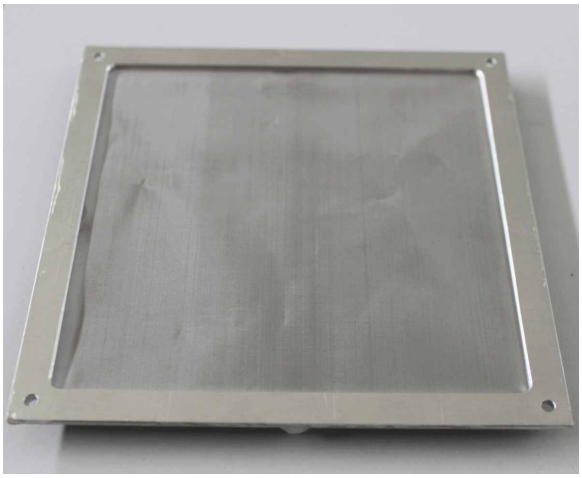

(b) Stainless-Steel mesh made from 18 $\mu$m wires

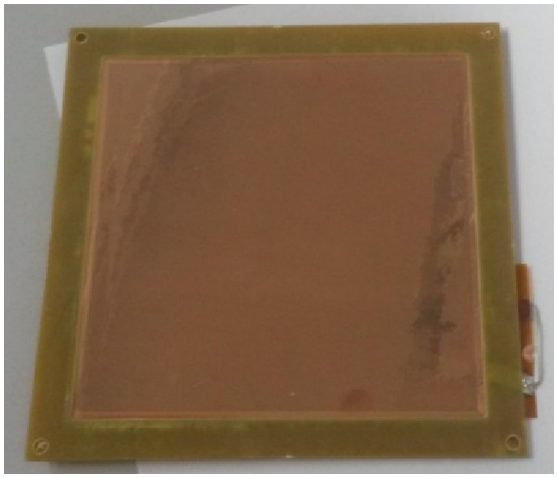

(c) GEM-foil used as cathode, with effective 5 $\mu$m of copper plating

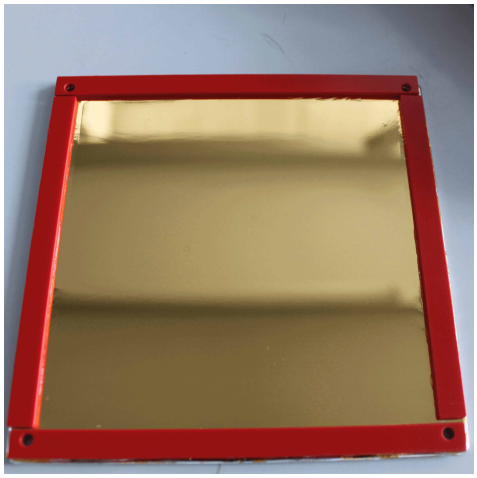

(d) 10 $\mu$m Kapton-cathode coated with 466 nm of gold

Figure 8.3: Four different types of cathodes for determination of the conversion efficiency of photons

# 9 Detection of thermal neutrons

Since neutrons, because of the absence of an electric charge, can only interact with the nuclei of atoms, they provide a great source for non destructive probing and imaging. Compared to photons, which do mostly interact with the electron shell of an atom, the interaction of neutrons is hardly depending on the atomic number. The possible interactions can be separated in two main sections: Scattering and absorption. A neutron can scatter at the nucleus of an atom. In this process it can lose energy and momentum and will transfer this to the atom. In addition to recoil the atom can get excited by this process and release radiation. If the nucleus absorbs the neutron, this can lead to a wide range of nuclear reactions e.g (n,$\gamma$), (n,$\alpha$), (n,2n), or fission.

Imaging with neutrons can be roughly separated in the two divisions of applications, which either use the scattering of neutrons on lattices or the attenuation in matter. The interference of the matter wave with a lattice structure leads to coherent scattering. This interference pattern represents the Fourier-transform of the lattice in so called reciprocal space. Therefore the lattice structure can be reconstructed from the interference pattern.

The absorption of neutrons can be utilized to get radiographic or tomographic images. Whether scattering or absorbtion are dominating is dependent on the target nucleus and the energy of the neutron. Depending on their energy neutrons are categorized as in table 9.1.

Table 9.1: Neutron classification by energy and de-Broglie wavelength ( [48])

| Type | Energy | Wavelength |
|---|---|---|
| ultra cold neutrons (UCN) | <0.2 meV | >2 nm |
| cold neutrons | <2 meV | 2000-640 pm |
| thermal neutrons | <100 meV | 640-90 pm |
| epi thermal neutrons | <1 eV | 90-28 pm |
| fast neutrons | < 20 MeV | |
| relativistic neutrons | > 20 MeV | |

The following chapter is dedicated to the detection of thermal neutrons with a modified GEM-detector. The high rate capability and the relative low detection efficiency for high energy photons combined with a high spatial resolution make GEM-based detectors promising replacement candidates for current detector systems.

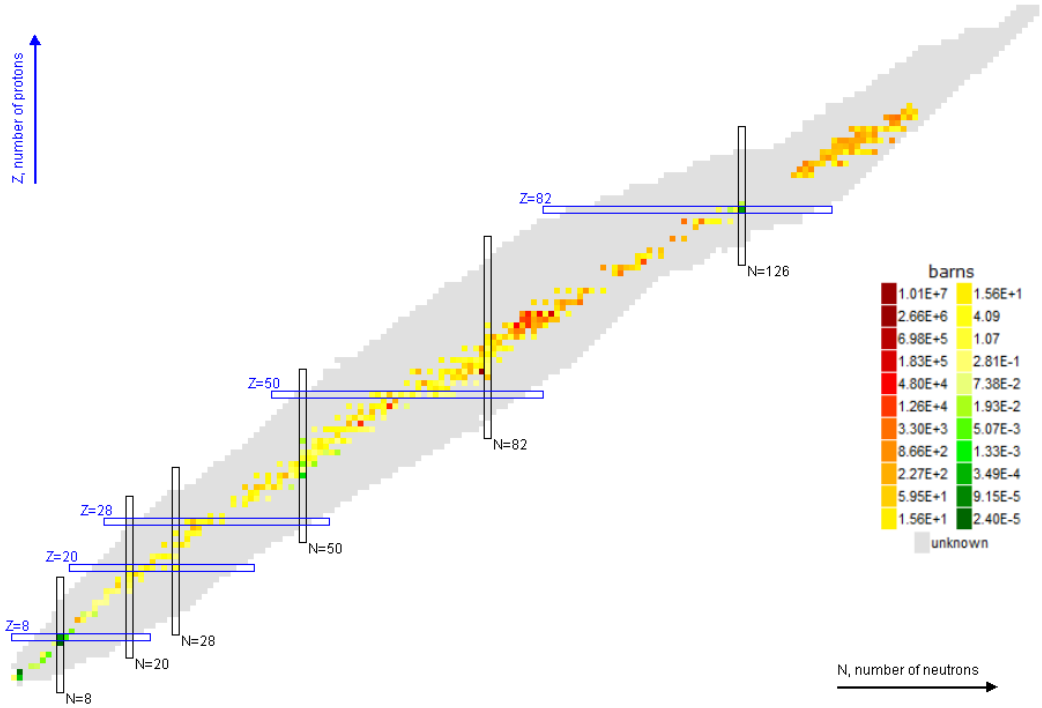


Figure 9.1: Chart of nuclides with neutron capture cross sections for thermal neutrons ( [49])

## 9.1 Detection of thermal neutrons

Thermal neutrons are typically detected by the induced radiation in an absorption process. Again there are two main types of neutron detectors: gas based and solid state based detectors. Scintillators (doped with Li and Ce) and image plates are the most common types for solid state detectors. Both suffer from their low or non-existent time resolution. Scintillators in addition are not capable of high rate detection and single neutron detection is not possible with imaging plates.

Gas detectors can detect neutrons, if they are properly prepared to do so. Since neutrons do not ionize directly in the gaseous volume, an element with a high absorption cross section has to be added. Common converters are $^{3}$He, $^{6}$Li or $^{10}$B.

Two examples of possible reactions are:

$$^{3}He + n \rightarrow p + t + 0.764\ \text{MeV} \tag{9.1}$$

$$^{10}B + n \rightarrow \alpha + ^{7}Li + 2.8\ \text{MeV} \tag{9.2}$$

Helium can be directly used as an inert gas in a detector and is in fact the most common detector gas for neutron applications. It is typically mixed with quenching gases like $CO_2$ or $CF_4$.$^{3}$He can be found in natural gas, but since this isotope is very rare on earth almost all $^{3}$He is produced industrially. The prices for $^{3}$He in the last years increased by a factor of approximately 20, therefore alternatives are strongly investigated (see [50]). One possible candidate is $^{10}$B, which can be used like $^{3}$He in

gaseous detectors, where $BF_3$ is typically used. The properties of the absorption reactions for both gases are shown in table 9.2. $BF_3$ however is highly toxic and corrosive and therefore not easily usable in a GEM-detector.

Alternatively as a thin coating boron can be used inside a gaseous detector. For reasons of momentum conservation the fission products will be emitted back-to-back. Therefore only one of the particles can be detected and only its fraction of the total energy, which is a slight methodical disadvantage.

Table 9.2: Properties of neutron converters used in gaseous detectors for 25 meV neutrons (taken from [51] and [48])

| Converter | Reaction | Cross Section [barn] | Product Energies[21] [keV] |
|---|---|---|---|
| $^3$He | $^3$He(n,p)t | 5330±10 | 573(p),191(t) |
| $^{10}$B | $^{10}$B(n,$\alpha$)$^7$Li | 3836 | (6%) 1730($\alpha$),990(Li) or (94%) 1472($\alpha$),840(Li), 480($\gamma$) |

## 9.2 Measurements with a $^{252}$Cf-source at FRMII

Neutrons are produced in some radioactive decays, by spallation or by interaction of high energy alpha-particles with a material with high cross section for an ($\alpha$,n) reaction. Since no suitable thermal neutron source was available, a setup, based on a $^{252}$Cf source, could be used at the "Forschungs-Neutronenquelle Heinz Maier-Leibnitz" (FRMII) before restart of the reactor. Afterwards a better defined neutron beam was available.

### 9.2.1 The thermal neutron source

The $^{252}$Cf based thermal neutron source at FRMII is moderated with layers of polyethylene and shielded with layers of iron, lead and boron carbide (see [52]). Besides an alpha decay $^{252}$Cf can also undergo spontaneous fission in 3.1 % of all decays (see [23]). In this process an average of 3.5 neutrons is produced (see [48]) with an energy range from 0 to 13 MeV and a peak in the distribution at 1 MeV (see [48] and figure 9.2(a)). The source is moderated by proton-rich material to provide mostly cold and thermal neutrons, as it can be seen in figure 9.2(b) and 9.2(b).

### 9.2.2 Converter cathodes

A Boron cathode based on a coating of 0.3 µm natural $B_4C$ was first used as a converter cathode, which was produced at the LMU target lab. The detection efficiency was quite poor since only about 20 % of natural Boron atoms are $^{10}$B and the thickness of the coating was too thin. This can be seen in figure 9.3 where the conversion efficiencies for single $^{10}$B -layers were simulated. The simulations show, that the

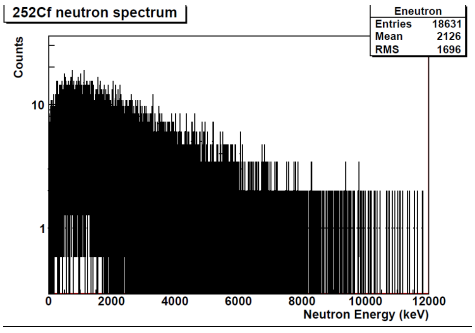


(a) Unmoderated neutron spectrum

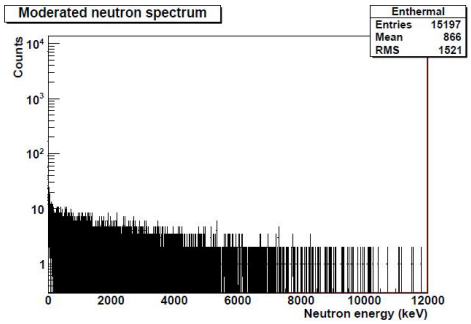


(b) Entire moderated neutron spectrum

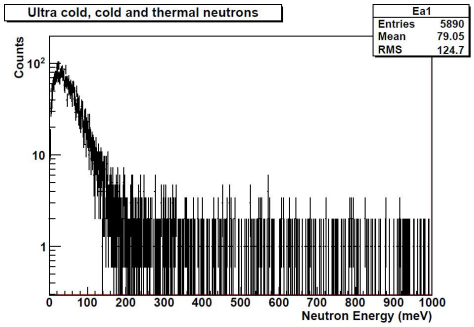


(c) Cold and thermal neutron spectrum

Figure 9.2: Spectrum of a $^{252}$Cf source before and after moderation (taken from [52])

conversion efficiency is dependent on the thickness of the conversion layer with an optimal value of 3 µm for a single layer and neutron energies of 10 meV. Thicker conversion layers do not improve the efficiency further since the range of the trackable products in the conversion layer is just around this value (3.14 µm for the $\alpha$-particle and 1.53 µm for the $^{7}$Li-ion, taken from [53]). Boron-cathodes made from pure $^{10}$B and optimized thickness, which were initially build for usage in a strip chamber from the detector-group at FRMII, could be used to improve the detection efficiency (described in [54]).

One crucial aspect in neutron detection is the distinction of neutrons and photons in the detector. Photons are produced by the thermalization of the neutrons and also by activation of the target material. Additionally photons of 480 keV are produced in 94 % of the neutron capture reactions in Boron (see table 9.2). In figure 9.4 the simulated energy deposition in the drift volume is shown for different conversion layers and 10 meV neutrons. For thin conversion layers the reaction products Li and He are clearly distinguishable by their respective different energy loss in the detector. In the case of a 0.3 $\mu$m Boron coating these two peaks are clearly separated as it can be seen in 9.4(a). The thicker the cathode gets the worse this separation becomes. For every thickness of conversion layers the signals around channel 0 correspond to charge deposition by photons in the detector. Therefore a simple cut on the collected charge will be sufficient to get rid of background due to photons.

Since the energy deposition per event in the active volume is about 1 MeV the amplification fields could be lowered to achieve the same amount of charge at the readout side. The fields used were : $E_{Ind} = 3000\,V\,cm^{-1}$ , $E_{Trans1} = E_{Trans2} =$

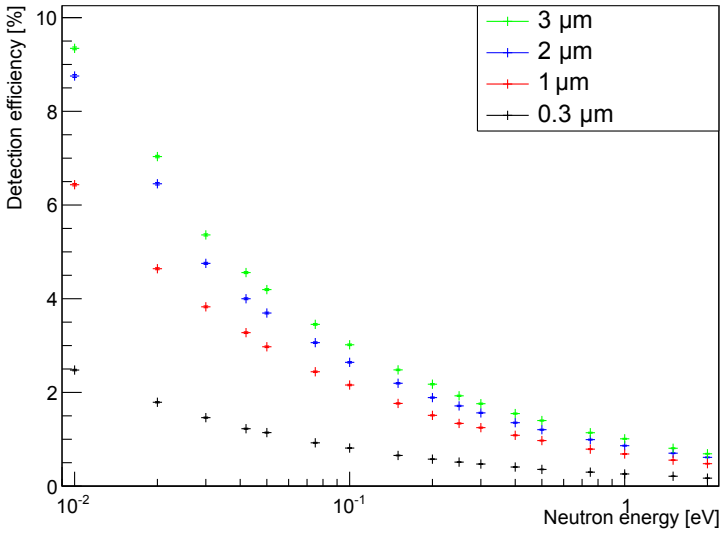


Figure 9.3: Simulated detection efficiencies for converter cathodes with different thickness of $^{10}$B coating

2500 V cm$^{-1}$ , $\Delta U_{GEM1}$=300 V , $\Delta U_{GEM1}$=200 V and $\Delta U_{GEM1}$=215 V and $E_{Drift}$ was varied in the range from 100-1000V cm$^{-1}$ .

Figure 9.5 shows in good agreement with the simulations in figure 4.16 the measured charge in the detector for different conversion layers. Figures 9.5(a) and 9.5(c) represent the pulse height measurement at the anode with APV25 electronics, whereas 9.5(b) and 9.5(d) are measured with a multi channel analyzer (MCA) at the lower side of the last GEM-foil and longer shaping of 60 ns. The measurements at the GEM-foil seem to fit better to the expected charge distribution, which is most likely due to the longer shaping compared to the shaping time of about 50 ns of the APV25 chips (see [17]). Since the discriminator threshold for the measurement with the MCA was chosen independently of the trigger, more of the photon background and electronic noise has been recorded, which is not visible in records of the readout strips. This is a strong argument that mostly charged products have been tracked.

### 9.2.3 Tracking of the products

In order to optimize the spatial resolution the neutron capture products should be tracked in the active volume to enable reconstruction of their starting position in the cathode and therefore the interaction point of the neutron. For a recorded event there is almost always a single track in the detector, as it can be seen in figure 9.6. This suggests that in fact there is only one particle tracked per event and photon background from the conversion can be neglected.

The distinction of the different reaction products might be useful in order to optimize the spatial resolution. For thin cathodes this distinction can be achieved by the charge, which is created in the detector, as can be seen for a 0.3 µm cathode of $B_4C$

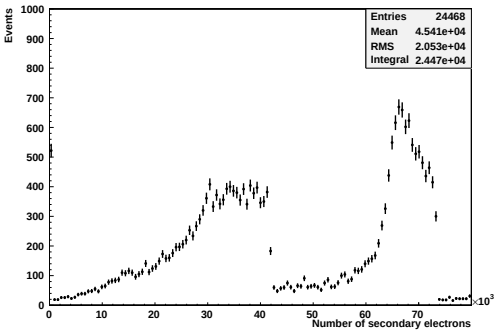


(a) Simulated amount of produced secondary electrons per detected neutron in the drift volume for 0.3 $\mu$m $^{10}$B coating of cathode

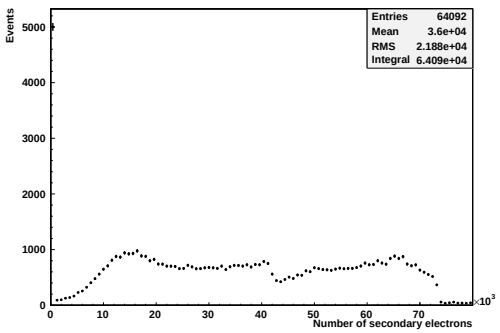


(b) Simulated amount of produced secondary electrons per detected neutron in the drift volume for 1 $\mu$m $^{10}$B coating of cathode

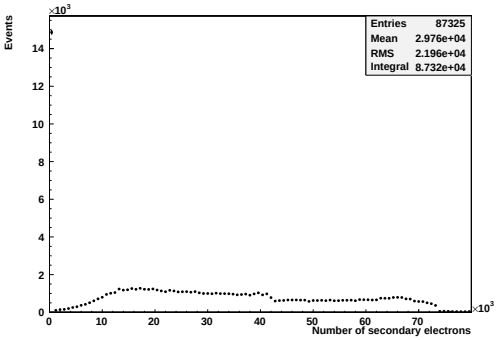


(c) Simulated amount of produced secondary electrons per detected neutron in the drift volume for 2 $\mu$m $^{10}$B coating of cathode

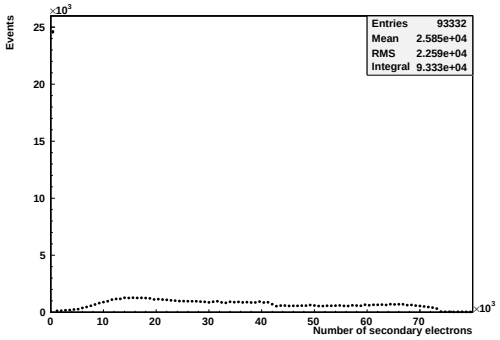


(d) Simulated amount of produced secondary electrons per detected neutron in the drift volume for 3 $\mu$m $^{10}$B coating of cathode

Figure 9.4: Simulated charge deposition caused by neutrons in active Volume for different converter cathodes. The Spikes at very low energies are due to photons

in figure 9.7. The peaks for both ions are clearly separated and the discrimination can be done by the amount of charge collected. For thicker conversion layers this distinction becomes more difficult since the distributions of both particles combine to a single plateau. The discrimination works still, if also the track length is taken into account. The energy loss and the track length of alpha particles and Lithium ions is very characteristic as it can be seen in figure 9.8. This characteristic can be used to optimize the position resolution depending on the tracked particle by measuring the specific energy loss.

The idea of the improvement is shown in figure 9.9. The neutron is converted in the boron-layer and an ion is detected in the gaseous volume. The inclination and the center of charge can be calculated. The position of the conversion can then be calculated by following the track. This method requires the correction factor $\epsilon$ form chapter 4, which compensates the spread of the electron cloud and possible asymmetries of the charge cluster at the readout-plane. This factor is angle dependent (as has been shown in chapter 4), but most likely also different for the two different ions. Therefore it is most useful to be capable of discriminating both products of the neutron capture reaction.

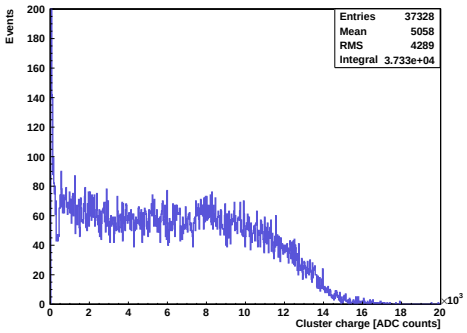


(a) Charge distibution at readout for 1 $\mu$m $^{10}$B-coating recorded with APV25. The peak at very low charges is due to electronic noise in the trigger system

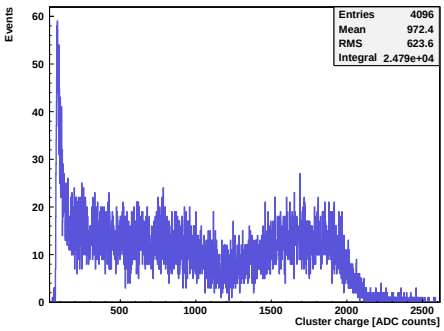


(b) Charge distibution at lowest GEM-foil measured with MCA for 1 $\mu$m $^{10}$B-coating

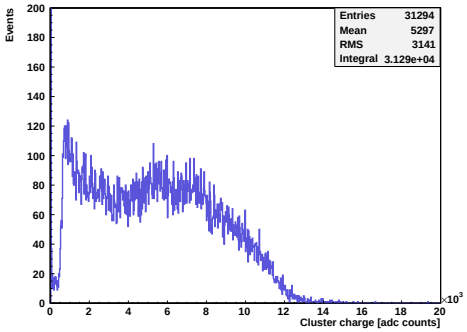


(c) Charge distibution at readout for 2 $\mu$m $^{10}$B-coating

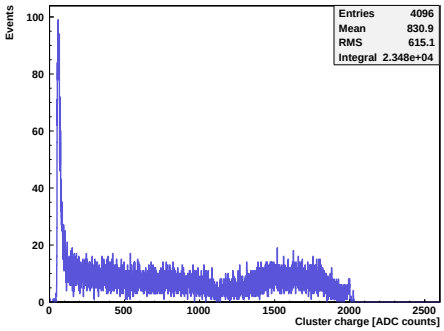


(d) Charge distibution at lowest GEM-foil measured with MCA for 2 $\mu$m $^{10}$B-coating recorded with APV25

Figure 9.5: Measured charge distribution for irradiation of $^{10}$B-coated cathodes

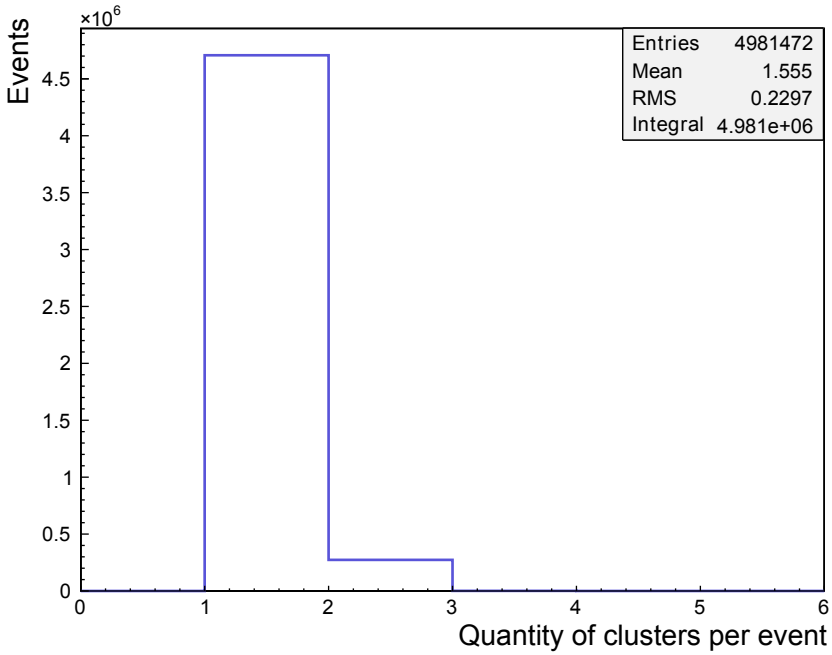


Figure 9.6: Number of tracks for every recorded event for irradiation of a 1 $\mu$m $^{10}$B coated cathode

### 9.2.4 Angle reconstruction of charged tracks

The angular distribution for the neutron capture products should be uniform in all directions. In contrast to this, the reconstruction of the angles for standard electric drift fields, showed a large deficit for angles below 50 degrees, as it can be seen in figure 9.10. The field 665 V cm$^{-1}$ corresponds to a standard value for muons. Besides the track length, the time resolution is the most limiting factor in the determination of the inclination angle (see chapter 4). For a track of 5 mm length at 40° inclination angle and a drift velocity of 50 µm ns$^{-1}$the time difference from the first to the last electron arriving at the readout plane would only be 77 ns but at 20 µm ns$^{-1}$ already 192 ns. This increase would presumably improve the reconstruction by minimizing the relative error on the fit to the slope of the hit distribution at the single strips. This should tend to improve the results for larger angles, but also for smaller angles. The drift velocity of the secondary electrons in the detector can be easily tuned by applying a different drift field (see figure 4.11). Experimentally the drift field was varied leaving all other fields constant. As it can be seen in figure 9.10, the minimal reconstructed angle is strongly dependent on the drift field value and therefore of the drift velocity. Lowering the drift velocity improves the reconstruction at low angles by far. To quantify this improvement the value of the angle at which the distribution is higher than 20% of the distribution at the most probable value has been evaluated for different drift fields. The results are shown in figure 9.11. By lowering the drift velocity the limit of the angular reconstruction could be improved from (38±1)° to (15±1)°.

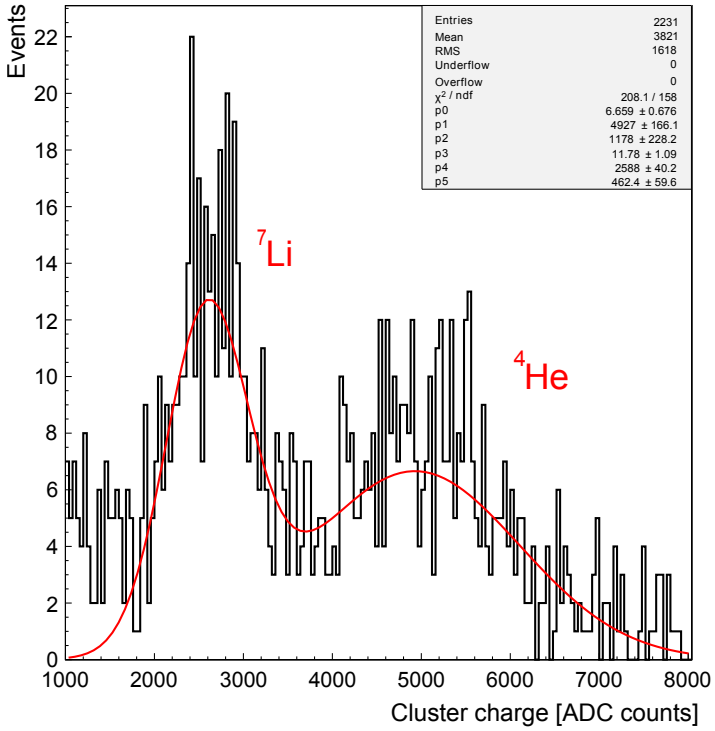


Figure 9.7: Energy deposition of thermal neutrons in the GEM-Detector with a $^{nat}B_4C$ cathode of 0.3 $\mu$m thickness. The $\alpha$ and $^7$Li peaks are clearly distinguishable

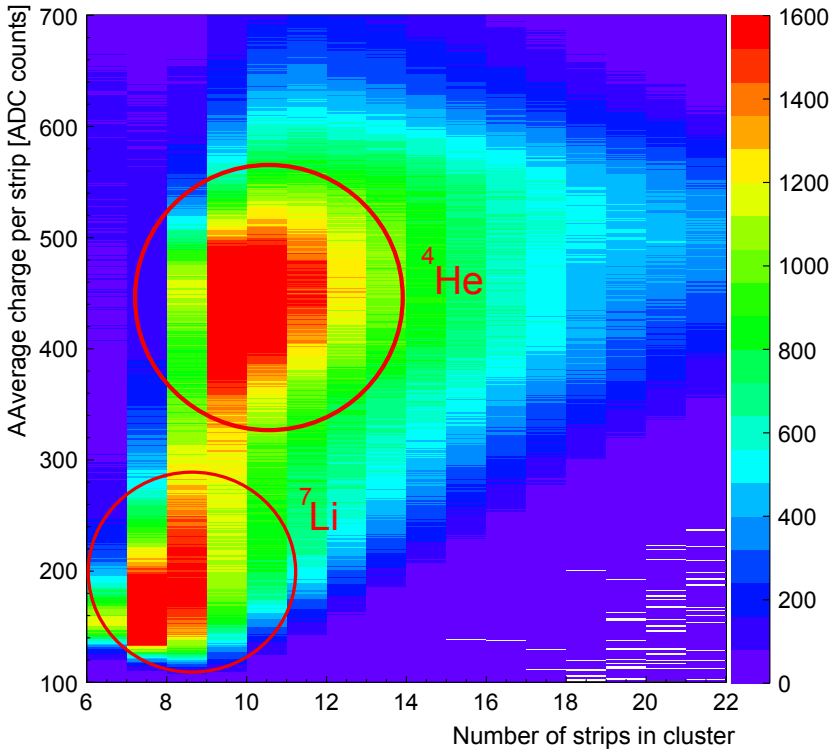


(a) Charge density against track length for measurement with one-dimensional readout for $E_{Drift}$=200 V/cm for 1 $\mu$m $^{10}$B-layer. The separation of $\alpha$ and $^7$Li is clearly possible

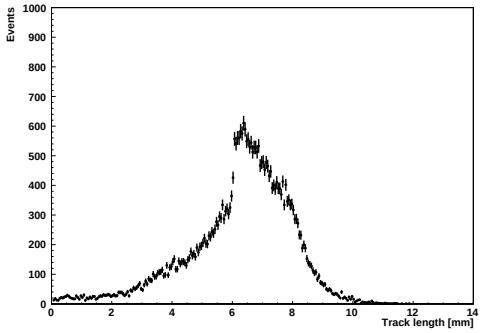


(b) Simulated track length of alpha particle in the drift volume with 1 $\mu$m $^{10}$B-cathode

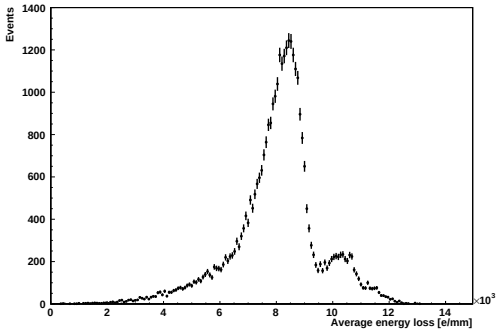


(c) Simulated energyloss per mm in the drift volume for alpha particles with 1 $\mu$m $^{10}$B-cathode

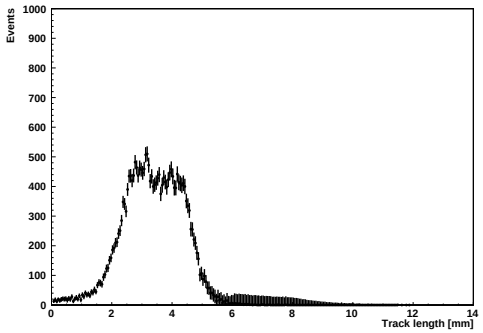


(d) Simulated track length of Lithium ions in the drift volume with 1 $\mu$m $^{10}$B-cathode

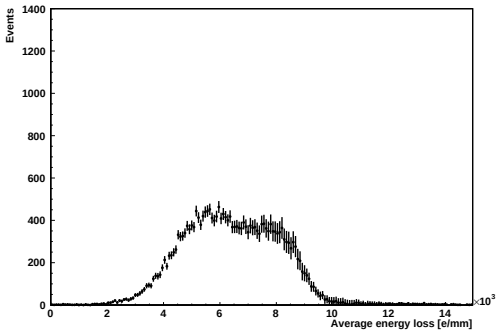


(e) Simulated energyloss per mm in hte drift volume for Lithium ions with 1 $\mu$m $^{10}$B-cathode

Figure 9.8: Distinction of different particles in the detector

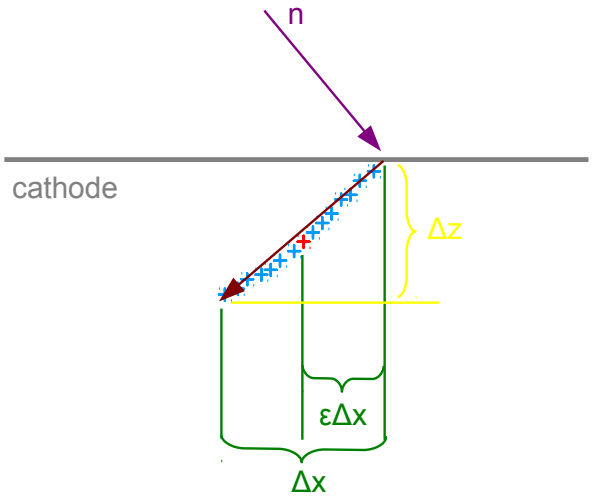


Figure 9.9: Scheme of neutron position resolution improvement by use of the μTPC method

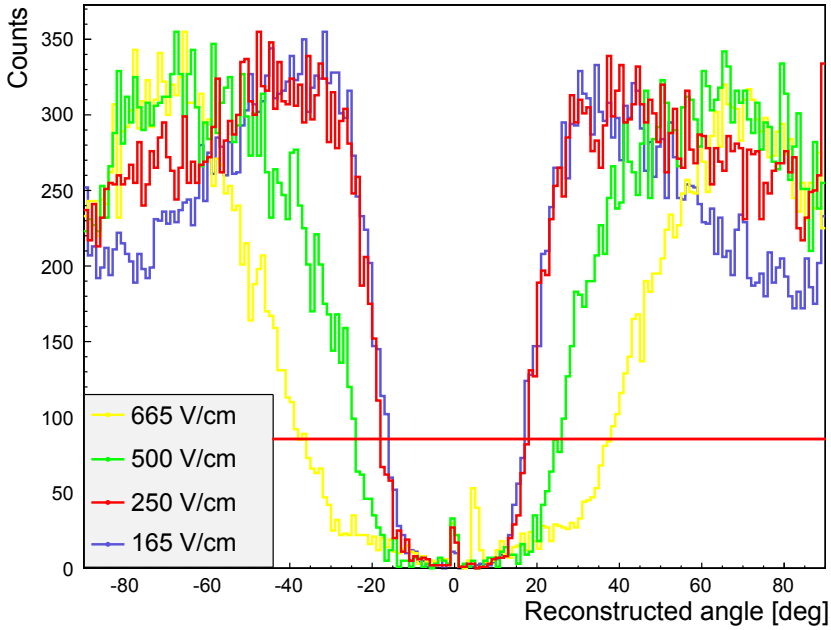


Figure 9.10: Angular distribution for different values of the drift field

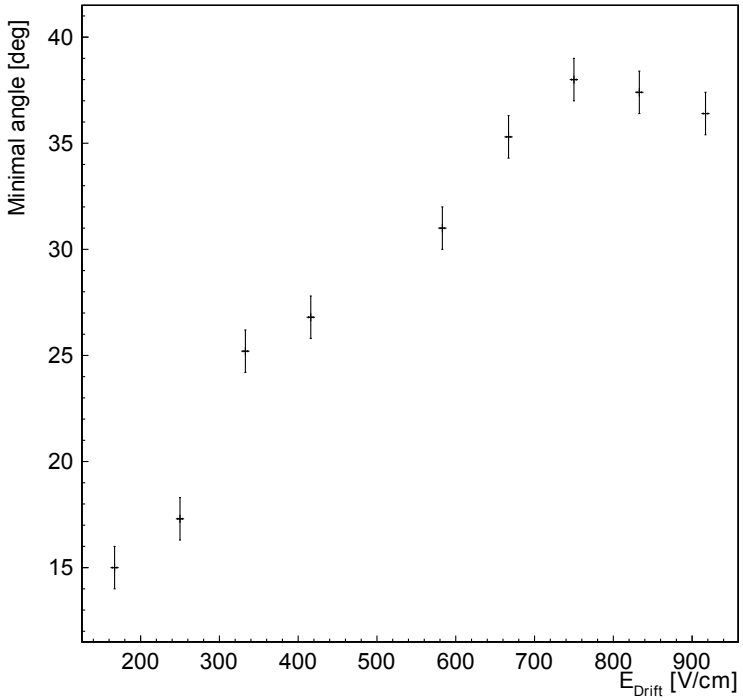


Figure 9.11: Lowest angle being 20% as likely as the most probable reconstructed angle against $E_{Drift}$ (as marked in figure 9.10). Measured with $^{252}$Cf-source and 1 $\mu$m $^{10}$B-cathode, all other fields were kept constant

### 9.2.5 Spatial resolution

The first step to achieve at least some spatial information was to apply collimated neutron geometries. Two sheets of 3 mm thick $B_4C$ were put in front of the detector to produce slits of 3, 2 and 1 mm width. For thermal neutrons of 10 meV these sheets are entirely untransparent. The resulting hit distributions in the detector are shown in figure 9.12(a) to 9.12(c). In all cases the slit is clearly visible as a broad peak on a homogenous plateau. The width of the peak is much wider than the width of the slits and although it becomes slightly narrower by variation, the slit width is not following the slit width as expected. This fact is most likely to be caused by the straggling of the neutrons, which are not collimated. There is an additional blurring since the position is still determined by the center of the charge of the tracks, which is not the interaction point of the neutron. The plateau is caused partly by the same reason, additional photon background and not perfect thermalized neutrons account for it. Since the count rate in this setup was in the range of 2-4 Hz it was not possible to collimate the neutrons better in order to measure the spatial resolution.

Using the reconstructed inclination angle of the charged particle tracks allowed to improve the reconstructed peak by calculating the interaction point of the neutron in the cathode. The inclination angle was calculated by two independent fits to the charge distribution in every charge cluster and only those events were used for which the difference in both calculations were less than 5°. A cut on the maximum angle was set to 75°, since higher values cannot be reconstructed in this gas mixture (see chapter 4). The charge in a cluster had to be higher than 1500 ADC counts in order to get rid of unwanted photon background. The starting point of a cluster $x_n$ was then calculated by the reconstructed angle, the center of charge position of the cluster $x_0$ and the cluster width represented by the number of strips in the cluster N and a factor f:

$$x_n = x_0 - \text{sign}(\theta) \cdot \epsilon \cdot N \tag{9.3}$$

The factor $\epsilon$ accounts for the spread of the charge cloud in the readout plane and therefore the difference between track length and number of strips. If there was no spread out and the charge position was also the geometric center of the track the factor would just be 0.5. If the charged particles would ionize perfectly homogenous along their track, the factor would only depend on the angle and the electric fields as was shown in chapter 4. Under this assumption the value should be about $0.45 \pm 0.02$ for most angles in this measurement.

In order to verify these simulations the hit distribution was recalculated by iteration of the factor $\epsilon$ from 0.25 to 0.75, as it can be seen in figure 9.13. Since the values for larger angles are predictably constant and the most probable value for a reconstructed angle is 30 degrees (see figure 9.10) a constant value for all angles is assumed. The FWHM of the peak due to the variation of this factor has minimum value at $\epsilon = 0.375 \pm 0.010$. The hit distribution, which is corrected by this factor is shown in figure 9.12(d). The FWHM width of the peak has been improved from $(4.25 \pm 0.05)$ mm to $(3.53 \pm 0.05)$ mm which is a improvement of 17%.

For a first test of the two dimensional strip readout also neutron absorbtion images with Boron nitride absorbers were done, as it can be seen in figure 9.14.The samples are equipped with holes of 0.5 and 1 mm respectively. Here the absorbers were placed directly atop of the detector. Neither 1 mm nor 0.5 mm holes in the absorbers are visible in the hit distributions in the detector. This again might be due to poor collimation of the source and the low statistics.

## 9.3 Determination of spatial resolution in neutron beams

In order to determine and optimize the spatial resolution of the detector and the reconstruction method it was possible to irradiate the detector directly in a neutron beam of the FRMII at the TREFF-beam line. The beam consisted of neutrons with a wavelength of 4.7 Å, which was collimated with four apertures. The distance of the cathode to the last aperture was 90 mm and the other apertures were placed as is shown in figure 9.15. The detector with two-dimensional readout was placed on a table, which could be moved by stepper motors in height and lateral to the beam in steps of 1/3200 mm. As converter the 1 µm $^{10}$B-cathode was used, with a drift space of 6 mm.

The detection efficiency of the GEM-detector was determined by a reference measurement with a $^{3}$He-tube, which for this neutron energy has a detection efficiency of close to 1. The GEM-detector has an efficiency of 3.8 % of the reference value from the tube. The efficiency of this cathode was simulated and measured at a value of 7 % by an Ar-$CO_2$ based gaseous detector (see [54]). The discrepancy between these two values is most likely due to a too high threshold for the trigger, because of electronic noise and gain limitations, because of the limited dynamic range of the APV25-chips. This deficit could most probably be fixed in future using an optimized trigger.

The resolution for this measurement was determined by a slit of $(150 \pm 20)$ µm. Its projection on the cathode had a maximum width of $(200 \pm 20)$ µm, because of the beam divergence. The height of the beam, 35 mm, was much larger,in order to obtain a reasonable detection rate. Figure 9.16 shows a uncorrected hit distribution, where the center of charge for every track is shown and its projection onto the Y-Axis. The width of the distribution has been determined using a Gaussian fit, the FWHM is 3.4 mm.

Corresponding to the correction for the one-dimensional readout the point of origin in every direction was then iteratively corrected in both planes and the best correction factor was determined by the width of the distribution. Here a distinctive feature of a narrow slit becomes apparent, since the correction leads to double peaks if the factor is chosen to small or to big. The corrected hit distributions are shown in figure 9.17.

This correction improves the spatial resolution massively. The best factor of 0.35 results in a FWHM of $(530 \pm 1)$ µm, even without any cuts to the angle. This method

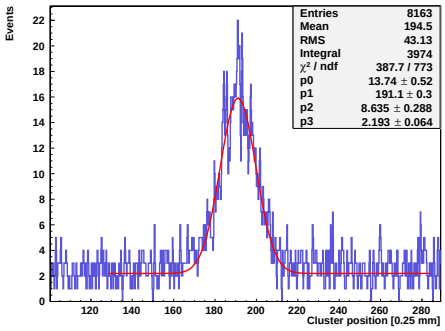


(a) Uncorrected hit distribution of neutrons with 3 mm slit collimator ($\sigma$=8.6·0.25 mm = 2.2 m)

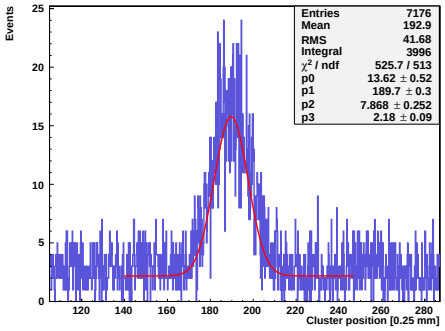


(b) Uncorrected hit distribution of neutrons with 2 mm slit collimator ($\sigma$=7.9·0.25 mm = 2.0 m)

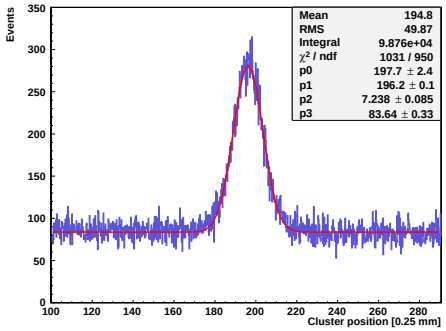


(c) Uncorrected hit distribution of neutrons with 1 mm slit collimator ($\sigma$=7.9·0.25 mm = 1.8 m)

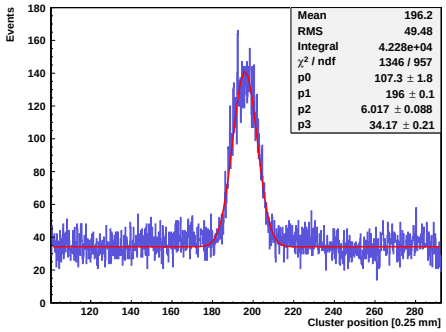


(d) Hit pattern for 1 mm slit corrected with direction of detected particle ($\sigma$=6.0·0.25 mm = 1.5 mm)

Figure 9.12: Slits produced by Boron-Carbide sheets of 3 mm thickness. $E_{Drift}$=165 V, $E_{Ind}$ = 3000 V cm$^{-1}$ , $E_{Trans1}$ = $E_{Trans2}$ = 2500 V cm$^{-1}$ , $\Delta U_{GEM1}$=300 V , $\Delta U_{GEM1}$=200 V and $\Delta U_{GEM1}$=215 V

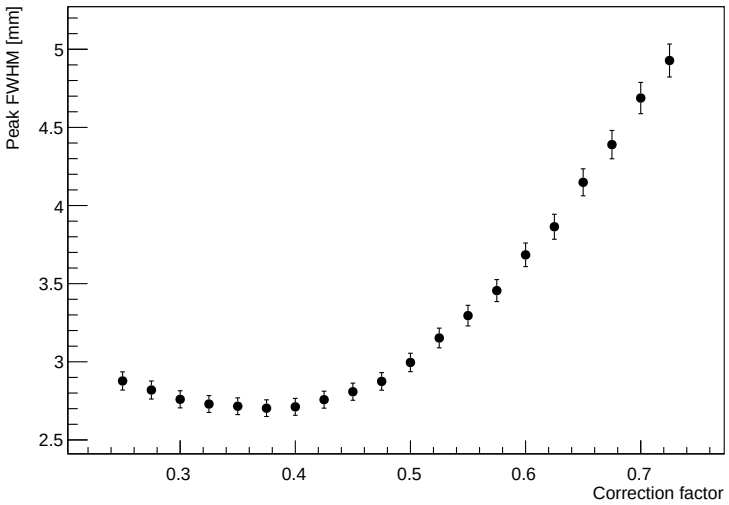


Figure 9.13: Corrected width of the distribution for a 1 mm slit in a $B_4C$ sheet in dependence of the correction factor

might be improved even more, if the correction factors are adapted to the inclination angles and particle types. This needs further evaluation, but the potential for improvement might be visible in figure 9.18, where the projection of a hit corrected hit distribution with a cut to the difference of the reconstructed angle in both directions is shown. A double Gaussian fit to the distribution leads to a width of the narrow Gaussian of $(366 \pm 1)$ µm. This cut is very course and only 20 % of the events survive this treatment, but this shows, that a trade-off for higher resolution for the price of efficiency is already possible.

To test whether the position reconstruction works homogeneously in the readout plane the detector was also moved relative to the readout plane with the movable table perpendicular to the beam. Therefore the table was moved from left to right[22]. The reconstructed position and the displacement from the original position are shown in figure 9.19. The reconstructed position is obviously perfectly correlated to the movement of the detector along a movement of 3 mm. There are also no features of the strip structure of the readout visible.

This first measurement shows, that high resolution position sensitive detection of thermal neutrons with a GEM-detector is possible. The detection efficiency for thermal neutrons with a single layer reaches an optimal value of approximately 10 % for a cathode coated with 2 µm of $^8B$. The neutron capture products can be discriminated and tracked for angles larger than 15° and the spatial resolution can be improved by a factor of 10 from about (3.45±0.01) mm to (366±1)µm.

22 The detector was tilted by 90° for this measurement, therefore a left-to-right movement with a vertical slit corresponds to an effective movement in the Y-direction of the detector system

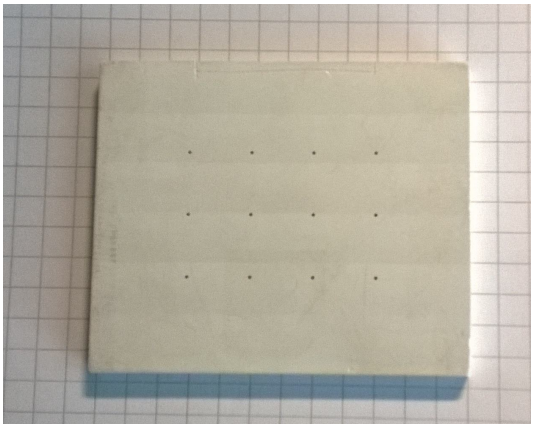

(a) Absorber A: 5 · 60· 50 mm Boron nitride sample sheet with 0.5 mm holes

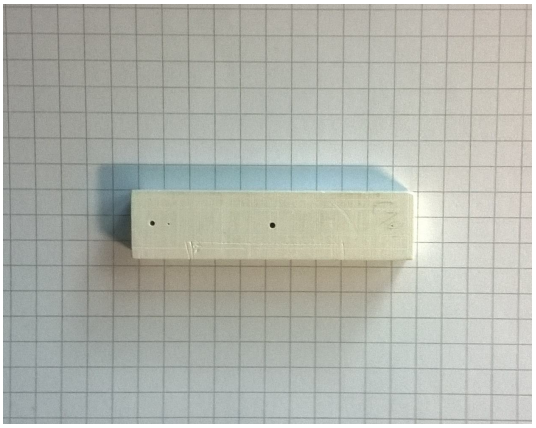

(b) Absorber B: 10 · 55· 12 mm Boron nitride sample sheet with 1 mm holes

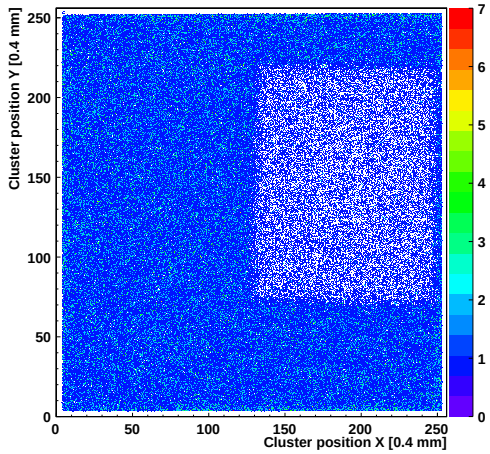


(c) Neutron absorbtion image with absorber A placed in front of the detector

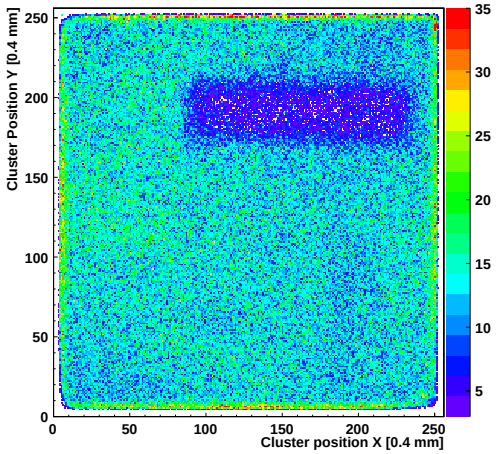


(d) Neutron absorbtion image with absorber B placed in front of the detector

Figure 9.14: Absorbtion images of boron nitride sheets placed directly above the cathode

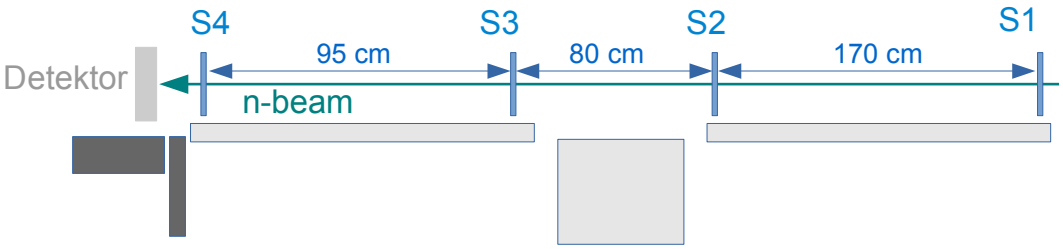


Figure 9.15: Experimental setup in the neutron beam. The width of the collimators for the slit measurements was 2 mm for S1 and S2 and the height was fixed to 20 mm for both. The aperture S3 was not used to collimate, but to get rid of beam halos. The aperture S4 defined the slit with a width of 150 $\mu$m and a height of 35 mm.

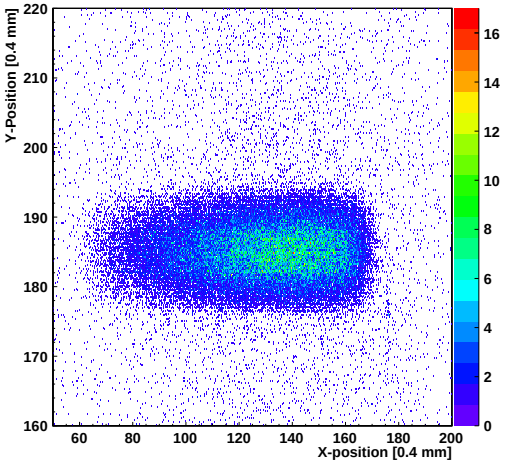


(a) Uncorrected two dimensional hit distribution for a slit. The inhomogenity in X-direction is a feature of the beam

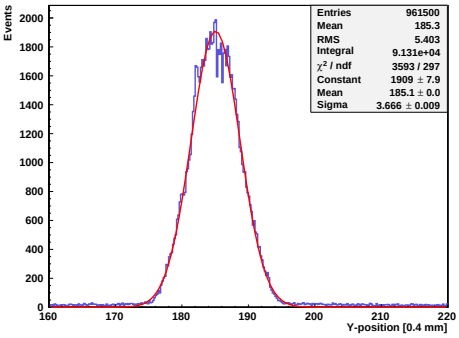


(b) Projection of the hit distribution in Y-direction with Gaussian fit. The distribution has a FWHM of 3.4 mm

Figure 9.16: Uncorrected hit distribution of a 150 µm slit, the center of charge positions are shown

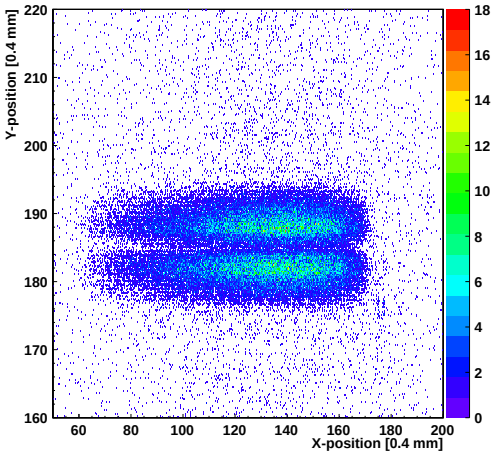


(a) By a factor of 0.1 corrected hit distribution, two peaks are visible in Y-direction because of the too small correction factor

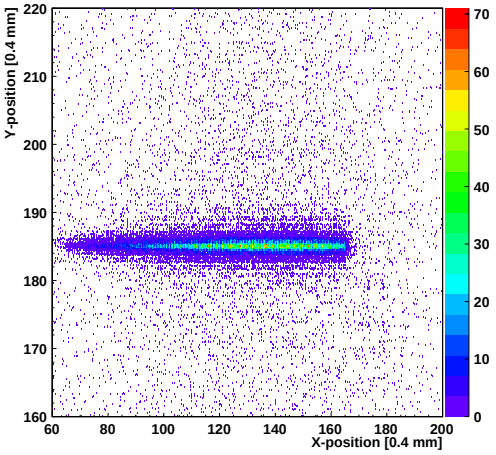


(b) By a factor of 0.35 corrected hit distribution

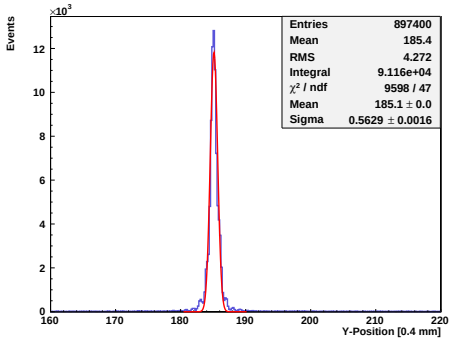


(c) Projection onto Y-axis of corrected hit distibution and Gaussian fit with FWHM of 530µm

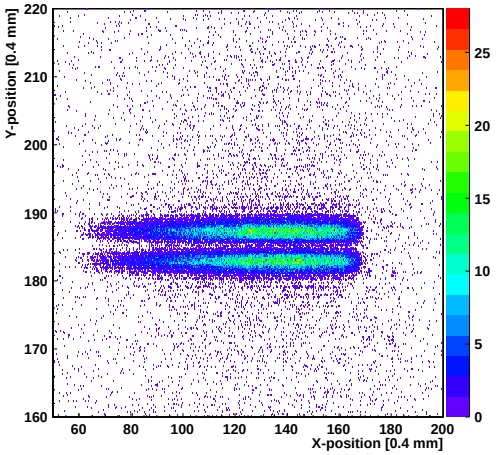


(d) By a factor of 0.8 corrected hit distribution. Two peaks are visible due to too large correction

Figure 9.17: Corrected hit distributions for different correction factors

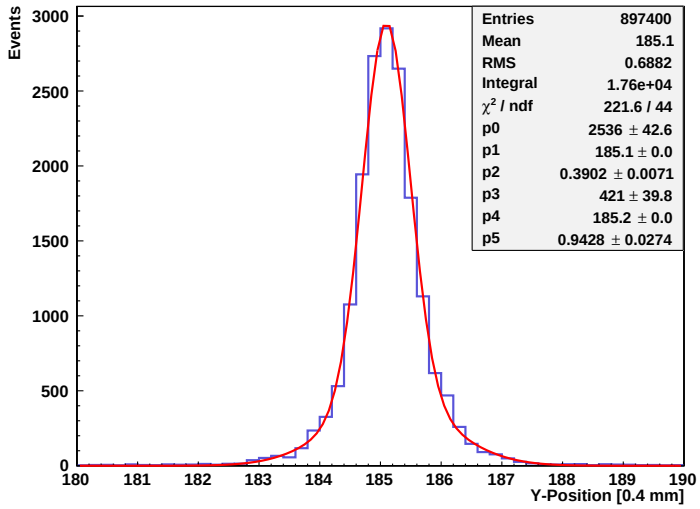


Figure 9.18: Projection of corrected hit distribution ($\epsilon$=0.35) with cuts to the difference of both reconstructed angles of a maximum of 5° for both planes. A fit of a double Gaussian leads to a FWHM of the smaller peak of 366 µm

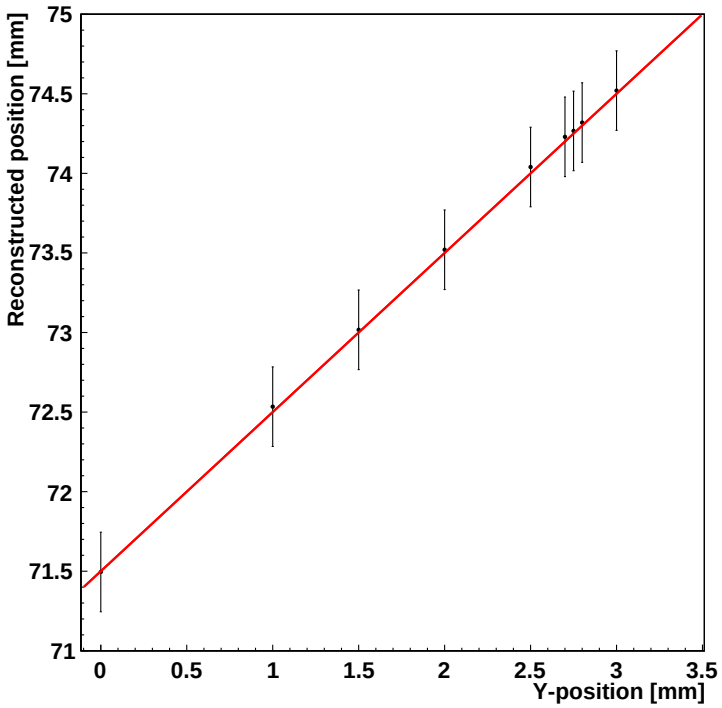


Figure 9.19: Position reconstruction for perpendicular movement of the detector relative to the slit. The line resembles the expected behaviour and is drawn to guide the eye

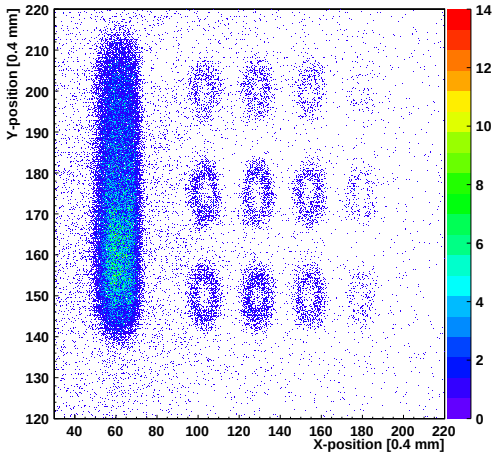


(a) Uncorrected image of absorber A irradiated with beam. The center of charge position is shown for every event. All twelve 0.5 mm holes are visible and the left edge of the sheet

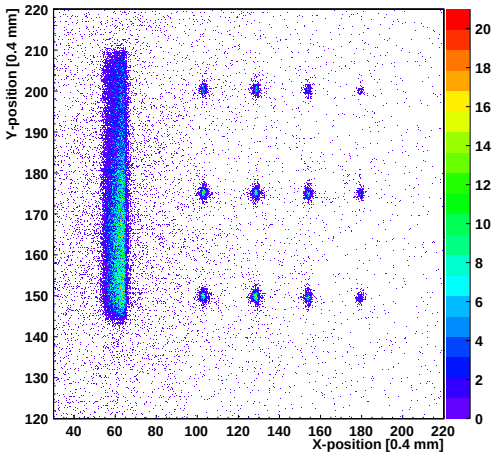


(b) Correction factor $\epsilon$=0.35; the holes and the left edge are much better defined

Figure 9.20: Neutron absorbtion image of the Boron nitride sheet shown in figure 9.14 irradiated with a thermal neutron beam of approximatly 60·35 $m^2$ size

# 10 Conclusion

The main goal of this thesis was to show, whether a GEM-based detector can be used for tracking of photons and neutrons. Three small prototype detectors with an active area of 10·10 $cm^2$ have been build, two of them with one dimensional strip readout and one with two dimensional strip readout. The one dimensional readout consists of 384 parallel copper strips with 250 $\mu$m pitch. The 2D-readout is the standard CERN GEM-readout with 250 strips for each direction and a pitch of 400 $\mu$m. The readout for all of them is based on time resolving and sampling APV25-chips. The detectors have been modeled and simulated in Geant4 and Garfield. The efficiency for detection of photons has been measured and simulated for different photon energies in the range between 3 and 51 keV for converter foils coated with aluminum, copper and gold and also a stainless stell mesh. For photon energies of 35 keV, as they are most dominant in a $^{133}$Ba source, simulation and measurement show very good agreement. It has been shown that a single layer of 466 nm gold can improve the overall detection efficiency for 35 keV photons by (120±20)% in comparison to a standard aluminized Kapton-cathode. For neutrons boron-carbide and $^{10}$B cathodes have been used to detect thermal neutrons and track the spallation products of the neutron capture reaction on boron. The detection efficiency for thermal neutrons reaches its optimal value of 8 % at a 3 $\mu$m layer of $^{10}$B.

Simulations and measurement both show, that the resolution for single electrons in the detector in the used geometric setup is limited to (460±10) $\mu$m for a single GEM-foil and (720±10) $\mu$m for a triple GEM-detector, therefore it might be useful to minimize the number of GEM-foils used, if detection of very short tracks is intended. The tracking capabilities were evaluated for tracks of muons and by means of Garfield simulations. An angular resolution of (3±1)° could be achieved for tracks of muons from 10 ° to 30° inclination angle. Simulations predict, that for a track length of 6 mm in the gas the reconstruction works in the range from 10° to 70°. The influence of the electric fields on the angular reconstruction has been measured and led to an optimal drift field of 200 V $cm^{-1}$. This value allows reasonable reconstruction of angles down to (15±1)° measured with products of the boron-neutron capture process, which have a track length in the gas of $(5 \pm 1)$ mm.

Comparison of simulations and measurements with the one-dimensional detectors predict that photon tracking is possible for photoelectrons of an energy above 20 keV.

The position resolution for a single object with 5.9 keV photons was determined to be better than 150 $\mu$m. For neutron reconstruction of the position of the interaction in the conversion layer could be applied in order to increase the position resolution. In a neutron beam the spatial resolution could be increased from $(3.45 \pm 0.01)$ mm

without this method to $(366 \pm 1)$ µm by applying a correction based on the inclination of the tracked secondary ions.

Overall it has been successfully shown a GEM-detector is suited for the detection of photons and thermal neutrons. The charged products in the detector particularly for neutron detection could be tracked with high accuracy, which led to a significant improvement of the resolution of the point of interaction in the converter cathode. There has to be further investigation of the behaviour of the energy deposit of electrons and ions in the gas and the detector response, which could lead to an even higher resolution especially for 35 keV photons and the potential reconstruction of point sources.

# A Radon-Transformation

The Radon transformation is an integral transformation first described by Johann Radon [55], which is related to a Fourier transformation in two dimensions and a special case of the Hough-transformation. Its inverse is widely used in medical applications. The transformation is defined as an integral of the function f along a line $\gamma$, which is parametrized as:

$$(x(t), y(t)) = (r\cos\alpha + t\sin\alpha, r\sin\alpha - t\cos\alpha) \tag{A.1}$$

Which leads to a transformation:

$$Rf(r,\alpha) = \int_{-\infty}^{\infty} f\left(r\cos\alpha + t\sin\alpha, r\sin\alpha - t\cos\alpha\right) \mathrm{d}t \tag{A.2}$$

By this process every point of the function is, depending on its position, converted into a line in the Radon space. The intersection of those lines can be translated into a straight line in the original function. The transform is shown graphically for a sample muon track with a Radon-transformation implemented in "mathematica". The initial distribution is transformed, hot spots in the transformation are detected and those hot spots are transformed back into lines. For the decision wether one or more tracks are defined by multiple charge clusters in a single event this method was applied. The algorithm used here is described in [56]. Here not the complete raw data was used but only the points representing the extrapolated start of a signal on each strip for all strips that have been already sorted into a cluster. The hot spots are then calculated with the root peak finder tool. If only one hot spot is found the clusters are merged, if more than one hot spot is found the event is neglected.

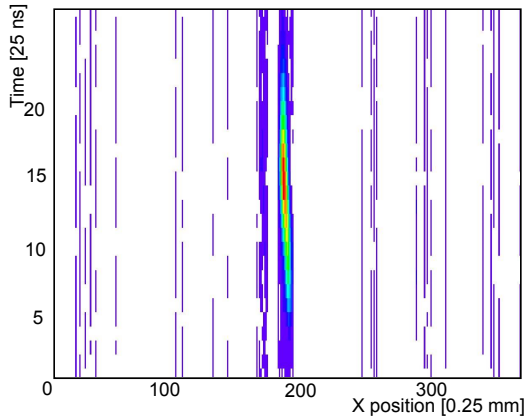


(a) Unaltered track for a muon in time-space coordinate system

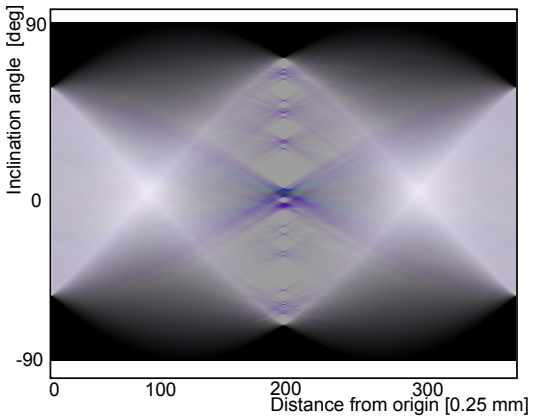


(b) Radon transformed track

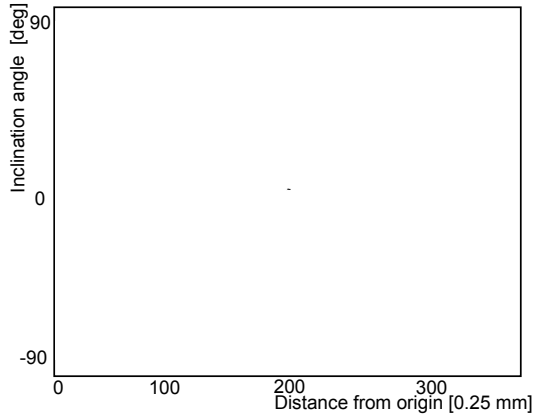


(c) Hot spot in Radon trandform coresponding to a track in the real space

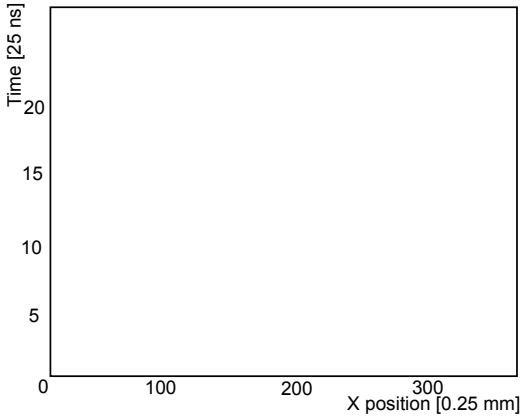


(d) Inverse transformation of the maximum of the radon transformed pattern

Figure A.1: Radon transform of a raw track

# B Housing and construction of the 2D-GEM

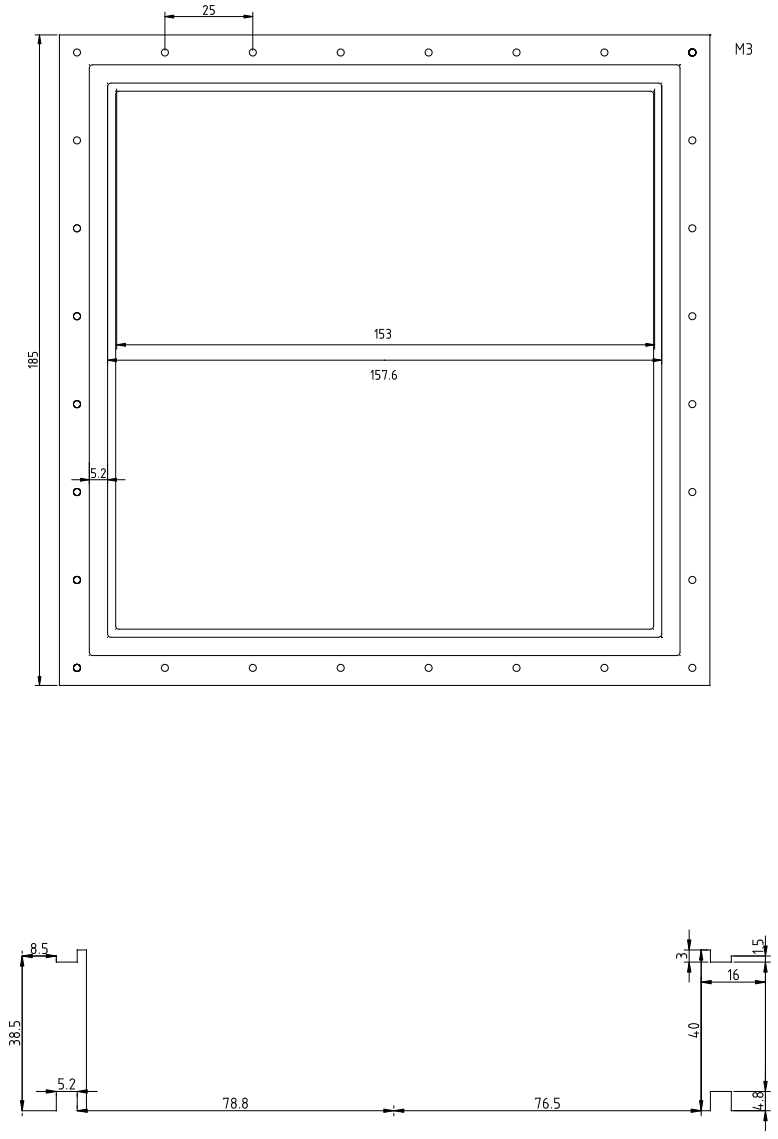


Figure B.1: Plan of the aluminum housing for the two-dimensional readout

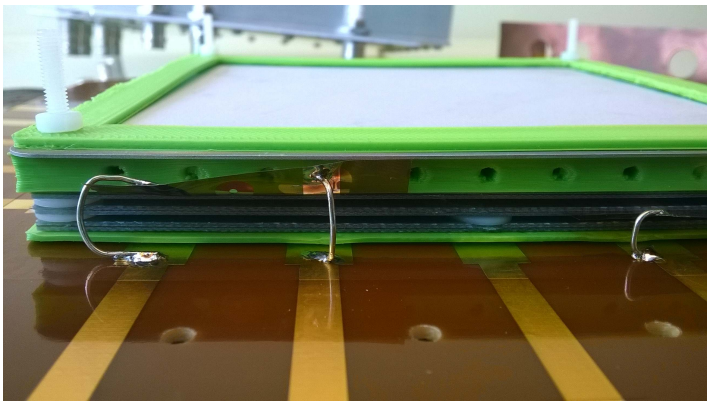

Figure B.2: Readout-board with stack of tree GEM-foils, PLA-spacers (green) and boron-coated aluminum cathode. The GEM-foils are separated by eight 0.8 mm teflon spacers each. For the lowest GEM-foil and the cathode spacers printed from PLA-plastic of 1.4 mm and 6 mm thickness respectively were used

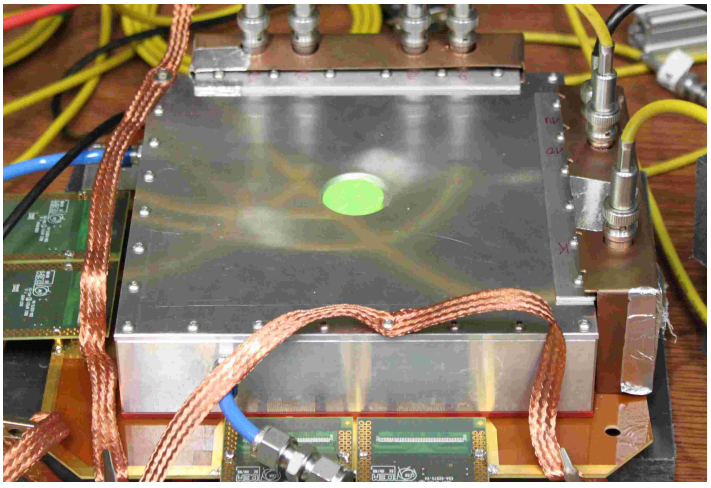

Figure B.3: Fully assembled detector with 3 mm aluminum lid and window for photon irradiation. The cables, which link the SHV- and BNC-connectors of the HV-supply with the electrodes on the readout board, have to be shielded carefully, which is realized by copper Farraday cages

# C Root Macros and Simulations

The data analysis has in total be carried out with root macros, which all can be found at: /data/etp6/Flierl/programs/macros/

The programs

`L1_Cosmic, analysis_CRF and ana_CRF`

are based on macros of the same name, written by P. Lösel (see [43]).

The Garfield based simulations can be found at: /data/etp6/Flierl/programs/garfieldsim/ with subdivisions for calculation of drift velocity and simulation of one, two or three GEM-foils in the detector.

The Genat4 based simulations can be found at: /data/etp6/Flierl/programs/geantsim/

The usage and function is described in a separate readme-file in every folder.

# Bibliography


[1] Atlas collaboration. `http://twiki.cern.ch/twiki/bin/view/AtlasPublic/`, 2013.

[2] F.N. Flakus. Detecting and measuring ionizing radiation- a short history. *IAEA Bulletin*, 23(4):31–36.

[3] J. Beringer et al. *Particle Physics Booklet*. Institute of Physics publishing, 2010.

[4] E. Fermi. The ionization loss of energy in gases and in condensed materials. *Phys. Rev.*, 57:485–493, Mar 1940.

[5] W.R. Leo. *Techniques for Nuclear and Particle Physics Experiments: A How-To Approach*. U.S. Government Printing Office, 1994.

[6] J.H. Hubbell M.J. Berger. "XCOM: Photon Cross Sections Database". `http://www.nist.gov/pml/data/xcom/index.cfm`. Accessed: 16.9.2014.

[7] K. Kleinknecht. *Detectors for Particle Radiation*. Cambridge University Press, 1998.

[8] M. E. Rose and S. A. Korff. An investigation of the properties of proportional counters. i. *Phys. Rev.*, 59:850–859, Jun 1941.

[9] Ö. Şahin, İ. Tapan, E.N. Özmutlu, and R. Veenhof. Penning transfer in argon-based gas mixtures. *Journal of Instrumentation*, 5(05):P05002, 2010.

[10] F. Sauli. GEM: A new concept for electron amplification in gas detectors. *Nuclear Instruments and Methods in Physics Research Section A: Accelerators, Spectrometers, Detectors and Associated Equipment*, 386(2):531–534, 1997.

[11] S. Bachmann et al. Charge amplification and transfer processes in the gas electron multiplier. *Nuclear Instruments and Methods in Physics Research Section A: Accelerators, Spectrometers, Detectors and Associated Equipment*, 438(2–3):376 – 408, 1999.

[12] D. Heereman. Development of Micro-Pattern Gaseous Detectors - GEM. Diplomarbeit, Ludwigs-Maximilians-Universität, München, Dezember 2010.

[13] S. Bachmann et al. Discharge studies and prevention in the gas electron multiplier (gem). *Nuclear Instruments and Methods in Physics Research Section A: Accelerators, Spectrometers, Detectors and Associated Equipment*, 479(2–3):294 – 308, 2002.

[14] F. Sauli. Progress with the gas electron multiplier. *Nuclear Instruments and Methods in Physics Research Section A: Accelerators, Spectrometers, Detectors and Associated Equipment*, 522(1–2):93 – 98, 2004. {TRDs} for the Third Millenium. Proceedings of the 2nd Workshop on Advanced Transition Radiation Detectors for Accelerator and Space Applications.

[15] R. de Oliviera and CERN-Detector Developement Group. `http://gdd.web.cern.ch/GDD/`.

[16] B. Flierl. Effizienzbestimmung und Optimierung an einem GEM-Detektor. Praktikumsbericht, Ludwig-Maximilians-Universität München, 2013.

[17] L.L. Jones, M.J. French, Q. Morrissey, A. Neviani, M. Raymond, et al. The APV25 deep submicron readout chip for CMS detectors. *Conf.Proc.*, C9909201:162–166, 1999.

[18] J. Bortfeldt. *Development of floating strip micromegas detectors*. PhD Thesis, April 2014.

[19] B. Ketzer et al. A triple-gem detector with pixel readout for high-rate beam tracking in compass. In *Nuclear Science Symposium Conference Record, 2007. NSS '07. IEEE*, volume 1, pages 242–244, Oct 2007.

[20] J. Alme et al. The ALICE TPC, a large 3-dimensional tracking device with fast readout for ultra-high multiplicity events. *Nuclear Instruments and Methods in Physics Research Section A: Accelerators, Spectrometers, Detectors and Associated Equipment*, 622(1):316 – 367, 2010.

[21] B. Ketzer. A time projection chamber for high-rate experiments: Towards an upgrade of the ALICE TPC. *Nuclear Instruments and Methods in Physics Research Section A: Accelerators, Spectrometers, Detectors and Associated Equipment*, 732(0):237 – 240, 2013. Vienna Conference on Instrumentation 2013.

[22] Y. Lan-Lan, T. Yan, M. Shan-Le, and Z. Pan-Pan. Study of spatial resolution in a single GEM simulated by Monte-Carlo method. 2013, 1306.0270.

[23] R.B. Firestone and V.S. Shirley. *Table of Isotopes, 2 Volume Set*. Table of Isotopes. Wiley, 1998.

[24] E.M.A. Hussein. *Handbook on Radiation Probing, Gauging, Imaging and Analysis: Basics and techniques*. Non-Destructive Evaluation Series. Kluwer Academic, 2003.

[25] M. Byszewski. MMDAQ Q&A, RD51 Collaboration Mini Week. `http://indico.cern.ch/event/218341/session/1/contribution/22/material/slides/0.pdf`, December 2012.

[26] K.J. Binns and P.J. Lawrenson. *Analysis and Computation of Electric and Magnetic Field Problems*. Pergamon international library of science, technology, engineering, and social studies. Elsevier Science & Technology, 1973.

[27] R. de Oliveira. DEM - Developement of Electronic Modules. `http://ts-dep-dem.web.cern.ch/ts-dep-dem/`.

[28] H. Schindler. Garfield++ - User Guide. http://garfieldpp.web.cern.ch/garfieldpp, September 2014.

[29] S. Biagi. Magboltz - transport of electrons in gas mixtures. http://consult.cern.ch/writeup/magboltz/, Mai 2012.

[30] I.B. Smirnov. Modeling of ionization produced by fast charged particles in gases. *Nuclear Instruments and Methods in Physics Research Section A: Accelerators, Spectrometers, Detectors and Associated Equipment*, 554(1–3):474 – 493, 2005.

[31] J. Renner. Detector simulation in garfield++ with open-source finite element electrostatics. http://garfieldpp.web.cern.ch/garfieldpp/examples/elmer/garfield_elmer_doc.pdf.

[32] S. Moll. Entladungsstudien an Micromegas -Teilchendetektoren. Diplomarbeit, Ludwigs-Maximilians-Universität, München, Juni 2013.

[33] A. Sharma. A how-to approach for a 3D simulation of charge transfer characteristics in a gas electron multiplier (GEM). *ICFA Instrum.Bull.*, 19:2, 1999.

[34] T. Lari. Measurements of spatial resolution of ATLAS pixel detectors. *Nuclear Instruments and Methods in Physics Research Section A: Accelerators, Spectrometers, Detectors and Associated Equipment*, 465(1):112 – 114, 2001. {SPD2000}.

[35] J. Allison et al. Geant4 developments and applications. *Nuclear Science, IEEE Transactions on*, 53(1):270–278, Feb 2006.

[36] S. Agostinelli et al. Geant4—a simulation toolkit. *Nuclear Instruments and Methods in Physics Research Section A: Accelerators, Spectrometers, Detectors and Associated Equipment*, 506(3):250 – 303, 2003.

[37] Geant4 Collaboration. Geant4 User's Guide for Application Developers-Version: geant4 10.0. http://geant4.web.cern.ch/geant4/. Accessed: 1.3.2014.

[38] Geant4 Collaboration. Physics Reference Manual-geant4 9.5.0. http://geant4.web.cern.ch/geant4/, note = Accessed: 2.3.2014.

[39] K. Nakamura et al. Review of particle physics. 37(7A):1–1422, 2010.

[40] C. Davisson and R. Evans. Gamma-ray absorption coefficients. *Rev. Mod. Phys.*, 24:79–107, Apr 1952.

[41] Y. F. Yang, Y. Gono, S. Motomura, S. Enomoto, and Y. Yano. A compton camera for multitracer imaging. *Nuclear Science, IEEE Transactions on*, 48(3):656–661, Jun 2001.

[42] O. Biebel, M. Binder, M. Boutemeur, A. Brandt, J. Dubbert, G. Duckeck, J. Elmsheuser, F. Fiedler, R. Hertenberger, O. Kortner, et al. A cosmic ray measurement facility for atlas muon chambers. *arXiv preprint physics/0307147*, 2003.

[43] Phillip Lösel. Performance studies of large size micromegas detectors. Master's thesis, Ludwig-Maximilians-Universität München, October 2013.

[44] O. Klein and Y. Nishina. Über die Streuung von Strahlung durch freie Elektronen nach der neuen relativistischen Quantendynamik von Dirac. *Zeitschrift für Physik*, 52(11-12):853–868, 1929.

[45] M.J. Berger et al. ESTAR,PSTAR and ASTAR:Computer Programs for Calculating Stopping-Power and Range Tables for Electron,Protons and Helium Ions (version 1.2.3). `http://physics.nist.gov/Star`, June 2014.

[46] M. Klein and C. Schmidt. Cascade, neutron detectors for highest count rates in combination with asic/fpga based readout electronics. *Nuclear Instruments and Methods in Physics Research Section A: Accelerators, Spectrometers, Detectors and Associated Equipment*, 628(1):9 – 18, 2011. {VCI} 2010 Proceedings of the 12th International Vienna Conference on Instrumentation.

[47] K. Kaneko and T. Kohmura. Soft X-ray response of Au-GEM. *Journal of Instrumentation*, 7(07):C07001, 2012.

[48] K.H. Beckurts and K. Wirtz. *Neutron physics*. Springer, 1964.

[49] National Nuclear Data Center. Chart of nuclides. `http://www.nndc.bnl.gov/chart/changeUnc.jsp?unc=standard`.

[50] D. Shea and D. Morgan. The helium-3 shortage: Supply, demand, and options for congress. `http://fas.org/sgp/crs/misc/R41419.pdf`.

[51] K. Zeitelhack. Advanced Summer School in Radiation Detection and Measurement-Neutron Detection and Imaging. 4. Advanced Summer School in Radiation Detection and Measurements, TU München.

[52] I. Stefanescu and K. Zeitelhack. Simulation der Abschirmung einer 252Cf Quelle. Präsentation, TU München.

[53] J. F. Ziegler, J. P. Biersack, and Matthias D. Ziegler. *SRIM, the stopping and range of ions in matter*. SRIM Co., 2008.

[54] I. Stefanescu, Y. Abdullahi, J. Birch, I. Defendi, R. Hall-Wilton, C. Höglund, L. Hultman, M. Zee, and K. Zeitelhack. A 10 B-based neutron detector with stacked MultiWire Proportional Counters and macrostructured cathodes. *Journal of Instrumentation*, 8(12):P12003, 2013.

[55] J. Radon. Berichte über die Verhandlungen der Königlich Sächsischen Gesellschaft der Wissenschaften zu Leipzig: Mathematisch-Physische Classe. 69:262–277, 1917.

[56] C. Hoilund. *The Radon Transform*. Aalborg University, November 2007.

# Acknoledgements

Ich möchte mich bei allen bedanken, ohne deren Beteiligung diese Arbeit nicht entstanden wäre:

- Prof. Dr. Otmar Biebel dafür, dass er mir die Möglichkeit gegeben hat diese Arbeit zu schreiben und auch dafür, dass er auf wirklich jede Frage eine Antwort weiß
- Dr. Ralf Hertenberger für die extrem engagierte Betreuung dieser Arbeit, seine vielen Anmerkungen und Korrekturen und nicht zuletzt für seine unablässige Unterstützung in allen Belangen
- Prof. Dr. Dorothee Schaile für die freundliche Aufnahme in ihrem Lehrstuhl und das hervorragende Arbeitsklima
- Dr. Karl Zeitelhack für die Möglichkeit Messungen mit Neutronen am Forscchungsreaktor durchführen zu können, vorallem aber für die viele Hilfe und Erfahrung mit der er diesen Teil der Arbeit unterstützt hat
- Fr. Friscchke für die vielen Versuche Aluminium mit $B_4C$ zu bedampfen und die Goldkathode herzustellen
- Phillip Lösel für die Stunden, die er mich beim schreiben der Analysesoftware unterstützt hat
- Dr. Jonathan Bortfeldt, Dr. André Zibell und Alexander Ruschke für die Hilfe bei allen großen und kleinen Fragen
- Johannes Grossmann und Elias Pree stellvertretend für alle meine Kommilitonen, die mich in den letzten Jahren begleitet haben und mir das Studium nie zu lange werden ließen
- Und schließlich meiner Familie für die Unterstüzung der letzten Jahre, weil es mir nie an irgendetwas fehlte

# Selbstständigkeitserklärung

Hiermit versichere ich, die vorliegende Arbeit selbstständig und unter ausschließlicher Verwendung der angegebenen Literatur und Hilfsmittel erstellt zu haben.

| | |
|---|---|
| Ort, Datum | Bernhard Flierl |